On finite-temperature holographic QCD in the Veneziano limit

T. Alho,[a] **M. Järvinen,**[b] **K. Kajantie,**[c] **E. Kiritsis**[b,d,1] **and K. Tuominen**[a,c]

[a] *Department of Physics,*
P.O. Box 35, FI-40014 University of Jyväskylä, Finland[2]

[b] *Crete Center for Theoretical Physics, Department of Physics,*
University of Crete, P.O. Box 2208, 71003 Heraklion, Greece[3]

[c] *Helsinki Institute of Physics,*
P.O. Box 64, FI-00014 University of Helsinki, Finland[4]

[d] *APC, Université Paris 7, CNRS/IN2P3 (UMR du CNRS 7164), CEA/IRFU,*
Obs. de Paris, Sorbonne Paris, Cité, Bâtiment Condorcet, F-75205, Paris Cedex 13, France[5]

E-mail: timo.s.alho@jyu.fi, mjarvine@physics.uoc.gr,
keijo.kajantie@helsinki.fi, kimmo.i.tuominen@jyu.fi

ABSTRACT: Holographic models in the $T = 0$ universality class of QCD in the limit of large number N_c of colors and N_f massless fermion flavors, but constant ratio $x_f = N_f/N_c$, are analyzed at finite temperature. The models contain a 5-dimensional metric and two scalars, a dilaton sourcing $\mathrm{Tr}F^2$ and a tachyon dual to $\bar{q}q$. The phase structure on the T, x_f plane is computed and various 1st order, 2nd order transitions and crossovers with their chiral symmetry properties are identified. For each x_f, the temperature dependence of p/T^4 and the condensate $\langle \bar{q}q \rangle$ is computed. In the simplest case, we find that for x_f up to the critical $x_c \sim 4$ there is a 1st order transition on which chiral symmetry is broken and the energy density jumps. In the conformal window $x_c < x_f < 11/2$, there is only a continuous crossover between two conformal phases. When approaching x_c from below, $x_f \to x_c$, temperature scales approach zero as specified by Miransky scaling.

---

[1]Contact information can be found here: http://hep.physics.uoc.gr/~kiritsis/

[2]https://www.jyu.fi/fysiikka/en

[3]http://hep.physics.uoc.gr

[4]http://www.hip.fi

[5]http://www.apc.univ-paris7.fr

Contents

1 Introduction

QCD in the Veneziano limit [1],

$$N_c \to \infty, \quad N_f \to \infty, \quad \frac{N_f}{N_c} = x_f \ \text{ fixed}, \quad \lambda = g_{\rm YM}^2 N_c \ \text{ fixed}, \tag{1.1}$$

is expected to display a host of interesting and mostly non-perturbative phenomena, including:

- The "conformal window" with a nontrivial infrared (IR) fixed point, which extends from $x_f = \frac{11}{2}$ to smaller values of x_f. The region $x_f \to \frac{11}{2}$ has an IR fixed point while the theory is still weakly coupled, as was analyzed in [2] (see also [3, 4]).

- It is expected that at a critical $x_f = x_c$, the conformal window will end, and for $x_f < x_c$, the theory will exhibit chiral symmetry breaking in the IR. This behavior is expected to persist down to $x_f = 0$. For $x_f > x_c$ the IR theory is a conformal field theory at strong coupling, that progressively becomes weak as $x_f \to \frac{11}{2}$.

- Near and below x_c, there is the transition region to conventional QCD IR behavior. In this region the theory is expected to be "walking": This means that the theory appears to be approaching the IR fixed point as the coupling evolves very slowly for many e-foldings of energies. But chiral symmetry breaking is nevertheless triggered and in the deep infrared the coupling diverges as in QCD. The slow evolution of the coupling has been correlated with a nontrivial dimension for the quark mass operator near two, rather than three (the free field value). IR observables are expected to obey the Miransky scaling [5–7] as $x_f \to x_c$ from below.

- New phenomena are expected to appear at finite density driven by strong coupling and the presence of quarks. These include color superconductivity [8, 9]. In this case, however, gauge invariant vevs are effectively double trace operators and the phase structure is determined at the next to leading order in $1/N_c$.

– 1 –

The existence of the "walking" region makes the theory extremely interesting for applications in dynamical electroweak symmetry breaking (technicolor). This has also motivated an intensive lattice Monte Carlo work during recent years [10–14]. The bulk of this work has been done at zero temperature; recently there appeared the first attempts to go to finite T for QCD with $N_c = 3$, N_f up to 8 [14–16] and for non-QCD-like theories [17]. Chiral effective theories have also been applied [18–25].

The aim of the present work is to study a class of holographic bottom-up models (V-QCD) that belong to the universality class of QCD with massless quarks in the Veneziano limit [26] at finite temperature and zero chemical potential. We will calculate the temperature dependence of the free energy density ($= -$pressure $= -p(T)$) and of the quark condensate ($\langle\bar{q}q\rangle(T)$). The former acts as an effective order parameter for deconfinement (at large N_c), for which there is no true order parameter associated with a symmetry.[1] The quark condensate is a true order parameter for chiral symmetry if quarks are massless. The calculation is carried out for the full range of x_f, $0 < x_f < 11/2$.

Discontinuities or rapid variations in pressure (or energy density) and quark condensate can be used to define phase boundaries associated with deconfinement and chiral symmetry restoration temperatures $T_d(x_f)$ and $T_\chi(x_f)$. We will use the usual nomenclature: If the nth derivative of $p(T)$ is discontinuous, the transition is of nth order. We also consider continuous *crossovers* which are identified by using the scaled quantity $(\epsilon - 3p)/T^4$. Its maximum defines the crossover temperature $T_{\text{crossover}}(x_f)$. The phase diagram is defined as a plot of all phase boundaries on the (x_f, T) plane. The phase diagrams we present will also contain a rich structure of metastable states, namely local (but globally subleading) minima of the free energy.

In the holographic approach the thermal transitions will be transitions between various 5-dimensional black hole and "thermal gas" metrics and the nomenclature of transitions, explained later in great detail, will be correspondingly different. The holographic approach is constrained but not fully constrained and we cannot give a precise prediction of the phase diagram of hot V-QCD. We can state the most plausible behavior but we can also mention a few other alternatives. We will always find the analogues of T_d and T_χ, but we will also find transitions with no obvious QCD interpretation. Whether these reflect real physics of hot QCD in the Veneziano limit or whether they are artifacts of the holographic approach will be an interesting problem for further study.

The usual expectation is that there is a 1st order line at $T_d = T_\chi$; in the large N_c limit one can actually prove that $T_\chi \geq T_d$ [18, 19]. The main class of our predictions reflect these properties: for smaller x_f we find that deconfinement and chiral symmetry restoration coincide, but for x_f approaching x_c the deconfining and chiral transitions can become separate so that $T_\chi > T_d$ (see, for example, figure 13 below). The chiral transition is then of 2nd order (and mean field type). Furthermore, for smaller x_f the separate 2nd order chiral transition is in the metastable region so that it can be reached if the system is supercooled [27]. One might here add that $T_\chi < T_d$ for stable phases may be reached at large chemical potential [28, 29].

---

[1] A related one, used commonly in lattice work, is the expectation value of the Polyakov loop.

The starting point of our finite temperature analysis is the $T = 0$ holographic model introduced in [26], based on previous theoretical ideas in [30–40]. Moving to finite T implies studying black hole solutions of the action in [26]. A defining characteristic of this class of models is that they contain full backreaction between the duals of the color and flavor degrees of freedom. Earlier work [41–48] on thermodynamics in such bottom-up models imposed quasiconformality directly on the beta function of the theory. One should note that walking behavior and the related "conformal transition" at $x_f = x_c$ have also been studied in top-down models [49–54], as well as in simpler bottom-up models [55–60] which do not attempt to model the backreaction. See also [40, 61] on introducing backreacted flavor in the top-down models.

In this introduction we will first describe the special properties of V-QCD from [26] and then discuss general properties of its black hole solutions. Section 2 will contain a detailed discussion of the action of the model and of the two characteristic classes of scalar potentials. Section 3 presents the Einstein equations of the model, describes how they are numerically solved and, finally, how thermodynamics is computed from the numerical bulk fields. A particularly delicate issue here is the fixing of the quark mass m to zero. We also briefly comment on fixing m to some nonzero value. An extensive list of numerical results is given in section 4. From these, the types of phase transition lines the models predict are determined. In section 5, techniques for computing the condensate are described and several numerical results are given. One should note that this, as well as many other numerical issues in the model, are technically very demanding. Finally, section 6 contains a discussion of what are the effects of making the quark mass nonzero. Several detailed considerations are collected in appendices.

1.1 V-QCD at zero temperature

In [26] a class of bottom-up holographic models was introduced (named V-QCD) and shown to be in the universality class of QCD in the Veneziano limit at zero temperature and density. These were 5-dimensional models of two scalars coupled to gravity. One of the scalars, the "dilaton" λ, is dual to $\mathrm{Tr}[F^2]$ (the QCD gauge coupling constant, or more precisely the 't Hooft coupling). The other scalar, the "tachyon" τ, is dual to the quark mass operator $\bar{q}q$. The potentials and interactions were modeled along successful bottom-up models for YM, namely Improved Holographic QCD (IHQCD) [30–36] and the idea that string theory tachyon condensation describes chiral symmetry breaking [37–39, 62–65].

The bulk action considered was

$$S = S_g + S_f, \quad S_g = M^3 N_c^2 \int d^5x \sqrt{-g} \left[R - \frac{4}{3} \frac{(\partial\lambda)^2}{\lambda^2} + V_g(\lambda) \right], \tag{1.2}$$

with λ the 't Hooft coupling (exponential of the dilaton ϕ) and the tachyon[2] action[3]

$$S_f = -x_f M^3 N_c^2 \int d^5x \, V_f(\lambda, \tau) \sqrt{\det(g_{\mu\nu} + \kappa(\lambda)\partial_\mu\tau\partial_\nu\tau)}. \tag{1.3}$$

---

[2]We have taken the tachyon to be real and diagonal in flavor space.

[3]To find the vacuum (saddle point) solution we have set the gauge fields $A_\mu^{L,R}$ dual to the QCD currents to zero, as they are not expected to have vacuum expectation values at zero density. We have also suppressed the Wess-Zumino terms as they also do not contribute to the vacuum solution.

The pure glue potential V_g has been determined from previous studies [33–35]. The tachyon potential $V_f(\lambda, \tau)$ must satisfy some basic properties determined by the dual theory or by general properties of tachyons in string theory: (a) To provide the proper dimension for the dual operator near the boundary (b) To exponentially vanish for $\tau \to \infty$. The function $\kappa(\lambda)$ captures, among other things, the transformation from the string frame to the Einstein frame in five dimensions. The class of potentials that were investigated in [26] are of the form

$$V_f(\lambda, \tau) = V_{0f}(\lambda)e^{-a(\lambda)\tau^2}. \tag{1.4}$$

In the Veneziano limit, the back-reaction of the flavor sector on the glue sector is fully included.

As with IHQCD, it was arranged that the theory is asymptotically AdS in the UV up to logarithmic corrections in the bulk coordinate. The function $V_{0f}(\lambda)$ is such that the potential $V_g(\lambda) - x_f V_{0f}(\lambda)$, when the tachyon has not condensed ($\tau = 0$) has an extremum [4] at a finite value $\lambda = \lambda_*$. As we approach the Banks-Zaks region [2], $x_f \to \frac{11}{2}$, the value of λ_* approaches zero. Without the tachyon, $\tau = 0$, the equations of motion imply that also $\beta(\lambda_*) = 0$, i.e., λ_* is an IR fixed point. When the dynamics of τ is included, the system approaches λ_* but is driven away from it as long as $x_f < x_c$ (see figure 7 of [26]).

The dimension of the chiral condensate was calculated in the IR fixed point theory from the bulk equations. It was found that it decreases monotonically with x_f for reasonably chosen potentials. It crossed the value 2 at $x_f = x_c$ where x_c corresponds to the end of the conformal window as argued in [66].

The lower edge of the conformal window x_c lies in the vicinity of 4. Requiring the holographic β-functions to match with QCD in the UV, we find that

$$3.7 \lesssim x_c \lesssim 4.2, \tag{1.5}$$

where the bounds are not strict but hold approximately for potentials that have smooth λ-dependence in the UV.

There is also a phenomenological heuristic argument for the value $x_c \approx 4$, simply from counting degrees of freedom. At low T chiral symmetry is broken and the massless degrees of freedom are N_f^2 Goldstone bosons. At large T there are $2N_c^2 + \frac{7}{2}N_cN_f$ weakly coupled degrees of freedom. These numbers are equal for $x_f = 4$. Conformal window and the location of its edge was also discussed within holographic frameworks related to V-QCD in [45, 67–69].

Apart from x_f, there is a single parameter in the theory, namely $\frac{m}{\Lambda_{\text{QCD}}}$ where m is the UV value of the (flavor independent) quark mass. For each value of x_f, the bulk equations were solved with fixed sources corresponding to fixed m, Λ_{QCD}. The vevs were determined such that the solution is "regular" in the IR. The notion of regularity is tricky even in the case of IHQCD (pure glue), as there is a naked singularity in the far IR. For the dilaton this has been settled in [30–35]. For the tachyon the notion of regularity is different and has been studied in detail in [38, 39].

---

[4] The extremum may exist for all $0 < x_f < \frac{11}{2}$ or may disappear at some small x_f. No changes in the phase structure at zero temperature for these two cases were found in [26].

The regularity condition was implemented in the IR. After solving the equations from the IR to the UV (this was done mostly numerically), there is a single parameter that determines the solutions as well as the UV coupling constants and vevs, and this is a real number τ_0 controlling the value of the tachyon in the IR. This number reflects the single dimensionless parameter $\frac{m}{\Lambda_{\text{QCD}}}$ of the theory.

For different values of x_f and m the following qualitatively different regions were found in [26]:

- When $x_c \leq x_f < 11/2$ and $m = 0$, the theory flows to an IR fixed point. The IR conformal field theory is weakly coupled near $x_f = \frac{11}{2}$ and strongly coupled in the vicinity of x_c. Chiral symmetry is unbroken in this regime (this is known as the conformal window).

- When $x_c \leq x_f < 11/2$ and $m \neq 0$, the tachyon has a nontrivial profile, and there is a single solution with the given source, which is "regular" in the IR. The IR theory is a theory with a mass gap.

- When $0 < x_f < x_c$ and $m = 0$, there is an infinite number of regular solutions with nontrivial tachyon profile, and a special solution with an identically vanishing tachyon and a nontrivial IR fixed point. The infinite number of solutions with nontrivial tachyon are classified by their number of zeros. The solution with the lowest free energy is the one with no zeros.

- When $0 < x_f < x_c$ and $m \neq 0$, the theory has vacua with nontrivial profile for the tachyon. For every non-zero m, there is a finite number of regular solutions that grows as m approaches zero.

In [26] two large classes of tachyon potentials were identified. Potentials in class I, have $a(\lambda)$ constant in (1.4). In this case the tachyon diverges exponentially in the IR for the regular solution

$$\tau \underset{r \to \infty}{\sim} \tau_0 \exp\left[Cr\right], \tag{1.6}$$

where C is a known constant (see appendix B) and τ_0 is the only integration constant controlling the solution. It determines the source (mass) in the UV. Potentials in class II, have $a(\lambda) \sim \lambda^{\frac{2}{3}}$ as $\lambda \to \infty$, and a tachyon that diverges in a milder way in the IR as

$$\tau \underset{r \to \infty}{\sim} C\sqrt{r - r_1}, \tag{1.7}$$

where again C is known and r_1 is the single integration constant controlling the regular solution. The qualitative conclusions above and below were valid for both classes of potentials.

In the region $x_f < x_c$ where several solutions exist, there is a interesting relation between the IR value τ_0 controlling the regular solutions, and the UV parameters, namely m. This is determined numerically, and a relevant plot describing the relation between m and τ_0 at fixed x_f is in figure 1.

The solutions are characterized by the number of times n the tachyon field changes sign as it evolves from the UV to the IR. For all values of m there is a single solution with

no tachyon zeroes. In addition, for each positive n there are two solutions[5] which exist within a finite range $0 < m < m_n$, where the limiting value m_n decreases with increasing n, and one solution for $m = 0$. In particular, for large enough fixed m, we find that only the solution without tachyon zeroes exists.

For $m \neq 0$, out of all regular solutions, the "first" one without tachyon zeroes has the smallest free energy. The same is true for $m = 0$, namely the solution with nontrivial tachyon without zeroes is energetically favored over the solutions with positive n as well as over the special solution with identically vanishing tachyon, which appears only for $m = 0$ and would leave chiral symmetry unbroken. Therefore, chiral symmetry is broken for $x_f < x_c$.

In the region just below x_c, [26] found Miransky scaling for the chiral condensate. As $x_f \to x_c$,

$$\sigma = \langle \bar{q} q \rangle \sim \Lambda_{\text{QCD}}^3 \exp\left(-\frac{2\hat{K}}{\sqrt{x_c - x_f}} \right). \tag{1.8}$$

For $x \geq x_c$, let $m_{\text{IR}}(x)$ be the mass of the tachyon at the IR fixed point and $\ell_{\text{IR}}(x)$ the IR AdS radius. The coefficient $\hat{K}$ is then fixed as

$$\hat{K} = \frac{\pi}{\sqrt{\frac{d}{dx}\left[m_{\text{IR}}^2 \ell_{\text{IR}}^2 \right]_{x=x_c}}} . \tag{1.9}$$

The behavior at and below the conformal transition at $x_f = x_c$ is to a large extent independent of the details of the model. In particular, no information on the nonlinear terms in the tachyon EoM is needed or how the IR boundary conditions are fixed. In the same region, "walking" of gauge coupling is realized. The YM coupling flows from small values to values very near λ_*, remains approximately constant for many e-foldings of energy (in this regime the tachyon remains small), and then runs off to infinity, driven by a large value of the tachyon field in the IR. The walking is related to a long section of the solution which is similar to the one studied in earlier bottom-up models for walking [55–59].

The finite temperature analysis of V-QCD amounts to studying all black hole solutions with appropriate boundary conditions. To start with, any zero temperature solution becomes a candidate saddle point at finite temperature by compactifying time on a circle of radius β. Any other competing black hole solution must have the same boundary conditions as well as a regular horizon in the IR.

As the dilaton always has a nontrivial UV source, it will always have a nontrivial profile in the black-hole solutions. With the tachyon, things can be different. In the massless case, its source is zero. Therefore there are two possible options (as in the zero temperature configurations discussed above): either it is identically zero (if the vev $\langle \bar{q} q \rangle$ is also zero) or it is non-zero (implying a non-zero vev).

Therefore we have two large classes of black holes in the massless case: those with $\tau = 0$ and those with $\tau \neq 0$. We will first consider the tachyon-free class.

---

[5]As m and $-m$ are related by a chiral rotation by π, we can take $m \geq 0$.

1.2 Black holes without tachyon hair

If $\tau = 0$, we have black holes in a single scalar theory, with potential $V(\lambda) = V_g(\lambda) - x_f V_{0f}(\lambda)$ from (1.4). This is a potential with an extremum for $x_f \neq 0$[6] and no extremum when $x_f = 0$.

Black hole solutions for such potentials were discussed in generality in [33–35]. After fixing all invariances, they are characterised by a single IR constant, λ_h, the value of the dilaton at the horizon. The plot relating the temperature T to λ_h contains important information about the thermodynamics of such black holes. Small values of λ_h denote large black-holes whereas larger values of λ_h correspond to smaller black holes (smaller horizon size and entropy). In all plots of this paper, dilatonic black holes without tachyon hair are denoted by red lines in the respective (λ_h, T)-diagrams, and we shall call the corresponding function $T_u(\lambda_h)$.

When $x_f = 0$, λ can become arbitrarily large at zero temperature, implying that λ_h can also be arbitrarily large for the finite temperature configurations. At finite temperature there are two branches: large black holes which are stable and small black holes which are unstable. If $T_u'(\lambda_h) < 0$ the black-hole thermodynamics is stable, otherwise it is unstable. There is a minimum temperature above which such black holes exist as shown, for example, by the black line in figure 22 (left or right).

When $x_f > 0$, we have two possibilities. The first is that the potential $V_{\text{eff}}(\lambda) = V_g(\lambda) - x_f V_{0f}(\lambda)$ has an extremum at $\lambda \to \lambda_*(x)$ for all $0 < x_f < \frac{11}{2}$, with $\lambda_* \left(x_f \to \frac{11}{2} \right) \to 0$ and $\lambda_*(x_f \to 0) \to \infty$. The second is that such extremum only exists for $x > x_*$, where $x_* < x_c$. We shall denote these potentials with a star subscript.

At finite temperature, and when the potential V_{eff} has no extremum, the black hole without the tachyon hair exists for all positive λ_h. For the potentials studied here, function $T_u(\lambda_h)$ is qualitatively similar to the YM case ($x_f \to 0$) [33–35]. As shown in figure 17 (top-left) and in figure 19 (left), there are two black hole branches, which exist above some minimum temperature. The branch at low λ_h is thermodynamically stable, while the large-λ_h branch is unstable.

When the extremum is present, $0 < \lambda_h < \lambda_*(x)$. The temperature of the black-hole corresponding to $\lambda_h = \lambda_*(x)$ is $T = 0$, while that of $\lambda_h \to 0$ has $T \to \infty$. There is no minimum temperature here. For any temperature there is always at least one black-hole solution. There are several possibilities that are shown as red lines in figures 7 (left), 9 (top), 10 (left) and 12 (left).

When x_f is large, but still smaller than x_c, the $T = T_u(\lambda_h)$ relation is one-to-one but contains a bump (a change of concavity) like in figure 9 (top). Then this is accompanied by a crossover behavior, signaled by a bump in the trace of the stress tensor $(\epsilon - 3p)/T^4$, (aka interaction measure) as shown in figure 9 (bottom-right).

At low enough x_f, the relation $T = T_u(\lambda_h)$ is not always one-to-one, as can be seen in figure 10 (left) or in figure 22. Then there are points where $T_u'(\lambda_h) = 0$. In such a case there can be a first order transition between the stable branches of the black hole solutions. This is a remnant of the deconfining transition at $x_f = 0$ (pure YM). In figure 22 both left and

---

[6]The extremum may also exist only for x_f above some fixed x_*, see the discussion further below.
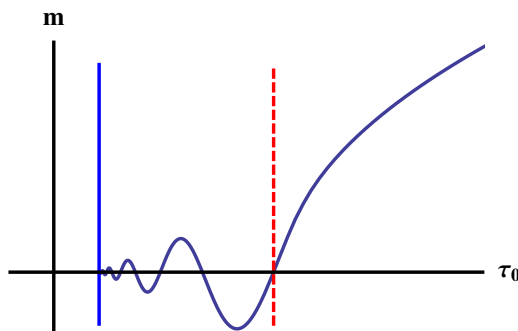
Figure 1. Plot of the UV Mass parameter m, as a function of the IR scale τ_0 in (1.6), for $x_f < x_c$. The vertical solid blue line marks the end-point of the existence of regular solutions. The dashed red line indicates the appearance of more than one regular solution with the same value of m.

right several curves in the (T, λ_h)-plane for different x_f indicate the successive structure of dilaton black holes (red lines). The black line corresponds to the pure YM ($x_f = 0$) limit.

When $x > x_c$ we are in the conformal window. The only black holes that exist here are those without tachyon hair. The relation $T = T_u(\lambda_h)$ is monotonic and there is a continuous transition to the black-hole phase at $T = 0^+$, as in the AdS case in the Poincaré patch. The thermodynamic functions, especially the interaction measure, show a crossover maximum at a temperature that is moving towards the UV as $x_f \to \frac{11}{2}$.

1.3 Black holes with tachyon hair and zero quark mass

When $\tau \neq 0$ we have black holes in the two scalar theory. The tachyon starts as $\sim r^3$ near the UV boundary as the source (quark mass) vanishes. In all plots of this paper, such black holes (with both dilaton and tachyon hair) are denoted by blue lines in the respective (λ_h, T)-diagrams, and we shall denote the corresponding functions by $T_b(\lambda_h)$. They are still one parameter solutions and can be parametrized again by the value λ_h of λ at the horizon, which translates into the temperature. These black holes usually exist for all $x_f \in]0, x_c[$ and our discussion below focuses in this region.

Because the presence of the nontrivial tachyon perturbs and annuls the possible nontrivial IR fixed point, for such black-holes, λ_h can take arbitrarily large values. This can be seen from the blue lines in figures 7 (left), 9 (top), 10 (left) and 12 (left). For all such black holes, the chiral condensate is determined by the regularity of the black hole solution. It decreases as λ_h decreases, and at some point it vanishes. At this point, the blue line in the (λ_h, T)-diagram merges with the red line corresponding to a λ_h that we call λ_{end} throughout the paper. This can be seen in all the figures mentioned above.

The shape of the blue line can vary as a function of x_f and the type of potential. There are three typical examples of shapes:

- Simple lines that are monotonic as the one depicted in figure 12 (left). This is an example of a monotonic blue branch where all such black-holes are thermodynamically unstable. Moreover, they have a minimum temperature. In such a case, they can never be thermodynamically dominant. At some temperature the vacuum thermal

solution is dominated by a dilaton black hole on the red line, and the chiral restoration transition is 1st order.

- Lines with two branches as the one depicted in figure 10 (left). Here the blue line has two parts one (to the left) that is thermodynamically stable and another to the right that is thermodynamically unstable. In such a case, the system is in the thermal vacuum solution at low enough temperatures, then jumps with a 1st order transition to the tachyon-hairy solution (the part of the blue line that is thick in figure 10 (left)) which still break chiral symmetry, and then eventually smoothly transits to the red line at the point where the blue and red lines merge, via a chirally-restoring 2nd order transition.[7]

- Lines with more than two branches as the one depicted in figure 11 (left). In this example the blue line has four branches, two unstable and two stable. There are in total three phase transitions here, first from the vacuum thermal solution to the rightmost blue thick branch, then to the intermediate thick blue branch and finally a 2nd order chirally restoring transition to the red branch at the point they touch. In this case there are two 1st order transitions between three chirally breaking phases, and a 2nd order one to the chirally symmetric phase.

A concrete overall view of the x_f dependence is presented in figure 2, in which $T(\lambda_h)$ is plotted for potentials of type II with SB normalisation (definitions specified later) for various x_f. One sees clearly how the pure (black) YM curve is approached for $x_f \to 0$. The thick curves represent stable phases; when a thick curve ends, the system makes a 1st order transition to the low T phase. When thick curves change from red to blue curves, a 2nd order transition to a chirally broken phase takes place. For a more accurate picture of small x_f, see figure 22.

1.4 The phase structure of different V-QCD models

There are three main ingredients that characterize a priori different QCD models which, however, have the same phase structure and qualitative behavior at zero temperature:

- The asymptotics of the tachyon solution in the IR. This is controlled by the behavior of the function $a(\lambda)$ in the tachyon potential in (1.4). When $a(\lambda)$ is constant, the tachyon diverges exponentially in the IR, and we call such potentials of type I. When $a(\lambda)$ diverges as $\lambda^{\frac{2}{3}}$ in the IR (λ large) then the tachyon diverges as a square root in the IR, and we call such potentials of type II.

- For any potential, the UV constant factor W_0 of $V_{0f}(\lambda)$ in (1.4), defined in (2.13) can vary in finite range, which in appropriate units is $]0, \frac{24}{11}]$, as in (2.21). We pick for each type of potential three indicative values of $\mathcal{L}_0^2 W_0$ that in general might

---

[7]It may also happen that the thermodynamically stable branch is only metastable, in which case the system jumps directly to the black hole branch without tachyon hair, and chiral symmetry is thus restored at this 1st order transition. The more complicated branch structure discussed in the next bullet may similarly contain metastable branches.
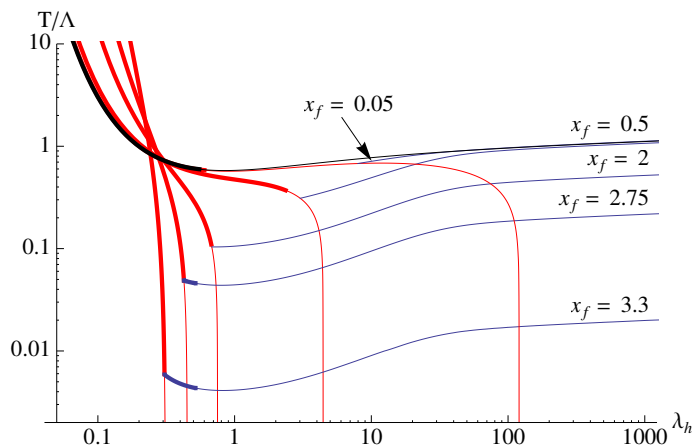
Figure 2. $T(\lambda_h)/\Lambda$ plotted for potentials of type II with SB normalisation (definitions specified in text) for various x_f marked on figure. Thick curves represent stable phases. For more details at small x_f, see figure 22.

give different physics, namely 0, $\frac{12}{11}$, and $\frac{24}{11}$.[8] We also consider x_f-dependent value, specified in (2.23) that corresponds to the normalization of the UV degrees of freedom of the free energy to the Stefan-Boltzmann limit of QCD.

- A final variation can be obtained on all of the above by using a glue potential $V_g(\lambda) - x_f V_{0f}(\lambda)$ in (1.4) that has

  (a) an extremum for all x_f in the appropriate range, $x_f \in]0, \frac{11}{2}[$.

  (b) an extremum only in part of this range, $x_* < x_f < \frac{11}{2}$. We will denote the potentials in this case by a star subscript.

According to the above options $\mathrm{PotI}_*(W_0 = 0)$ denotes a potential in the type I class, with $W_0 = 0$ and an IR critical point that exists only down to a finite x_*.

Let us then summarize the phase structure of the model as x_f and the temperature are varied (at zero quark mass). In general one expects the phase diagram of figure 8, so that for $0 < x_f < x_c$ there is the 1st order transition at finite temperature, which also separates the chirally symmetric and broken phases. For $x_f > x_c$ the low temperature and high temperature configurations correspond to a tachyonless black holes, and, one expects a continuous crossover between these two.

For the various potentials presented above, this phase diagram is indeed obtained in the zeroth approximation, but for $x_f < x_c$ there are additional details which depend on the choice of potentials as follows.

- For potentials I the phase structure depends strongly on the choice for W_0 (see figure 18). For the lowest value $W_0 = 0$, there is only one 1st order transition

---

[8]Notice that the exactly zero value of W_0 is actually excluded, because it predicts wrong anomalous dimensions for quark mass or the chiral condensate [26]. We anyhow consider it as the limiting case of the allowed solutions. Moreover, W_0 may exceed the upper limit of $24/11$, if x_f dependence is allowed.

at[9] $T = T_d$ for all $0 < x_f < x_c$, except possibly for x_f very close to x_c, where solving the phase diagram numerically becomes demanding. As W_0 is increased, a complicated structure appears near $x_f = x_c$, where we have two 1st order transitions between chirally broken phases, and the restoration of chiral symmetry at a 2nd order transition at even higher temperature. At even higher W_0 the 1st order transitions combine again into a single one, but the separate 2nd order transition continues to exist for x_f close to x_c. At low x_f, there is also a surprising change as W_0 increases. The chiral symmetry breaking phases disappear, but there is a 1st order transition between two chirally symmetric black hole phases at a finite temperature instead.

- For potentials II the dependence on W_0 is milder (see figures 13–16). At high W_0, for low x_f up to some value x_χ, there is only the 1st order transition at[10] $T = T_d$. When $x_\chi < x_f < x_c$, the chiral symmetry restoration takes again place at a 2nd order transition at T_χ such that $T_\chi > T_d$. For decreasing W_0, x_χ increases, and finally disappears by joining with x_c.

- For the potentials I$_*$, the phase structure is the standard one for high x_f, i.e., a 2nd order transition and a 1st order one with critical temperatures $T_\chi > T_d$ within a range $x_\chi < x_f < x_c$, with the former separating the chirally symmetric and broken phases (see figure 19). For lower x_f there is only one 1st order transition. For $x_f \lesssim 2$, in the region where the effective potential does not admit an extremum, chiral symmetry is intact at all temperatures. We find a single 1st order transition between chirally symmetric thermal gas and black hole phases.

- For potentials II$_*$, the phase structure is simple (see figure 17): there is a single 1st order transition for all $x_f \in]0, x_c[$. In particular, the system is in a chirally broken phase at low temperatures, even in the region of low x_f where the effective potential does not have an extremum.

2 Defining V-QCD

2.1 Gravity action of the model

The action of V-QCD is [26]

$$S = M^3 N_c^2 \int d^5x \, \mathcal{L} \equiv \frac{1}{16\pi G_5} \int d^5x \, \mathcal{L}, \tag{2.1}$$

where[11]

$$\mathcal{L} = \left[\sqrt{-g} \left(R - \frac{4}{3} \frac{(\partial\lambda)^2}{\lambda^2} + V_g(\lambda) \right) - V_f(\lambda, \tau) \sqrt{\det(g_{ab} + \kappa(\lambda, \tau)\partial_a\tau \, \partial_b\tau)} \right]$$

$$= \sqrt{-g} \left[R + \left[-\frac{4}{3} g^{\mu\nu}\partial_\mu\phi\partial_\nu\phi + V_g(\lambda) \right] - V_f(\lambda, \tau)\sqrt{1 + g^{rr}\kappa(\lambda(r))\tau'(r)^2} \right]. \tag{2.2}$$

---

[9]$T_d = T_h$ in figure 18.

[10]$T_\chi = T_{\text{end}}$ of figures 13–16 when it is in the stable brach.

[11]Notice that for notational simplicity we have absorbed a factor of x_f, which is visible in eq. (1.3), into $V_f(\lambda, \tau)$. See also eq. (2.10) below.

The metric Ansatz is

$$ds^2 = b^2(r)\left[-f(r)dt^2 + d\mathbf{x}^2 + \frac{dr^2}{f(r)}\right], \quad b(r) = e^{A(r)} \underset{r\to 0}{\sim} \frac{\mathcal{L}_{\text{UV}}}{r}, \tag{2.3}$$

and the two scalar functions, $1/\lambda$ sourcing F^2 and τ sourcing $\langle\bar{q}q\rangle$, are

$$\lambda = \lambda(r) = e^{\phi(r)}, \quad \tau = \tau(r). \tag{2.4}$$

In the second form $\sqrt{-g}$ has been factored out of the DBI action. The Gibbons-Hawking counter term would be

$$S_{GH} = -\int d^4x \sqrt{-\gamma}\left[2K + \frac{6}{\mathcal{L}_{\text{UV}}} + \frac{\mathcal{L}_{\text{UV}}}{2}R(\gamma)\right], \tag{2.5}$$

with, for a hypersurface $r =$const,

$$K = \frac{\sqrt{f}}{2b}\left(8\frac{b'(r)}{b} + \frac{f'(r)}{f}\right). \tag{2.6}$$

Notice also that we have set the gauge fields $A_{L,R}$, which are dual to the left and right handed fermion currents, to zero, and neglected the Wess-Zumino terms. These terms do not affect the thermodynamics of the models.

The background solution of the dilaton $\lambda(r)$ and the warp factor $A(r)$ are identified as the 't Hooft coupling and the logarithm of the energy scale of the dual field theory, respectively [30–32]. As a matter of convention, we shall fix the normalisation of $\lambda(r)$ so that its relation to the perturbative QCD coupling is

$$\lambda(r) = \frac{g^2(b(r))}{8\pi^2}. \tag{2.7}$$

The results of the model are independent of this normalisation, changing $\lambda \to \lambda/\lambda_0$ one simply has to change the potentials by $V(\lambda) \to V(\lambda_0\lambda)$. The convention of [26], for example, is obtained by shifting by $\lambda_0 = 1/(8\pi^2)$.

Important ingredients of the model are the relation of the bulk fields at r to the QCD beta and quark mass anomalous dimension functions evaluated for a coupling at scale $b(r)$. Motivated by the connection to field theory, one defines

$$\beta = \frac{d\lambda}{db/b} = \lambda'(A) = -b_0\lambda^2 - b_1\lambda^3 - b_2\lambda^4\ldots, \quad \gamma = \tau'(A). \tag{2.8}$$

Matching with the perturbative expansion of the QCD beta function gives

$$b_0 = \frac{1}{3}(11 - 2x_f), \quad b_1 = \frac{1}{6}(34 - 13x_f). \tag{2.9}$$

The action contains the gluonic potential $V_g(\lambda)$ and the fermionic potential $V_f(\lambda,\tau)$, which will be specified to the form

$$V_f(\lambda,\tau) = x_f V_{f0}(\lambda)e^{-a(\lambda)\tau^2}. \tag{2.10}$$

The detailed form of these and the functions $\kappa(\lambda)$, $a(\lambda)$ will be discussed in the following subsections.

2.2 Construction of the potentials

The potentials can be constructed in stages. First one fixes the potentials $V_g(\lambda)$ and $V_{f0}(\lambda)$ up to order λ^2 in the UV, using the two scheme independent coefficients of the beta function. This analysis is simplified by the fact that the tachyon decouples in the UV. Next one fixes the UV behavior of the functions $a(\lambda)$ and $\kappa(\lambda)$, which parametrize the tachyon dependence of the action using the similarly scheme independent UV running properties of the quark mass and the condensate. Finally, one fixes the large λ behavior of the potentials by requiring that the model reproduces known features of QCD in the IR, such as confinement, linear Regge trajectories, and reasonable zero-temperature phase structure. We shall discuss the various steps in detail below (see also [26]).

2.2.1 The potentials from the beta function in the UV

In the UV, since the tachyon vanishes much faster than the dilaton, we can first set it to zero. Then the dilaton profile can be linked to the effective potential $V_{\rm eff}(\lambda) = V_g(\lambda) - x_f V_{f0}(\lambda)$ [26] by using Einstein's equations [30–32]. Defining $\beta = d\lambda/d\ln b = -b_0\lambda^2 - b_1\lambda^3$, to order λ^2,

$$V_g - x_f V_{0f} = \frac{12}{\mathcal{L}_{\rm UV}^2} \exp\left[-\frac{8}{9}\int_0^\lambda d\lambda \frac{\beta}{\lambda^2}\right]\left(1 - \frac{\beta^2}{9\lambda^2}\right) \tag{2.11}$$

$$= \frac{12}{\mathcal{L}_{\rm UV}^2}\left[1 + \frac{8}{9}b_0\lambda + \left(\frac{23}{81}b_0^2 + \frac{4}{9}b_1\right)\lambda^2\right] \tag{2.12}$$

$$= V_0 - x_f W_0 + (V_1 - x_f W_1)\lambda + (V_2 - x_f W_2)\lambda^2, \tag{2.13}$$

where we expanded

$$V_g = V_0 + V_1\lambda + V_2\lambda^2 + \mathcal{O}(\lambda^3), \quad V_{f0} = W_0 + W_1\lambda + W_2\lambda^2 + \mathcal{O}(\lambda^3), \tag{2.14}$$

and where we have introduced an x_f dependent AdS radius

$$\mathcal{L}_{\rm UV} = \mathcal{L}(x_f). \tag{2.15}$$

Applying equation (2.12) for $x_f = 0$ we have for the gluonic potential

$$V_g = \frac{12}{\mathcal{L}_0^2}\left(1 + \frac{8}{9}b_0^{\rm YM}\lambda + \frac{23(b_0^{\rm YM})^2 + 36b_1^{\rm YM}}{81}\lambda^2\right) \tag{2.16}$$

$$= \frac{12}{\mathcal{L}_0^2}\left(1 + \frac{88}{27}\lambda + \frac{4619}{729}\lambda^2\right), \tag{2.17}$$

where $b_i^{\rm YM}$ are the values of b_i for $x_f = 0$ and $\mathcal{L}_0 = \mathcal{L}(x_f = 0)$. In practice, one usually sets the (dimensionful) quantity $\mathcal{L}_0 = 1$.

By using equations (2.12) and (2.13) one can now solve for the coefficients of the fermionic potential:

$$x_f \mathcal{L}_0^2 W_0 = 12\left(1 - \frac{\mathcal{L}_0^2}{\mathcal{L}_{\text{UV}}^2}\right), \tag{2.18}$$

$$x_f \mathcal{L}_0^2 W_1 = \frac{32}{3}\left(b_0^{\text{YM}} - b_0 \frac{\mathcal{L}_0^2}{\mathcal{L}_{\text{UV}}^2}\right) = \frac{12 \cdot 8}{27}\left[11 - (11 - 2x_f)\frac{\mathcal{L}_0^2}{\mathcal{L}_{\text{UV}}^2}\right], \tag{2.19}$$

$$x_f \mathcal{L}_0^2 W_2 = \frac{12}{81}\left[23(b_0^{\text{YM}})^2 + 36b_1^{\text{YM}} - (23b_0^2 + 36b_1)\frac{\mathcal{L}_0^2}{\mathcal{L}_{\text{UV}}^2}\right] \tag{2.20}$$

$$= \frac{12}{729}\left[4619 - (4619 - 1714x_f + 92x_f^2)\frac{\mathcal{L}_0^2}{\mathcal{L}_{\text{UV}}^2}\right].$$

These equations still involve one free parameter, which can be taken to be either W_0 or $\mathcal{L}_{\text{UV}}$. We shall study two ways to fix this parameter. First, we can take W_0 to be constant. In this case [26]

$$0 \leq \mathcal{L}_0^2 W_0 \leq \frac{24}{11}, \tag{2.21}$$

and the x_f-dependent AdS radius is given by

$$\mathcal{L}_{\text{UV}} = \frac{\mathcal{L}_0}{\sqrt{1 - \frac{1}{12}\mathcal{L}_0^2 W_0 \cdot x_f}}. \tag{2.22}$$

Second, we can make a special x_f-dependent choice, which (as we shall show later) automatically normalises the free energy at large T to Stefan-Boltzmann:

$$\mathcal{L}_{\text{UV}} = \mathcal{L}_0\left(1 + \frac{7}{4}x_f\right)^{1/3}. \tag{2.23}$$

Further, we have to fix the λ dependence of the functions $a(\lambda)$ and $\kappa(\lambda)$ in the tachyon part

$$x_f V_{f0}(\lambda) e^{-a(\lambda)\tau^2}\sqrt{1 + g^{rr}\kappa(\lambda(r))\dot{\tau}^2}, \tag{2.24}$$

of the action, where $g^{rr} = f/b^2$. The leading logarithmic term to the UV expansion of the tachyon should be (remember that the energy dimension of τ is -1)

$$\tau(r)/\mathcal{L}_{\text{UV}} = mr\left(-\ln \Lambda r\right)^{-\frac{\gamma_0}{b_0}} = mr\left(-\ln \Lambda r\right)^{-\frac{3}{2b_0}} \tag{2.25}$$

to satisfy the scheme independent UV running of the quark mass. Here $\gamma_0 = 3/2$ is the leading coefficient of the anomalous dimension of the quark mass in QCD, $\gamma(\lambda) = \gamma_0\lambda + \cdots$. By using the tachyon equation of motion one sees that this requires that for small λ,

$$\frac{\kappa(\lambda)}{a(\lambda)} = \frac{2}{3}\mathcal{L}_{\text{UV}}^2\left[1 - \left(\frac{8}{9}b_0 + 1\right)\lambda + \lambda^2 + \cdots\right]. \tag{2.26}$$

2.2.2 Large λ behavior of the potentials

To specify the full potential $V_g(\lambda) - x_f V_{f0}(\lambda) e^{-a(\lambda)\tau^2}$ we have to continue the small λ expansions to large λ. The guideline is quark confinement and chiral symmetry breaking at small x_f and the appearance of an infrared fixed point at some $x_f = x_c$ (see [26]). Since there is no unique path to the result, we present the final forms of the potentials we use and motivate them.

We use the gluonic potential

$$V_g(\lambda) = \frac{12}{\mathcal{L}_0^2}\left[1 + \frac{88\lambda}{27} + \frac{4619\lambda^2}{729}\frac{\sqrt{1+\ln(1+\lambda)}}{(1+\lambda)^{2/3}}\right] \tag{2.27}$$

which is constructed from the expansion (2.16) by simply multiplying the λ^2 term by the confinement factor

$$\frac{\sqrt{1+\ln(1+\lambda)}}{(1+\lambda)^{2/3}} . \tag{2.28}$$

Then V_g has the proper large-λ behavior [30–32] but the small-λ behavior is left intact. One could add scale factors of type λ/λ_0 containing more parameters.

For the fermionic potential V_{f0} in

$$V_f(\lambda, \tau) = x_f V_{f0}(\lambda) e^{-a(\lambda)\tau^2} \tag{2.29}$$

we consider two different choices. The first one is obtained directly using (2.18)–(2.20)

$$V_{f0} = \frac{12}{\mathcal{L}_{\mathrm{UV}}^2 x_f}\left[\frac{\mathcal{L}_{\mathrm{UV}}^2}{\mathcal{L}_0^2} - 1 + \frac{8}{27}\left(11\frac{\mathcal{L}_{\mathrm{UV}}^2}{\mathcal{L}_0^2} - 11 + 2x_f\right)\lambda \right. \tag{2.30}$$
$$\left. + \frac{1}{729}\left(4619\frac{\mathcal{L}_{\mathrm{UV}}^2}{\mathcal{L}_0^2} - 4619 + 1714x_f - 92x_f^2\right)\lambda^2\right].$$

Here one could as well use the parameter W_0 which is related to $\mathcal{L}_{\mathrm{UV}}$ by

$$\frac{\mathcal{L}_0^2}{\mathcal{L}_{\mathrm{UV}}^2} = 1 - \frac{x_f \mathcal{L}_0^2 W_0}{12}. \tag{2.31}$$

For this choice the effective potential

$$V_{\mathrm{eff}}(\lambda) = V_g(\lambda) - x_f V_{f0}(\lambda) \tag{2.32}$$

has a single maximum at finite positive $\lambda = \lambda_*$ for all $0 < x_f < 11/2$, indicating a (possible) infra-red fixed point.

The second choice is obtained introducing the confinement factor (2.28) also for the fermionic potential, i.e.,

$$V_{f0} = \frac{12}{\mathcal{L}_{\mathrm{UV}}^2 x_f}\left[\frac{\mathcal{L}_{\mathrm{UV}}^2}{\mathcal{L}_0^2} - 1 + \frac{8}{27}\left(11\frac{\mathcal{L}_{\mathrm{UV}}^2}{\mathcal{L}_0^2} - 11 + 2x_f\right)\lambda \right. \tag{2.33}$$
$$\left. + \frac{1}{729}\left(4619\frac{\mathcal{L}_{\mathrm{UV}}^2}{\mathcal{L}_0^2} - 4619 + 1714x_f - 92x_f^2\right)\lambda^2\frac{\sqrt{1+\ln(1+\lambda)}}{(1+\lambda)^{2/3}}\right].$$

Now the effective potential has a maximum only at large x_f. To see this concretely, consider again the case (2.23). The asymptotic large-λ behavior of $V_g - x_f V_{f0}$ now is $\lambda^{4/3}\sqrt{\ln\lambda}$ times the function

$$\frac{18476}{243} - 4\frac{4619(1 + \frac{7}{4}x_f)^{2/3} - 4619 + 1714x_f - 92x_f^2}{243(1 + \frac{7}{4}x_f)^{2/3}}. \tag{2.34}$$

This function is positive for small x_f, negative at large x_f ($< 11/2$) and has a zero at $x_f = 3.26817$. Thus there is a (possible) fixed point λ_* only for $3.26817 < x_f < 11/2$.

Let us then discuss the IR behavior of the potentials a and κ which appear in the tachyon DBI action. For the function κ we will consider the large-λ asymptotics

$$\kappa(\lambda) \underset{\lambda\to\infty}{\sim} \lambda^{-4/3}. \tag{2.35}$$

This is motivated by the fact that in the action the combination $\kappa(\lambda)/b^2$ has the same asymptotics as $1/b_s^2$ at large λ, where $b_s = b\lambda^{2/3}$ is the metric factor b in the string frame. To ensure that the fractional exponent limit at large λ does not spoil analyticity at small λ, we replace $\lambda^{4/3}$ by $(1 + \#\lambda)^{4/3}$ in the expression for $\kappa(\lambda)$.

More precisely, two qualitatively different, acceptable choices for the IR asymptotics of a (and κ) were identified in [26]. These are produced by the following two choices. The first choice has

$$a(\lambda) = \frac{3}{2}\frac{1}{\mathcal{L}_{\mathrm{UV}}^2}, \quad \kappa(\lambda) = \frac{1}{[1 + \frac{3}{4}(\frac{8}{9}b_0 + 1)\lambda]^{4/3}} = \frac{1}{\left(1 + \frac{115 - 16x_f}{36}\lambda\right)^{4/3}}, \tag{2.36}$$

and leads to tachyon growing exponentially at large r,

$$\tau(r) \underset{r\to\infty}{\sim} \tau_0 e^{Cr} \tag{2.37}$$

where C is a known constant (see appendix B) and τ_0 parametrises the solutions. The second choice is given by

$$\kappa(\lambda) = \frac{1}{(1 + \lambda)^{4/3}}, \quad a(\lambda) = \kappa(\lambda)\frac{3}{2\mathcal{L}_{\mathrm{UV}}^2}\left[1 + \left(\frac{8}{9}b_0 + 1\right)\lambda + \lambda^2\right] \tag{2.38}$$

and for them the leading divergence is

$$\tau(r) \underset{r\to\infty}{\sim} C\sqrt{r - r_1}, \tag{2.39}$$

where the constant C is again known and now r_1 parametrises the solutions. To select this solution, it is required that the last term in the square brackets in (2.38) grows faster than $\lambda^{4/3}$.

Finally, let us summarize our choices for acceptable potentials. We always keep V_g fixed to the expression (2.27) and choose V_{f0}, a, and κ as follows:

- *Potentials I*: We take V_{f0} as in equation (2.30), so that the fixed point λ_* exists for all $0 < x_f < 11/2$. For a and κ we use the choice of equations (2.36), which lead to exponentially diverging tachyon in the IR.

- *Potentials II*: We take again V_{f0} from equation (2.30), but use the other choice (2.38) for a and κ. Then the tachyon diverges as $\tau \sim \sqrt{r}$ in the IR.

- *Potentials I*$_*$: We use now the fermionic potential V_{f0} of equation (2.33), which contains the confinement factor. Thus the extremum exists only within the interval $3.26817 < x_f < 11/2$. For a and κ we use the choice of equations (2.36), which lead to exponentially diverging tachyon in the IR.

- *Potentials II*$_*$: We use V_{f0} with the confinement factor, but use the other choice (2.38) for a and κ. Then the fixed point exist only for large x_f, and the tachyon diverges as $\tau \sim \sqrt{r}$ in the IR.

To fully pin down the potentials, we also need to specify the value of W_0 (or $\mathcal{L}_{\rm UV}$) which is used. We choose four reference values:

- $W_0 = 0$ (and constant). This is the lower bound of W_0. Actually, exactly zero W_0 is not acceptable because the anomalous dimensions of the quark mass and the chiral condensate do not sum up to zero. This case is nevertheless interesting as it is the limit of acceptable solutions.

- $W_0 = 12/11$. This is the standard choice studied in [26].

- $W_0 = 24/11$. For constant W_0, this is the largest possible value, for which $\mathcal{L}_{\rm UV} \to \infty$ as $x_f \to 11/2$.

- W_0 (and $\mathcal{L}_{\rm UV}$) fixed such that the free energy automatically matches with the standard Stefan-Boltzmann result at high temperature with the correct number of degrees of freedom (see eq. (2.23) and the discussion in section 3.4 below).

An ongoing work [70] studies the meson spectra in this model. As it turns out, the potentials I and I$_*$ admit linear "Regge" trajectories, so that the quadratic masses are asymptotically linear in the excitation number, $m_n^2 \sim n$, independently of the other quantum numbers. Potentials II and II$_*$, however, have linear trajectories only in the glueball sector, while the other trajectories are quadratic, $m_n^2 \sim n^2$. As linear trajectories are expected in QCD, this observation favors potentials I and I$_*$.

2.2.3 IR fixed point and the BF bound for the tachyon

Now that the potentials are defined, one can check that they satisfy an important requirement: they permit the determination of the bulk tachyon mass and, equating this with the Breitenlohner-Freedman (BF) instability bound, the determination of the start of the conformal window. Take $\tau(r) = 0$ (there is no chiral symmetry breaking in the conformal window) and note that at small λ, $V_g(\lambda) - x_f V_{f0}(\lambda) > 0$. However, $V_{f0}(\lambda)$ grows faster and the conformal window starts at the value λ_* defined by the vanishing derivative

$$V_g'(\lambda_*) - x_f V_{f0}'(\lambda_*) = 0. \tag{2.40}$$

	PotI	PotI$_*$	PotII	PotII$_*$
$W_0 = 0$	4.10209	4.33334	4.17825	4.38493
$W_0 = 12/11$	3.99591	4.33334	4.07968	4.38493
$W_0 = 24/11$	3.71607	4.33334	3.80086	4.38493
W_0 SB	3.59172	4.33334	3.70008	4.38493

Table 1. The critical values x_c for the various potentials. Notice that for the types I$_*$ and II$_*$, x_c is independent of W_0.

Given λ_* one defines an IR AdS radius

$$\frac{12}{\mathcal{L}_{\rm IR}^2} = V_g(\lambda_*) - x_f V_{f0}(\lambda_*), \quad \mathcal{L}_{\rm UV} > \mathcal{L}_{\rm IR}. \tag{2.41}$$

The tachyon mass at λ_* in units of $\mathcal{L}_{\rm IR}$ becomes

$$- m_{\rm IR}^2 \mathcal{L}_{\rm IR}^2 = \frac{24a(\lambda_*)}{\kappa(\lambda_*)[V_g(\lambda_*) - x_f V_{f0}(\lambda_*)]}. \tag{2.42}$$

Gravity solutions with $\tau = 0$ are stable when $m_{\rm IR}^2 \mathcal{L}_{\rm IR}^2 > -4$; the conformal window thus starts when (2.42), as a function of x_f, has the value 4.

Eq. (2.42) can be evaluated for the two choices of a, κ above. For the choice (2.36) (types I and I$_*$) the equation becomes

$$\frac{36[1 + \frac{1}{36}(115 - 16x_f)\lambda_*]^{4/3}}{\mathcal{L}_{\rm UV}^2[V_g(\lambda_*) - x_f V_{f0}(\lambda_*)]} = 4 . \tag{2.43}$$

For the choice (2.38) (types II and II$_*$), the x_c-equation (2.42) has the form

$$\frac{36[1 + \frac{1}{27}(115 - 16x_f)\lambda_* + \lambda^{*2}]}{\mathcal{L}_{\rm UV}^2[V_g(\lambda_*) - x_f V_{f0}(\lambda_*)]} = 4 . \tag{2.44}$$

The values of x_c can then be calculated by inserting the potential $V_g - x_f V_{f0}$ and the chosen value for W_0 in these equations. The critical values for the potentials listed above are given in table 1.

The x_f-dependence of the tachyon mass for all the potential choices suggested above is shown in figure 3. The critical value x_c is the rightmost point where the curve intersects the horizontal dashed line where the BF bound is saturated. For potentials I$_*$ and II$_*$ (solid magenta curves) the fixed point only exists for $x_* < x_f < 11/2$ with $x_* \simeq 3.27$. In this case the tachyon mass diverges as x approaches x_* from above.

From (2.43) and (2.44) one sees, using the asymptotics of the potentials (see eq. (4.3) below), that $-m_{\rm IR}^2 \mathcal{L}_{\rm IR}^2 \sim 1/\sqrt{\ln(1/x_f)}$ for type I and $-m_{\rm IR}^2 \mathcal{L}_{\rm IR}^2 \sim 1/x_f$ for type II as $x_f \to 0$. They thus behave completely differently in this limit, for type I the mass vanishes, for type II it grows without bounds. In particular, for potentials I and for low x_f the (absolute value of the squared) tachyon mass dives below the BF bound. This means that the existence of a solution with a nontrivial tachyon profile and zero quark mass is
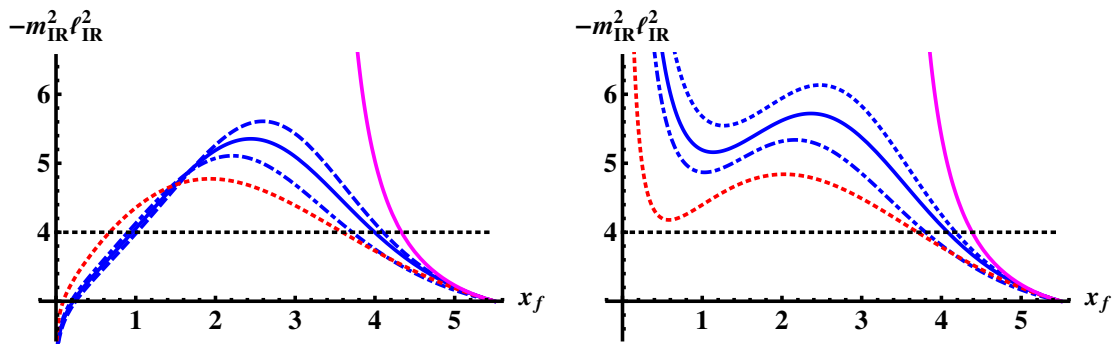
Figure 3. The squared tachyon mass at the IR fixed point, see eqs.(2.43) and (2.44). *Left*: potentials I; *Right*: potentials II. The blue curves give the masses for constant W_0. The dashed, solid and dotdashed curves have $W_0 = 0$, 12/11, and 24/11, respectively. The dotted red curves have W_0 fixed according to the Stefan-Boltzmann normalization of the free energy in the UV. The solid magenta (uppermost) curves are for potentials I$_*$ and II$_*$, for which the tachyon mass is independent of W_0. The black dotted horizontal line marks the BF bound.

not guaranteed [26], which means that chiral symmetry could remain intact even at low temperatures. However, in most of the cases, such a solution anyhow exists all the way down to $x_f = 0$, and the expected picture with chiral symmetry breaking is obtained. We shall discuss this issue in more detail below.

3 V-QCD at finite temperature: equations and their solution

The V-QCD action has two kinds of vacua at finite temperature, either with identically vanishing tachyon or with nontrivial tachyon profile. The tachyonless black hole solutions can be constructed in the same way as in the Yang-Mills case [33–35]. Below most of the discussion will in principle assume the presence of the tachyon, but the construction for the solutions without the tachyon can be obtained simply by setting $\tau = 0$ everywhere.

3.1 Equations and numerical solution

The goal now is to find numerical solutions of the Einstein's equations for the metric functions $b(r) = e^{A(r)}$, $f(r)$ and the scalars $\lambda(r)$, $\tau(r)$, satisfying

$$f(r_h) = 0, \quad f(0) = 1, \quad b(r) \underset{r \to 0}{\sim} \frac{\mathcal{L}_{\text{UV}}}{r}, \tag{3.1}$$

where r_h marks the location of the horizon.

Due to the singular behavior of the solutions near the UV boundary ($r \to 0$), it proves to be convenient to use $A = \ln b$ as a coordinate instead of r in the numerical solution. Carrying out this transformation, one finds that the combination

$$q(A) = e^A \frac{dr}{dA} = -\frac{1}{W} \tag{3.2}$$

appears naturally. This is just a rewriting of the superpotential

$$W = -\frac{\dot{b}}{b^2} = -e^{-A} \frac{dA}{dr}. \tag{3.3}$$

The equations of motion then become

$$12 - 6\frac{q'}{q} + \frac{4}{3}\frac{\lambda'^2}{\lambda^2} + 3\frac{f'}{f} = \frac{q^2}{f}\left(V_g - V_f\sqrt{1 + f\kappa\tau'^2/q^2}\right), \tag{3.4}$$

$$12 - \frac{4}{3}\frac{\lambda'^2}{\lambda^2} + 3\frac{f'}{f} = \frac{q^2}{f}\left(V_g - \frac{V_f}{\sqrt{1 + f\kappa\tau'^2/q^2}}\right), \tag{3.5}$$

$$4 - \frac{q'}{q} + \frac{f''}{f'} = 0, \tag{3.6}$$

$$\tau'' + \left(4 - \frac{q'}{q} + \frac{f'}{f} + \lambda'\frac{\partial\ln\kappa}{\partial\lambda} + \lambda'\frac{\partial\ln V_f}{\partial\lambda}\right)\tau' = -\frac{f\kappa}{q^2}\left(4 + \frac{f'}{2f} + \frac{\lambda'}{2}\frac{\partial\ln\kappa}{\partial\lambda} + \lambda'\frac{\partial\ln V_f}{\partial\lambda}\right)\tau'^3$$
$$+ \frac{\partial\ln V_f}{\partial\tau}\tau'^2 + \frac{q^2}{f\kappa}\frac{\partial\ln V_f}{\partial\tau}, \tag{3.7}$$

$$\frac{\lambda''}{\lambda} + \frac{f'}{f}\frac{\lambda'}{\lambda} + 4\frac{\lambda'}{\lambda} - \frac{\lambda'^2}{\lambda^2} - \frac{q'}{q}\frac{\lambda'}{\lambda} = -\frac{3}{8}\frac{q^2\lambda}{f}\left(\frac{\partial V_g}{\partial\lambda} - \frac{\partial V_f}{\partial\lambda}\sqrt{1 + \frac{f}{q^2}\kappa\tau'^2} - \frac{f}{2q^2}\frac{V_f\frac{d\kappa}{d\lambda}\tau'^2}{\sqrt{1 + \frac{f}{q^2}\kappa\tau'^2}}\right). \tag{3.8}$$

Here the prime denotes differentiation with respect to A. Near the UV boundary $r = 0$,

$$A = \ln b = \ln\frac{\mathcal{L}_{\mathrm{UV}}}{r} \to +\infty. \tag{3.9}$$

The range of A thus is $A_h < A < +\infty$, where A_h is the horizon,

$$f(A_h) = 0. \tag{3.10}$$

Numerical integration starts by solving q', λ', f'', τ'' from the four first ones in terms of lower derivatives; the fifth equation, the equation for λ, will be used as a check and constraint. For brevity we introduce two square root factors:

$$R_1 = \sqrt{1 + \frac{f\kappa}{q^2}\tau'^2}, \tag{3.11}$$

and

$$R_2 = \sqrt{12 + \frac{3f'}{f} - \frac{q^2}{f}\left(V_g - \frac{V_f}{R_1}\right)}. \tag{3.12}$$

The equations to be solved numerically then are

$$q' = q\left[4 + \frac{f'}{f} - \frac{q^2}{6f}\left(2V_g - V_fR_1 - \frac{V_f}{R_1}\right)\right], \tag{3.13}$$

$$\lambda' = -\frac{\sqrt{3}}{2}\lambda R_2, \tag{3.14}$$

$$f'' = f'\left[\frac{f'}{f} - \frac{q^2}{6f}\left(2V_g - V_fR_1 - \frac{V_f}{R_1}\right)\right] = f'\left(\frac{q'}{q} - 4\right), \tag{3.15}$$

$$\tau'' = -\frac{q^2}{6f}\left(2V_g - V_fR_1 - \frac{V_f}{R_1}\right)\tau' - \frac{f\kappa}{q^2}\left(4 + \frac{f'}{2f}\right)\tau'^3 \tag{3.16}$$
$$+ \frac{\sqrt{3}}{2}\left(\tau' + \frac{f\kappa}{2q^2}\tau'^3\right)\frac{\lambda\partial_\lambda\kappa}{\kappa}R_2 + \frac{\sqrt{3}}{2}\left(\tau' + \frac{f\kappa}{q^2}\tau'^3\right)\frac{\lambda\partial_\lambda V_f}{V_f}R_2 + \left(\frac{q^2}{f\kappa} + \tau'^2\right)\frac{\partial_\tau V_f}{V_f}.$$

In the λ equation the minus branch has to be chosen as $\lambda(A)$ is a monotonically decreasing function of A. The derivatives are with respect to A. The equations are autonomous in the sense that there is no explicit A dependence. Numerical integration then proceeds as follows:

1. Let us fix the horizon at $A = A_h = -\epsilon$, where ϵ is a sufficiently small number, e.g., $\epsilon = 10^{-6}$. the values of the functions at $A = 0$, which is taken as the initial value of numerical integration, are computed by using the expansions (B.19)–(B.22) in appendix B. These numbers can now be obtained by inserting the values of λ_h, τ_h, f_h'. Among these the horizon values of the scalars, λ_h, τ_h, remain as parameters, f_h' can be given an arbitrary positive value, $+1$, say. One then finds a solution $q_1(A), f_1(A), \lambda_1(A), \tau_1(A)$ valid from $A = 0$ to some large upper limit A_+ by using NDSolve of Mathematica. The spatial coordinate $r(A)$ can then, if needed, be computed by similarly integrating the differential equation

$$r'(A) = e^{-A}q(A) \tag{3.17}$$

with the initial condition $r(A = \infty) = 0$.

2. The so obtained first-level solution $f_1(A)$ is scaled to one in the UV $(A \to \infty)$ by writing $f_2(A) = f_1(A)/f_1(A_+)$. Simultaneously $q_2(A) = q_1(A)/\sqrt{f_1(A_+)}$, which is needed since eq. (3.4) demands that q^2/f be invariant. Finally, $\lambda_2 = \lambda_1, \tau_2 = \tau_1$.

3. The final scaling is performed to guarantee that all solutions use the same unit of energy or, equivalently, have the same integration constant in the integral of the definition (2.8) of the beta function. This implies

$$A - \hat{A}_0 = \ln(b) - \hat{A}_0 = \frac{1}{b_0\lambda(A)} + \frac{b_1}{b_2^2}\ln(b_0\lambda(A)) + \left(\frac{b_2}{b_0^2} - \frac{b_1^2}{b_0^3}\right)\lambda(A) + \mathcal{O}(\lambda^2), \tag{3.18}$$

where $\hat{A}_0$ is the integration constant. By inserting the UV expansions of A and λ from appendix A, we identify $\hat{A}_0 = \ln(\mathcal{L}_{\mathrm{UV}}\Lambda)$. We wish to scale Λ to one[12], and therefore define

$$A_0 = \hat{A}_0 - \ln\mathcal{L}_{\mathrm{UV}} = \ln\Lambda, \tag{3.19}$$

and shift solutions by A_0. In practice, one implements this by determining, for a given numerical solution (the $\mathcal{O}(\lambda_2)$ term is optional),

$$A_0 = \lim_{A \to \infty}\left[A - \ln\mathcal{L}_{\mathrm{UV}} - \frac{1}{b_0\lambda_2(A)} - \frac{b_1}{b_2^2}\ln(b_0\lambda_2(A)) - \left(\frac{b_2}{b_0^2} - \frac{b_1^2}{b_0^3}\right)\lambda_2(A)\right] \tag{3.20}$$

and then performing the scaling

$$\lambda_3(A) = \lambda_2(A + A_0) \tag{3.21}$$

---

[12]After this, all quantities are expressed in units of Λ; omitting the factor $\mathcal{L}_{\mathrm{UV}}$ would give a unit of energy depending on x_f

etc. for all the functions at level 2. The set $q_3(A)$, $f_3(A)$, $\lambda_3(A)$, $\tau_3(A)$, parametrised by the values of λ_h, τ_h, is the final numerical solution. Note that the horizon has now been shifted to

$$A_h = -A_0 - \epsilon \approx -A_0; \tag{3.22}$$

at level 2 it was defined by $f_2(-\epsilon) = 0$.

3.2 Physical quantities

The set of functions $q(A)$, $f(A)$, $\lambda(A)$, $\tau(A)$ (leaving out the index 3) can now be converted to various physical quantities:

The temperature is

$$T = -\frac{1}{4\pi} f'(r_h) = -\frac{e^A}{4\pi q(A)} f'(A_h)|_{A_0 = A_h} = \frac{e^{-A_0}}{-4\pi q(-A_0)} f'(-A_0), \tag{3.23}$$

and the value of b at the horizon is

$$b_h = e^{-A_0}. \tag{3.24}$$

The quark mass m_q is defined by the UV expansion of the tachyon:

$$\tau(r) = \mathcal{L}_{\mathrm{UV}} m_q (-\ln \Lambda r)^{-\frac{9}{22-4x_f}} r \tag{3.25}$$

so that, using the relation (3.18),

$$m_q = \lim_{A \to \infty} \mathcal{L}_{\mathrm{UV}}^{-1} \tau(A) \exp\left[\frac{1}{b_0 \lambda(A)} + \left(\frac{b_1}{b_0^2} - \frac{9}{22 - 4x_f}\right) \ln(b_0 \lambda(A))\right]. \tag{3.26}$$

In practice, the extrapolation to $A = \infty$ can be carried out by measuring $\tilde{m}_q(A)$, as defined by the right hand side of eq. (3.26), at two large values of A and then linearly extrapolating to $\lambda = 0$:

$$m_q = \frac{\tilde{m}_q(A_1)\lambda(A_2) - \tilde{m}_q(A_2)\lambda(A_1)}{\lambda(A_2) - \lambda(A_1)}. \tag{3.27}$$

Linear extrapolation is chosen, because the leading neglected terms in the expansion of eq. (3.26) are (up to logarithmic corrections) linear in λ.

3.3 Fixing quark mass

The above is for fixed λ_h, τ_h. The really demanding task is to find the field configurations at fixed m_q. For this one needs the curves $\tau_h(\lambda_h, m_q)$. The quark mass is determined by the UV behavior of the tachyon: $\tau(r)/\mathcal{L}_{\mathrm{UV}} \simeq m_q(-\ln r)^{-\gamma_0/b_0} r$. To fix m_q at fixed λ_h we have to solve the equations of motion at various τ_h and find that value of τ_h which leads to the desired UV behavior of $\tau(r)$.
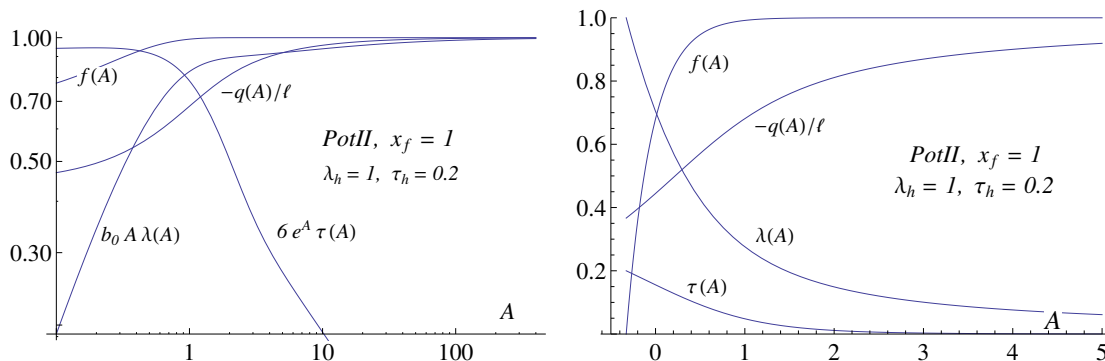
Figure 4. Explicit bulk configurations. *Left*: UV large-A region. *Right*: near horizon region. For this configuration $T = 0.3839$, $b_h = 0.7200$, $m_q = 0.05422$.

3.3.1 Zero quark mass

In particular, we are interested in $m_q = 0$. This case splits in two parts: either $\tau(r) = 0$ identically (chiral symmetry holds) or $\tau(r)$ nonzero (chiral symmetry broken).

If $\tau = 0$, solutions with $m_q = 0$ are obtained simply by setting $\tau_h = 0$ above. The solution is then controlled by the effective potential $V_g(\lambda) - x_f V_{f0}(\lambda)$. For classes I and II, this increases monotonically from $\lambda = 0$, but since V_{f0} grows faster, the derivative decreases and becomes finally zero at some $\lambda = \lambda_*(x_f)$ (see eq. (2.40)). The extremum of the potential marks the location of the IR fixed point, which is screened by the horizon at finite temperature. Indeed, the tachyonless black holes have $0 < \lambda_h < \lambda_*$, and for λ_h very close to λ_* we obtain configurations where the dilaton is approximately constant, $\lambda \simeq \lambda_h \simeq \lambda_*$ for a long range of the coordinate before the horizon is reached in the deep IR.

For classes I$_*$ and II$_*$, the effective potential $V_g(\lambda) - x_f V_{f0}(\lambda)$ does not have an extremum for x_f below $x_* \simeq 3.27$. In this case the fixed point is absent, and the tachyonless black hole solutions are qualitatively similar to Yang-Mills ($x_f \to 0$) [30–32]. In particular λ_h can take any value.

For non-zero $\tau(r)$, the discussion of $m_q = 0$ configurations has to take into account the existence of Efimov zeroes, oscillatory behavior when approaching $r = 0$, which was discussed above in the introduction. We discuss here the standard picture which is seen in most cases for $x_f < x_c$. A rough description of more complicated cases is given in appendix C. The situation is summarised in figure 5. For large $\tau_h > 0$, $\tau(r)$ decreases monotonically from τ_h towards $r = 0$ and ends with positive m_q. We evaluate m_q using (3.27) with two large values of A (corresponding to a small UV cutoff ϵ in the r-coordinate). When τ_h is decreased, ultimately an (approximate) $m_q = 0$ configuration ($\tau_0(r, m_q = 0)$ in figure 5) with monotonically decreasing $\tau(r)$ is obtained.

This defines the curve $\tau_{h0}(\lambda_h)$ in figure 6. One finds that these solutions are possible only if λ_h is larger than a fixed positive value, which we call λ_{end}. Decreasing τ_h further, $\tau(r)$ first develops a zero so that $m_q < 0$. Continuing even further we find a second location where $m_q = 0$ vanishes. This is a configuration with one tachyon node ($\tau_1(r, m_q = 0)$ in figure 5). The pattern continues with an ever increasing number of nodes, until one ends up
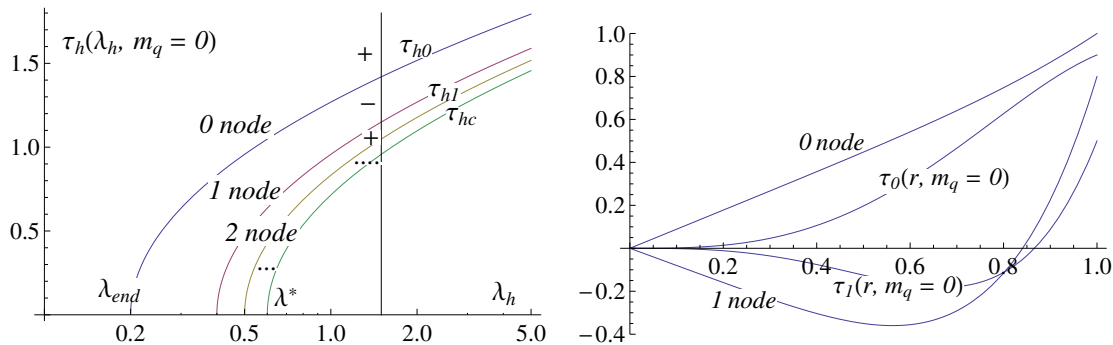
Figure 5. *Left*: schematic presentation of the curves $\tau_h(\lambda_h, m_q = 0)$, i.e., those values of the horizon value τ_h of the tachyon which lead to configurations with $m_q = 0$, at that particular λ_h. Choosing τ_h on the curve τ_{hi} leads to a $\tau(r)$ without a linear term and with i zeros at some r. The zero mass solutions with vanishing tachyon live on the line $0 < \lambda_h < \lambda_*$. The plus and minus signs indicate the sign of the quark mass in each region limited by the curves $\tau_{h0}, \tau_{h1}, \ldots$ *Right*: schematic presentation of the r dependence of the bulk tachyon for low node numbers. Tachyon solutions for top to bottom are: a generic solution with $m_q > 0$ and no nodes ("0 node"), the standard solution with zero quark mass (τ_0), the solution with zero quark mass and one node (τ_1), and a generic solution with $m_q < 0$ and one node ("1 node"). See the text for a more detailed explanation.

with the curve $\tau_{hc}(\lambda_h)$, below which a solution with the standard UV boundary does not exist. Numerically, the curves $\tau_{h0}(\lambda_h)$ and $\tau_{h1}(\lambda_h)$ can be separated, but already $\tau_{h2}(\lambda_h)$ would require so much effort that we have not embarked on computing it. As we approach the conformal window, the curves $\tau_{h0}, \tau_{h1}, \ldots$ get closer and closer to τ_{hc} and finally vanish for $x_f \geq x_c$.

We expect that increasing the number of nodes increases the free energy so that to study equilibrium states it is enough to compute $\tau_{h0}(\lambda_h, m_q = 0)$. This was checked at zero temperature in [26] numerically for potentials I, and analytically in the limit $x_f \to x_c$ as well as in the limit of large number of tachyon nodes.

3.3.2 Nonzero quark mass

For nonzero quark mass the special solution with identically vanishing tachyon profile is missing. However, there are solutions of various types for $\tau_h > 0$, as suggested by figure 5. We shall here restrict to the "standard" solutions which have monotonic tachyon, i.e., the region above τ_{h0} in figure 5 (left). Below this curve there can be Efimov type solutions where the tachyon has nodes. As for $m_q = 0$, we expect that these solutions have higher free energies than the standard one. In the region of standard solutions, the dependence of quark mass is smooth (see figure 6). We have found numerically that for fixed λ_h the correspondence between m_q and τ_h is one-to-one. Therefore m_q can be kept fixed by following a set of well-defined curves on the (λ_h, τ_h)-plane, some of which are sketched in figure 6.

It is also interesting to notice how the $m_q = 0$ solution is obtained from the ones having finite quark masses as $m_q \to 0$. What happens for nonzero quark mass is shown in figure 6 for a concrete computation. If $0 < \lambda_h < \lambda_{\text{end}}$ (and λ_h fixed), the curve $\tau_h(\lambda_h, m_q)$
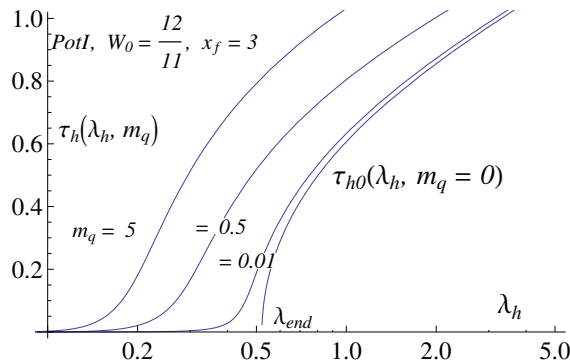
Figure 6. The curves $\tau_h(\lambda_h, m_q)$ for values of m_q marked in the figure, computed for Potential I with $W_0 = 12/11$. Here $\lambda_{\text{end}} = 0.5221$ and $\lambda_* = 0.6467$.

approaches zero as $m_q \to 0$, indicating that $\tau(r)$ approaches the chiral symmetry conserving solution ($\tau(r) \equiv 0$) uniformly. If $\lambda_h > \lambda_{\text{end}}$, $\tau_h(\lambda_h, m_q)$ approaches $\tau_{h0}(\lambda_h)$ instead, which implies that $\tau(r)$ converges to the standard chiral symmetry breaking solution $\tau_0(r)$.

3.4 Thermodynamics

We now want to compute minus free energy density or pressure $p(T, m_q; x_f)$ of the gravity dual, assuming that all the quarks have the same mass m_q. In particular, we are interested in $m_q = 0$. The chemical potential is zero, there is an equal number of quarks and antiquarks. The equilibrium phase has the largest pressure.

The basic strategy is to compute the temperature and entropy density from the formulas

$$T = -\frac{1}{4\pi} f'(r_h), \quad s = \frac{1}{4G_5} b^3(r_h), \tag{3.28}$$

where f and b are obtained by solving Einstein's equations. The pressure is then obtained by integrating $s(T) = p'(T)$. The key technical issues are keeping track of the quark mass and specifying the integration constant in the pressure integral.

The general structure of temperature (for a case containing a fixed point) is shown in figure 7, to be consulted in association with figures 5 and 6. For $m_q = 0$ two branches separate. Firstly, for $0 < \lambda_h < \lambda_*$ there is the temperature computed for chirally symmetric vanishing tachyon solutions. We shall use the notation $T_u(\lambda_h) \equiv T(\lambda_h, \tau_h = 0)$ for this temperature below.

The chiral symmetry breaking solution exists for $\lambda_{\text{end}} < \lambda_h < \infty$ and as $\lambda_h \to \lambda_{\text{end}}$, the corresponding temperature curve ends precisely on the curve which has identically vanishing tachyon. The temperature curve is computed by using the zero node zero mass curve $\tau_{h0}(\lambda_h)$ in figure 5. We shall use the notation $T_b(\lambda_h) \equiv T(\lambda_h, \tau_{h0}(\lambda_h, m_q = 0))$ for this temperature. If we computed the temperature for the one node solution $\tau_{h1}(\lambda_h)$, we would get a curve which lies significantly below the zero node curve in figure 7 and again ends on the zero tachyon curve. These solutions will have a higher free energy and we can thus neglect them.
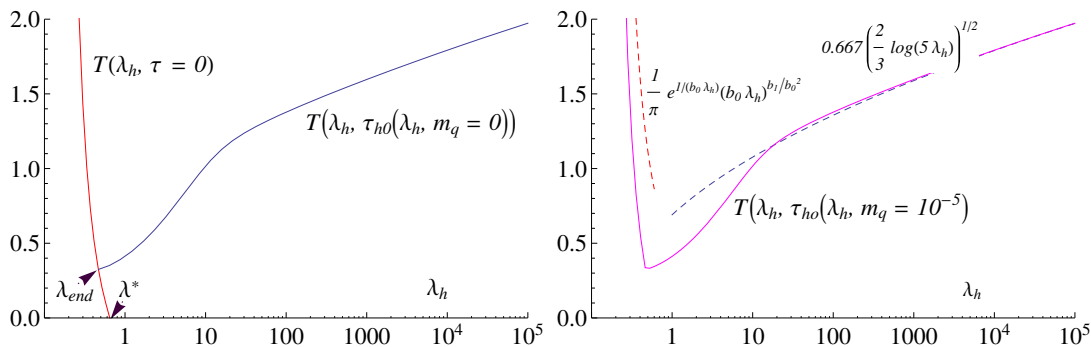
Figure 7. The temperature as a function of λ_h for solutions for Pot II at $x_f = 3$ and $W_0 = 12/11$, both for zero (*Left*) and very small mass (*Right*). The asymptotic limits (3.29) and (3.30) are also shown for $m_q = 10^{-5}$, in the range of the figure the UV limit is not yet accurate. The maximum value λ^* of λ for the $\tau = 0$ curve is defined in (2.40). See also figure 2.

Whenever the quark mass is nonzero, the tachyon cannot be vanishing and that branch disappears. However, as seen from figures 6 and 7, the small-mass curve very closely approximates the zero tachyon curve, also at small λ_h.

Analytic approximations are often useful. In the UV $f(r) \to 1 - r^4/r_h^4$ so that

$$\pi T(\lambda_h) = \frac{1}{r_h} = e^{1/(b_0\lambda_h)}(b_0\lambda_h)^{b_1/b_0^2} = \frac{b(\lambda_h)}{\mathcal{L}_{\rm UV}}. \tag{3.29}$$

Similarly, in the IR (see (B.10) in appendix B),

$$T(\lambda_h) \sim \left(\frac{2}{3} \ln \lambda_h\right)^{1/2}, \quad b(\lambda_h) \sim \frac{1}{\lambda_h^{2/3}}\left(\frac{2}{3} \ln \lambda_h\right)^{1/4}. \tag{3.30}$$

For a numerical check, see figure 7. The interesting physics takes place in the region connecting these two limits.

The function $b(\lambda_h)$ decreases monotonically while the function $T(\lambda_h)$ decreases in the UV but starts increasing in the IR. The physics of the UV increase is obvious, this is the weak coupling limit which naturally corresponds to large T of a thermal fluid. The (extremely slow) increase in the IR is a quantitative fact but does not correspond to a stable phase. This is simplest seen by computing the sound velocity

$$c_s^2 = \frac{dp}{d\epsilon} = \frac{s}{Ts'(T)} = \frac{b(\lambda_h)}{3T(-b'(\lambda_h))}\left(-\frac{dT}{d\lambda_h}\right). \tag{3.31}$$

A stable phase has $c_s^2 > 0$ (equivalently, has a positive specific heat) and this requires $T'(\lambda_h) < 0$. Thus only the UV decreasing part can correspond to a stable phase, the IR part is the unstable small black hole region, small since $s \sim b^3(\lambda_h) \to 0$ there. It is, nevertheless, crucially important for the phase structure.

To compute the pressure, we have to integrate the entropy density (3.28) over T. Taking λ_h as a variable, we have integrals over the two branches in figure 7:

$$p_b(T) = \frac{1}{4G_5} \int_{\lambda_h(T)}^{\infty} d\lambda_h(-T_b'(\lambda_h)) \, b_b^3(\lambda_h) + p_b(\infty), \qquad (3.32)$$

$$p_u(T) = \frac{1}{4G_5} \int_{\lambda_h(T)}^{\lambda_*} d\lambda_h(-T_u'(\lambda_h)) \, b_u^3(\lambda_h) + p_u(\lambda_*), \qquad (3.33)$$

where b, u refer to the chiral symmetry broken ($\tau_h = \tau_{h0}(\lambda_h, m_q = 0)$) and chirally symmetric (or unbroken, $\tau = 0$) phases. The continuity of pressure at $T_{\text{end}} = T(\lambda_{\text{end}})$ leads to a rather remarkable consistency check of the entire scheme: it demands

$$\frac{1}{4G_5} \int_{\lambda_{\text{end}}}^{\lambda_*} d\lambda_h(-T_u'(\lambda_h)) \, b_u^3(\lambda_h) - \frac{1}{4G_5} \int_{\lambda_{\text{end}}}^{\infty} d\lambda_h(-T_b'(\lambda_h)) \, b_b^3(\lambda_h) = p_b(\infty) - p_u(\lambda_*). \quad (3.34)$$

However, the difference on the r.h.s. is nothing but the difference between the free energies of the broken and symmetric phases at $T = 0$:

$$p_b(\infty) - p_u(\lambda_*) = -F_b(T = 0) + F_u(T = 0). \qquad (3.35)$$

This difference was computed in [26] from the $T = 0$ solutions, with no black hole. Here they are computed in (3.34) from the black hole solutions and we have checked numerically that the results agree within the numerical precision.

The computation of the free energy now proceeds as follows, first for the simple structure of $T(\lambda_h)$ in figure 7:

- Start by integrating (3.32) from some large value of λ_h down to λ_{end}, choosing $p_b(\infty) = 0$. Since $T'(\lambda_h) > 0$ in figure 7, this leads to a negative pressure. This is not the stable phase, the physical stable phase is not described by this metric. The stable phase with the largest pressure is the thermal gas phase with $p = 0$.

- At λ_{end} move to the chirally symmetric $\tau = 0$ branch and fix the constant $p_u(\lambda_*)$ by demanding continuity of pressure. Since now $T'(\lambda_h) < 0$, p starts increasing. At first p is still negative and the stable phase is the thermal gas phase with $p = 0$.

- At some $\lambda_h \equiv \lambda_c$ pressure passes through 0. This defines a transition temperature T_h since from now on the black hole metric has the largest pressure. Since $\tau = 0$ this black hole phase is chirally symmetric.

- The latent heat of the transition is

$$\frac{L}{T_h^4} = \frac{s(T_h)}{T_h^3} = \frac{1}{4G_5} \left(\frac{b(\lambda_h)}{T_h} \right)^3 < N_c^2 \frac{4\pi^2}{45} \left(1 + \frac{7}{4} x_f \right), \qquad (3.36)$$

  where the maximum value is obtained taking normalisation from (3.39) and using the UV approximation (A.19). Counting degrees of freedom one has N_f^2 Goldstone bosons in the low T phase (for which we do not have a T dependent gravity dual) and $2N_c^2 + \frac{7}{2} N_c N_f$ degrees of freedom in the high T phase. These are equal at $x_f = 4$ and if latent heat is naively assumed to be proportional to the jump in the number of degrees of freedom, one might rather expect L to decrease when x_f increases.

– 27 –

- Asymptotically, for large T, $\lambda_h \to 0$ we have $\pi T = 1/r_h = b(\lambda_h)/\mathcal{L}_{\text{UV}}$ so that

$$4G_5 p = (\pi \mathcal{L}_{\text{UV}})^3 \int_{\lambda_h}^{\infty} dx (-T'(x)) T^3(x) = \frac{1}{4} (\pi \mathcal{L}_{\text{UV}})^3 T^4. \qquad (3.37)$$

If one for large T assumes that the system becomes a gas of non-interacting bosons and fermions one should have

$$\frac{p}{T^4} = \left(1 + \frac{7}{4} x_f\right) \frac{\pi^2}{45} N_c^2. \qquad (3.38)$$

This is obtained from (3.33) if

$$\frac{1}{4G_5} = \frac{4}{45\pi} \frac{1 + \frac{7}{4} x_f}{\mathcal{L}_{\text{UV}}^3} N_c^2, \qquad (3.39)$$

which can be used to normalise the pressure.

- The above was for the simple $T(\lambda_h)$ in figure 7. Depending on the potentials, more complex structures can appear, as analysed in the following section.

- To present results for p/T^4 we choose to normalise it so that it approaches at large T the ideal gas Stefan-Boltzmann pressure according to (3.38). However, we have no dynamical argument for fixing the x_f dependence of $\mathcal{L}_{\text{UV}}$ in (3.39). We shall present the phase diagrams for two choices, for the automatically SB-normalised case (see eq. (3.39))

$$\mathcal{L}_{\text{UV}} = \left(1 + \frac{7}{4} x_f\right)^{1/3}, \quad W_0 = \frac{12}{x_f} \left[1 - \frac{1}{(1 + \frac{7}{4} x_f)^{2/3}}\right], \qquad (3.40)$$

and for the W_0 fixed case

$$\mathcal{L}_{\text{UV}} = \frac{1}{\sqrt{1 - \frac{1}{12} W_0 x_f}}, \quad W_0 = 0, \frac{12}{11}, \frac{24}{11} \qquad (3.41)$$

In the former case one simply has
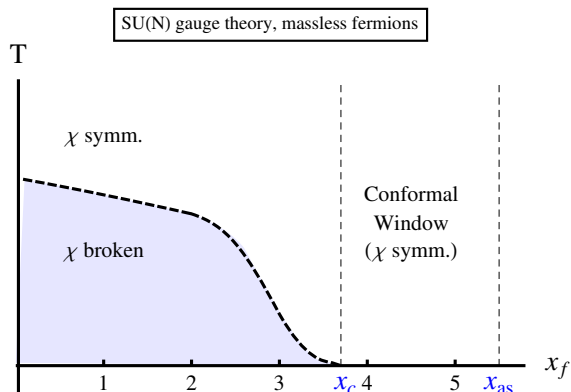
$$\frac{1}{4G_5} = \frac{4}{45\pi} N_c^2 \qquad (3.42)$$

and in the latter case[13]

$$\frac{1}{4G_5} = \frac{4}{45\pi} \frac{1 + \frac{7}{4} x_f}{(1 - \frac{1}{12} x_f W_0)^{2/3}} N_c^2; \qquad (3.43)$$
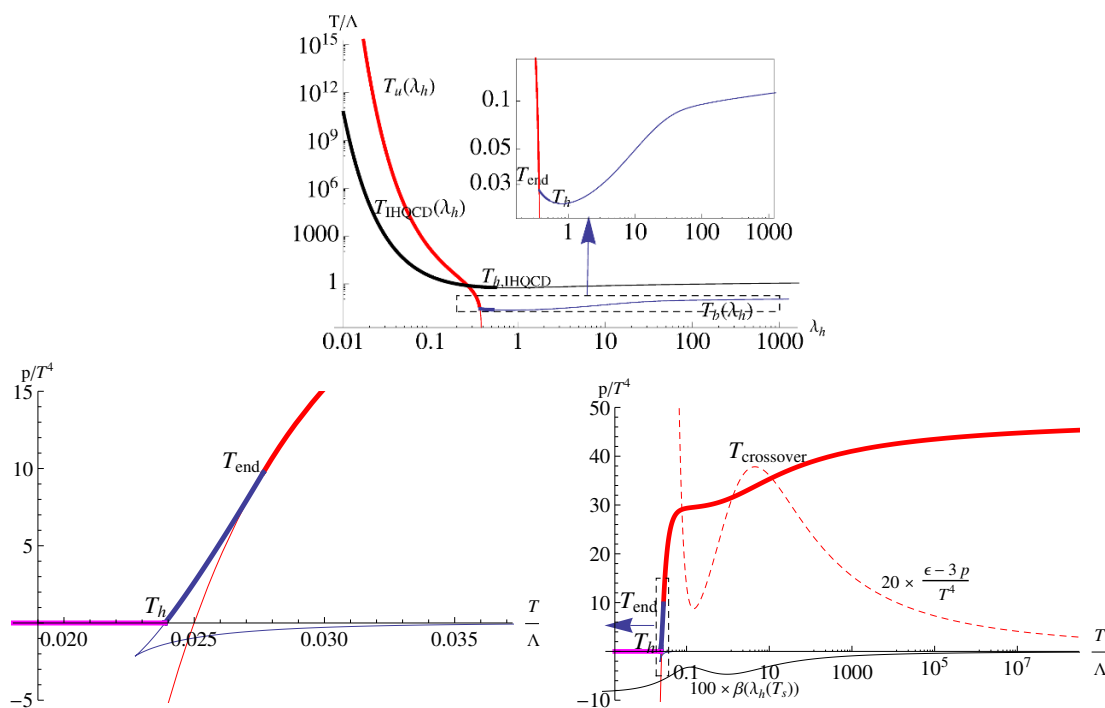
the factor N_c^2 is furthermore often implied, i.e., results for $p/(N_c^2 T^4)$ are given.

---

[13]Notice that in this case the glue part of the V-QCD action will also depend on x_f through the normalization factor $1/4G_5$.

Figure 8. Qualitative behavior of the transition temperature between the low and high T phases of V-QCD matter.

Figure 9. Examples of the T_{end}, T_h and $T_{\text{crossover}}$ transitions in potential II with Stefan-Boltzmann -normalization of $\mathcal{L}_{\text{UV}}$ and with $x_f = 3$ (see also figure 13). *Upper*: The temperature $T(\lambda_h)$. The curving of $T_u(\lambda_h)$ at $\lambda_h \sim 0.2$, $T \sim 2$ is related to the crossover. The inset shows the minimum of $T_b(\lambda_h)$, which causes p_b to be positive between T_h and T_{end}. For comparison, we also plot $T(\lambda_h)$ for IHQCD with $x_f = 0$. *Lower left*: p/T^4 in a close-up around the region of the T_h and T_{end} -transitions. *Lower right*: an overview of the pressure in the same case, also showing the interaction measure, the peak of which determines the position of $T_{\text{crossover}}$. The black curve shows the vacuum beta function, scaled to fit, as a function of temperature in the symmetric phase, so that $\beta(T) = \beta(\lambda_u(T))$, where $\lambda_u(T)$ is the inverse function of $T_u(\lambda_h)$. The walking maximum of the beta function clearly coincides with the plateau related to $T_{\text{crossover}}$, confirming that the $p/T^4 \sim$ constant phase below $T_{\text{crossover}}$ is indeed the quasi-conformal phase related to walking dynamics.
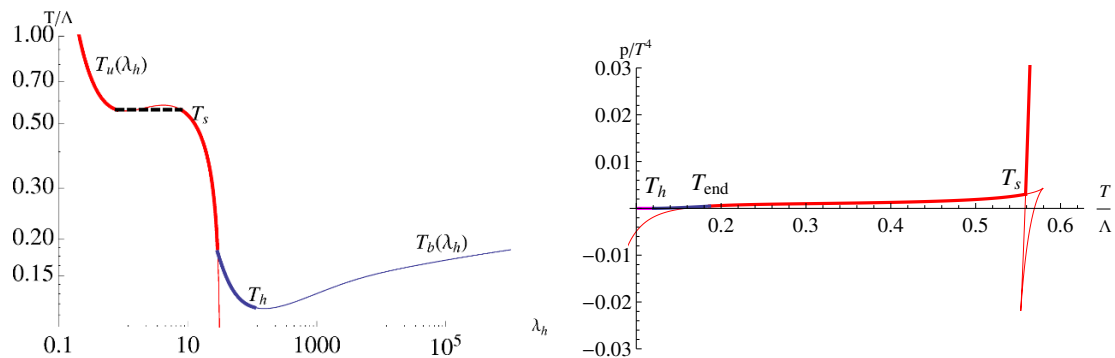
Figure 10. An example of the T_s transition in potential I with $W_0 = 24/11$ and with $x_f = 0.3$ *Left*: the local maximum and minimum which generate the 1st order T_s-transition. *Right*: $p(T)/T^4$ in the region around which the 1st order T_s transition takes place, extending to smaller T in order to show the relation to the T_h and $T_{\rm end}$ transitions.

4 Results for the phase structure

4.1 Phase transitions

Let us first review what one qualitatively expects for the phase structure of V-QCD when the number of (massless) fermions is changed [71]. This is shown in figure 8, where the transition temperature between a low T and a high T phase is plotted as a function of x_f.

A few reminders are in order. In the absence of quarks, YM has a Z_{N_c} center symmetry that is central in the definition of the confined and deconfined phases. The relevant order parameter is the Polyakov loop that transforms nontrivially under Z_{N_c}. If its expectation value is zero, we are in the confined phase, while the expectation value becomes non-zero in the deconfined phase.

This expectation value is simple to calculate holographically, [72]. It corresponds to a string world-sheet along the time circle, and hanging down straight in the holographic (radial) direction. The important difference is where it ends. At zero temperature, this worldsheet extends to $r \to \infty$ and is the world-sheet of a free quark. Standard renormalization subtracts its contribution completely and therefore the Polyakov loop vev is zero (to leading order in $1/N_c$) in the zero temperature phase.

In a regular black-hole phase, the worldsheet terminates at the horizon and after subtraction the Polyakov loop expectation value is non-zero. This is in agreement with the identification of black-hole phases generically as deconfined phases.

In the presence of massless quarks, the center symmetry is not a symmetry any more, and the Polyakov loop is not an order parameter. However at large N_c, there is alternative order parameter for a deconfined phase, namely the N_c dependence of the free energy, F. In the confined phases $F \sim \mathcal{O}(1)$ while in deconfined phases, $F \sim \mathcal{O}(N_c^2)$. Again, with this criterion, the vacuum solutions (without horizons) are "confining" ($F \sim \mathcal{O}(1)$) while any black hole solution with regular horizon is "deconfined" ($F \sim \mathcal{O}(N_c^2)$). It is therefore natural to use this criterion in our analysis in order to define deconfined phases.

The true symmetry in the case of massless quarks is chiral symmetry. This always has an order parameter, the chiral condensate, that distinguishes chirally symmetric from chirally broken phases.

Given the remarks above, we summarize what we would expect.

- For $x_f = 0$ one has the Yang-Mills 1st order phase transition between a confined and deconfined phase. In the high T deconfined phase, the Z_{N_c} symmetry is broken.

- For a somewhat higher x_f one expects that there still is a 1st order transition. However, now this transition will involve chiral symmetry breaking/restoration.

- For x_f approaching x_c one expects the transition temperature to decrease rapidly as follows from Miransky scaling.

- For x_f in the conformal window, $x_c < x_f < 11/2$, both the low and high T phases are conformal ones, which can be separated by a crossover. The only transition happens at $T = 0^+$ like in the AdS black hole in Poincaré coordinates.

The models we consider contain the full fermion backreaction and therefore predict a somewhat more detailed phase structure. New phase transitions of different orders can take place, lines can split in two, etc. The behavior in the conformal window ($x_c < x_f < 11/2$) is nonetheless always simple: there are no transitions, but a crossover between the low and high temperature conformal phases. Therefore we concentrate first on the phase structure in the region below the conformal transition ($x_f < x_c$).

While the details of the phase structure depend on the choice of potential, the various phase transitions encountered appear in certain systematic ways. We will define a consistent notation, and describe the classes of transitions, assuming the system is heated up and we go from low temperatures to high temperatures.

To motivate the notation, we first list the various transitions and the corresponding temperatures.

- T_h is the analogue of the QCD hadronisation transition if it is the chiral restoration transition (chirally symmetric → chirally broken).

- T_{end} is the end point of the curve $T_b(\lambda_h) = T(\lambda_h, \tau_{h0}(\lambda_h, m_q = 0))$, which contains the black holes with tachyon hair. For values of λ_h smaller than at this endpoint, the black-holes have no tachyon hair.

- $T_{\text{crossover}}$ marks the position of a crossover. This crossover is defined by the position of the peak in the equation-of-state $((\epsilon - 3p)/T^4)$ as a function of temperature.

- T_s takes place at small x_f within the chirally symmetric phase when one can jump from one decreasing branch of $T_u(\lambda_h)$ (no tachyon hair) to another.

- Finally T_{12} involves the splitting of one 1st order line to two.

With this notation we may now describe in detail the various types of transitions and crossovers we have found, and show examples of each case. In the figures we denote the stable phases with thick lines and meta- and unstable phases with thin lines.

- The 1st order hadronisation transition at T_h, happens either between the chirally broken $\rightarrow$ a chirally symmetric phase (see figure 7) or from a chirally broken $\rightarrow$ a chirally broken phases (see figure 9).[14] As described above, our normalization for pressure is such that the pressure of the ($T = 0$) hadron gas phase is zero. In the holographic setup, this transition is between that of the black hole phases, whose pressure remains positive down to the lowest temperature, and the hadron gas phase. The transition takes place at the temperature T_h where the pressure of the BH phase reaches zero. Whether this phase is chirally symmetric or non-symmetric depends on the potential choices and x_f. For an example, see figure 13.

- The 2nd order chirally broken $\rightarrow$ chirally symmetric transition at $T_{\mathrm{end}} = T(\lambda_{\mathrm{end}}, 0) = T(\lambda_{\mathrm{end}}, \tau_{h0}(\lambda_{\mathrm{end}}, m_q = 0))$, see figures 7 or 9. Since the chiral symmetry breaking solution starts to exist only above some λ_{end}, the system makes at that point a transition to the chirally symmetric phase. However, this transition may be absent in the thermodynamic limit: if $p_b(\lambda_h)$ is everywhere negative, the transition is between two thermodynamically metastable phases, and the relevant saddle point is never dominant. We denote the temperature of the transition by T_{end}. Since this transition takes place at one single value $\lambda_h = \lambda_{\mathrm{end}}$, both pressure and entropy density are continuous ($b(\lambda_h)$ does not jump). Therefore, only $p''(T)$ or c_s^2 are discontinuous, and the transition is of second order.

- The high-T chirally symmetric $\rightarrow$ chirally symmetric crossover at $T_{\mathrm{crossover}}$, see figure 9. This is a crossover which is expected on general grounds when x_f is near but below x_c. It reflects the change of the dynamics from the walking region, where the QCD coupling constant evolves slowly, to the region in the deep UV where it runs. In this sense, above the crossover it is the nontrivial fixed point theory that controls the thermodynamics, while below the crossover it is the YM-like theory that controls the dynamics.

  The thermodynamics behaves as follows: At first p/T^4 stabilizes to some intermediate value, before eventually increasing very slowly toward the Stefan-Boltzmann limit. For the potentials studied here, this creates a clear, although very broad, peak in the interaction measure, and the position of that peak can be used to define the temperature $T_{\mathrm{crossover}}$ at which there is a crossover. The peak of the interaction measure is also observed at low values of x_f. In this region, however, $T_{\mathrm{crossover}}$ is typically relatively close to T_h. Note also that for SU(N_c) YM theory, $N_f = 0$ the interaction measure starts decreasing immediately at T_h [73], $T_{\mathrm{crossover}} \simeq T_h$.

- The 1st order high-T chirally symmetric $\rightarrow$ chirally symmetric transition at T_s, see figure 10: With some choices of potential, at low x_f, $T_u(\lambda_h)$ in the chirally symmetric (unbroken) part of the solution develops a local maximum and minimum. There are then two values of λ_h between which both the pressure and the temperature of the

---

[14]There is also the special case of potentials I$_*$ at low x_f where the transition analogous to T_h takes place from a chirally *symmetric* thermal gas to chirally symmetric black hole phase (see figure 19).
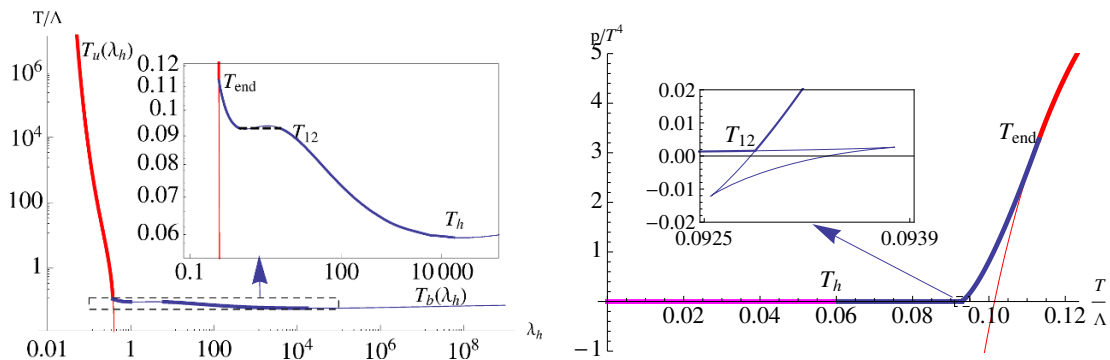
Figure 11. An example of the T_{12} transition in potential I with $W_0 = 12/11$ and with $x_f = 3.5$. *Left*: the overall structure of $T(\lambda_h)$, with an inset showing the maximum and minimum in more detail. *Right*: a close-up of $p(T)/T^4$ in the region where the T_{12} -transition happens, with an inset showing further detail.

solution match, and there is a 1st order transition between these two branches of the chirally symmetric solution. Interestingly, T_s approaches the temperature of the YM transition in IHQCD as $x_f \to 0$ (see the discussion in section 4.8).

- The 1st order chirally broken $\to$ chirally broken transition at T_{12}, see figure 11. This happens in the chirally non-symmetric phase, with potential I and $W_0 = 12/11$, $T(\lambda_h)$ which develops a local minimum and maximum at large x_f. This again induces a 1st order transition, which we denote by T_{12}. In this case the single 1st order transition at T_h splits into two 1st order transitions as x_f increases above some critical value. Above this value, the transition with higher (lower) temperature is identified as T_{12} (T_h).

4.2 Class-II potentials

Let us then discuss the details of the phase structure for the various potentials and choices of W_0 defined in section 2.2.2.

We take Class-II first since it leads systematically to a simple phase structure. We observe two possibilities: First, for x_f up to some value $x_\chi < x_c$ the 1st order deconfinement and chiral transition temperatures coincide, $T_d = T_\chi$, from this value up to x_c one has $T_\chi > T_d$ and the higher chiral transition is of 2nd order. Second, $T_d = T_\chi$ all the way up to x_c and x_χ is absent.

For this choice of potentials the tachyon diverges $\sim \sqrt{r - r_1}$ at large r. The part $V_{f0}(\lambda)$ of the fermionic potential is given by eq. (2.30) and $a(\lambda)$ and $\kappa(\lambda)$ are given in (2.38). Notice that the deconfinement temperature T_d always equals the temperature of the "standard" 1st order transition T_h in the holographic framework. The temperature of the chiral symmetry restoration T_χ can be either T_{end} or T_h depending on the order of the transitions, see examples below.

The result for the SB-normalised case is shown in figure 13. For $0 < x_f < x_\chi \simeq 2.46$ we find that $T_{\text{end}} < T_h$, but T_{end} is in the metastable branch of the solution. Thus the

– 33 –
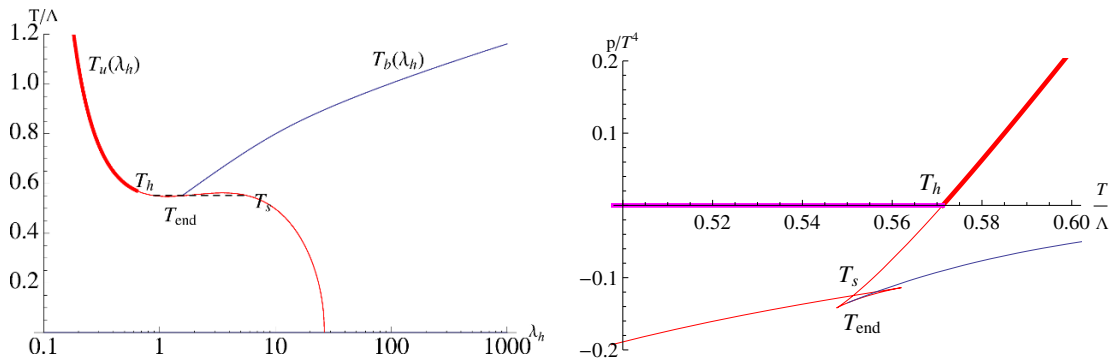
Figure 12. An example of a configuration where all but the crossover and hadronisation transitions $T_{\text{crossover}}$, T_h, are in the thermodynamically unstable region, in the initial stages of the approach to the IHQCD limit. The potential is II with $W_0 = 12/11$ and with $x_f = 0.4$ *Left*: the temperature $T(\lambda_h)$. Note that everything to the right of the T_h transition is in the unstable phase. *Right*: $p(T)/T^4$ in the region where the T_h transition and the unstable T_{end} and T_s -transitions happen.

deconfinement and chirality transitions coincide here, $T_d = T_\chi = T_h$. In other words, if one could sufficiently supercool the system below T_h in the high-T chirally symmetric phase, the symmetry breaking transition could take place at $T_{\text{end}} < T_h$. In the thermodynamic limit there is no supercooling and only T_h is seen.

Above $x_f \simeq 2.46$, the second order T_{end} moves above T_h and becomes stable, as seen in the bottom right plot of figure 13. Therefore, we first have a 1st order T_h transition from the thermal gas solution to a chirally breaking black-hole phase, and then a 2nd order transition from the chirally broken low-T phase to the chirally symmetric high-T phase. In other words, $T_\chi > T_d$ with a 2nd order chiral and 1st order deconfinement transition. For a more detailed view of the thermodynamics in this region at $x_f = 3$, the reader is guided to the left panel of figure 24 where the chiral condensate as well as the energy and the pressure are plotted as functions of T. The chirally symmetric crossover transition $T_{\text{crossover}}$ is for all x_f, the highest temperature transition.

For $x_f \to x_c$ both T_{end} and T_h are expected to approach zero as specified by Miransky scaling. Numerical results are compatible with this.

When $x_f \to 0$ one would expect that the T_h transition smoothly approaches the transition temperature of large N_c hot Yang-Mills theory. Note, however, that strictly speaking the limit of YM theory demands $N_f = 0$ and falls outside the Veneziano limit $N_f \to \infty$ of QCD. Thus it is not surprising that nontrivial metastable structures appear at $x_f \to 0$. What happens is that the curve $T = T_u(\lambda_h)$ of the chirally symmetric phase suddenly at $x_f \sim 0.2$ develops a local minimum similar to the one shown in red in figure 10. Further evolution of this minimum is shown in figure 22. Associated with this there is a first order T_s transition in the metastable branch. It is so slightly below T_h that it is not visibly separated in the bottom left plot of figure 13. As discussed in section 4.8, both T_h and T_s approach the transition temperature of YM as $x_f \to 0$. T_{end} crosses above all of the other transitions for low x_f, but it is also in the metastable branch, see figure 12 for details.
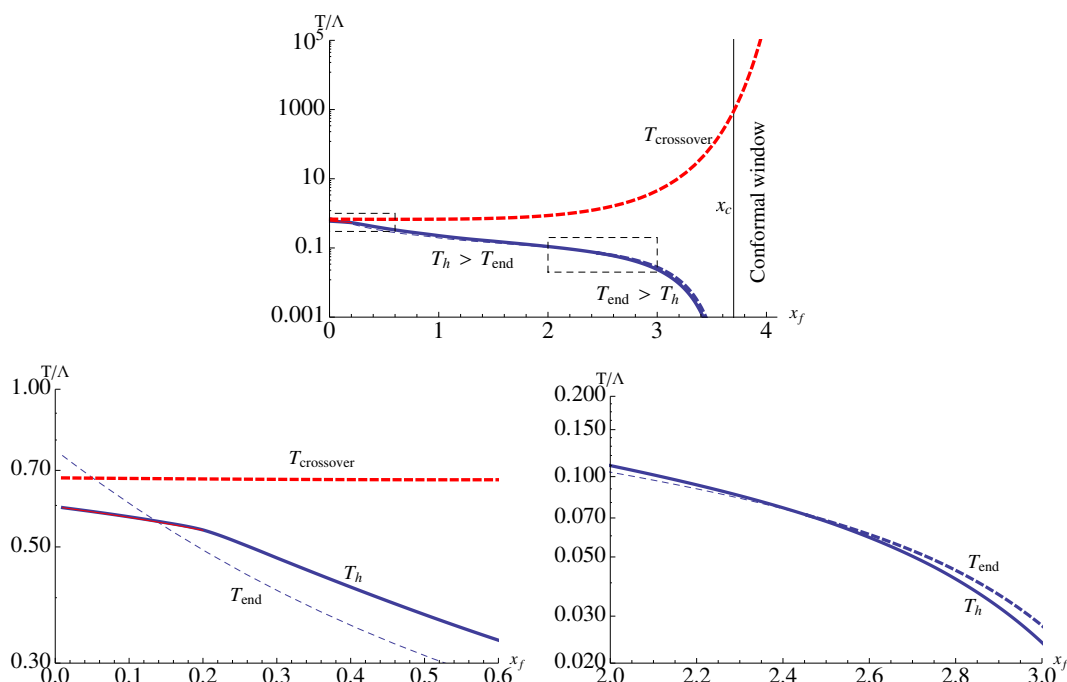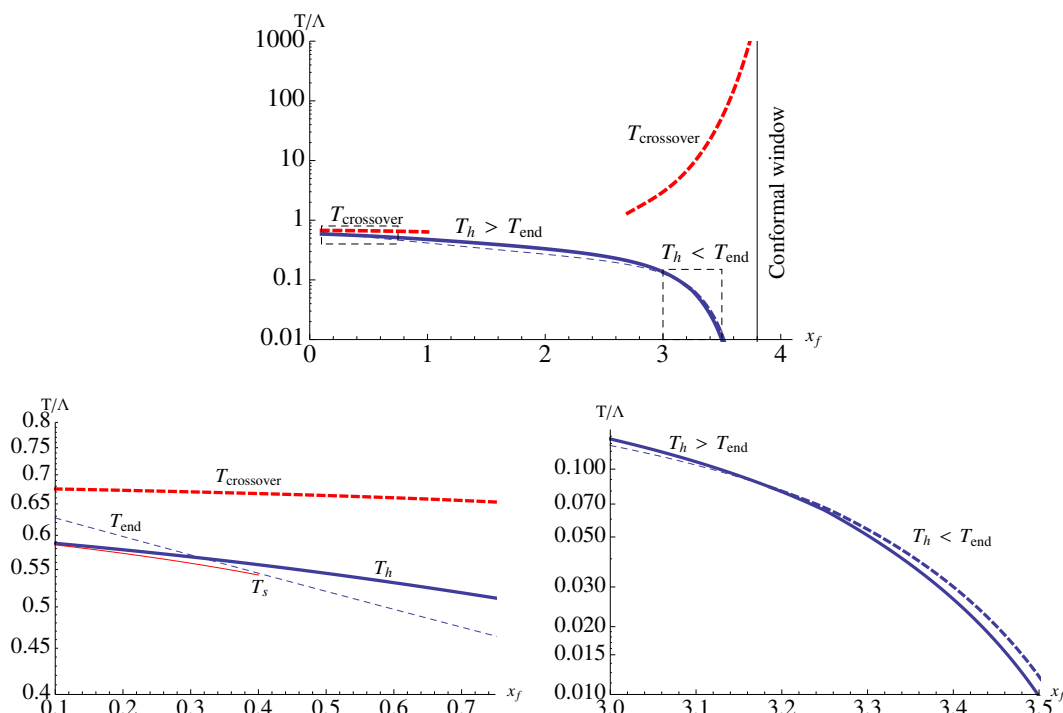
Figure 13. *Upper*: the phase diagram for potential II, W_0 Stefan-Boltzmann normalized, $x_c = 3.70$. The dashed boxes show the regions detailed in the bottom two plots. In the bottom left plot $T_s \lesssim T_h$ at $x_f \lesssim 0.2$ is not visibly separated. For discussion, see text.

The phase diagram for potential II at $W_0 = 24/11$ is shown in figure 14. The phase structure is qualitatively similar to the SB-normalized case. For $x_f < x_\chi \simeq 3.19$ the stable T_h transition is the only one in the thermodynamic limit, with $T_{\rm end} < T_h$ in the metastable branch of the solution. Thus again $T_d = T_\chi$. Above $x_f \simeq 3.19$, the second order $T_{\rm end}$ moves above T_h and becomes stable, see bottom right plot of figure 14. Thus we again have $T_\chi > T_d$ with a 2nd order chiral and 1st order deconfinement transition. The chirally symmetric crossover transition $T_{\rm crossover}$ is for all x_f the highest temperature stable transition, except between $x_f \sim 1$ to $x_f \sim 2.7$, where the interaction measure does not have a maximum and the crossover therefore does not exist.

Now T_s which appears in the metastable branch slightly below T_h in figure 10 (bottom-left) visibly separates from T_h. Again T_s and T_h approach the temperature of the YM-transition in the $x_f \to 0$ -limit, as discussed in section 4.8. $T_{\rm end}$ crosses above the T_h transition for $x_f < 0.34$, but it is also in the metastable branch, see figure 12 for details.

The phase diagram for potential II at $W_0 = 12/11$ is shown in figure 15. The main difference with respect to the previous cases is that $T_{\rm end} < T_h$ for all values of x_f, so the region with $T_\chi > T_d$ does not exist. Notice that $T_{\rm end}$ is close to T_h for $x_f \to x_c$ as seen from figure 15 (left). Because the region with small $x_c - x_f$ is numerically challenging, we do not have reliable data for $x_f \gtrsim 3.8$. However, nontrivial structure apart from the Miransky scaling, such as rapid changes in the ratios of the various temperatures, are not expected in this region (see discussion below in section 4.8). The chirally symmetric
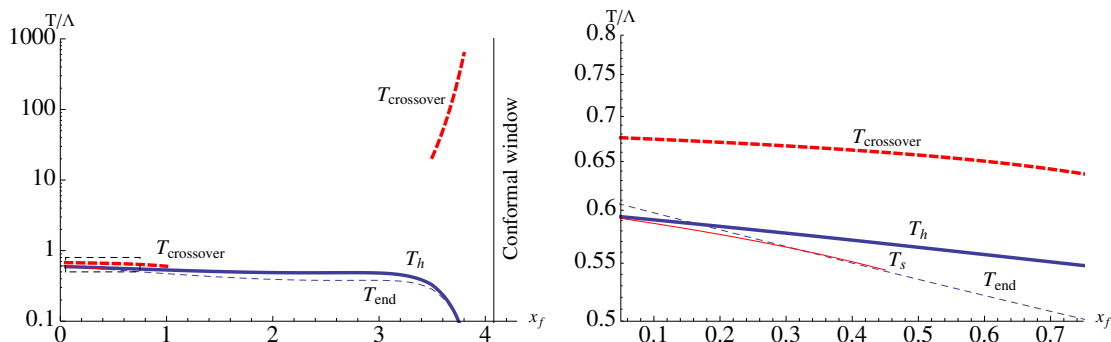
Figure 14. *Upper*: the phase diagram for potential II, $W_0 = 24/11$, $x_c = 3.80$. The dashed boxes show the regions detailed in the bottom two plots. For discussion, see text.

crossover transition $T_{\text{crossover}}$ is the highest temperature stable transition where it exists. The next stable transition is everywhere T_h, and as already pointed out, T_{end} is in the metastable branch of the solution. Details of further metastable structure at small x_f are shown in the right hand plot. At $x_f \sim 0.25$, the first order T_s transition appears in the metastable branch slightly below T_h, see figure 10. This transition develops into the YM transition in the $x_f \to 0$ -limit. T_{end} crosses above the T_h transition, but it is also in the metastable branch, see figure 12 for details.

The phase diagram for potential II at $W_0 = 0$ is shown in figure 16. For all points shown, T_{end} is below T_h and in the metastable branch. The crossover exists when $x_f \gtrsim 3.6$ and again between $x_f = 0$ to ~ 0.7. The close-up of the small x_f -region in the right hand plot shows the crossover and the hadronisation transition T_h, with the T_{end} and T_s transitions in the metastable branch. As a new feature the crossover also becomes metastable for $0.5 \lesssim x_f \lesssim 0.7$.

Finally, let us comment on the x_f dependence of the transition temperature(s). For SB normalised W_0 or $W_0 = 24/11$ (figures 13 and 14), T_h and T_{end} decrease with increasing x_f, in qualitative agreement with estimates based on field theory [74–77]. Decreasing W_0 to 12/11 (figure 15), however, the x_f dependence becomes almost flat, and for $W_0 = 0$ (figure 16) the temperatures increase with x_f up to $x_f \simeq 3.5$. Rather similar behavior with varying W_0 will be found for potentials I below, where the x_f-dependence is partially disturbed by the additional structure appearing at low x_f.

Figure 15. *Left*: the phase diagram for potential II at $W_0 = 12/11$, $x_c = 4.08$. The dashed box shows the region detailed in the other plot. For discussion, see text.
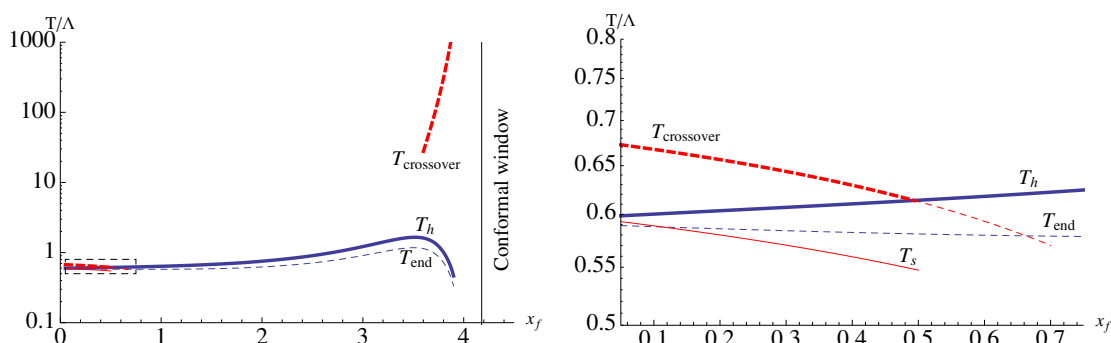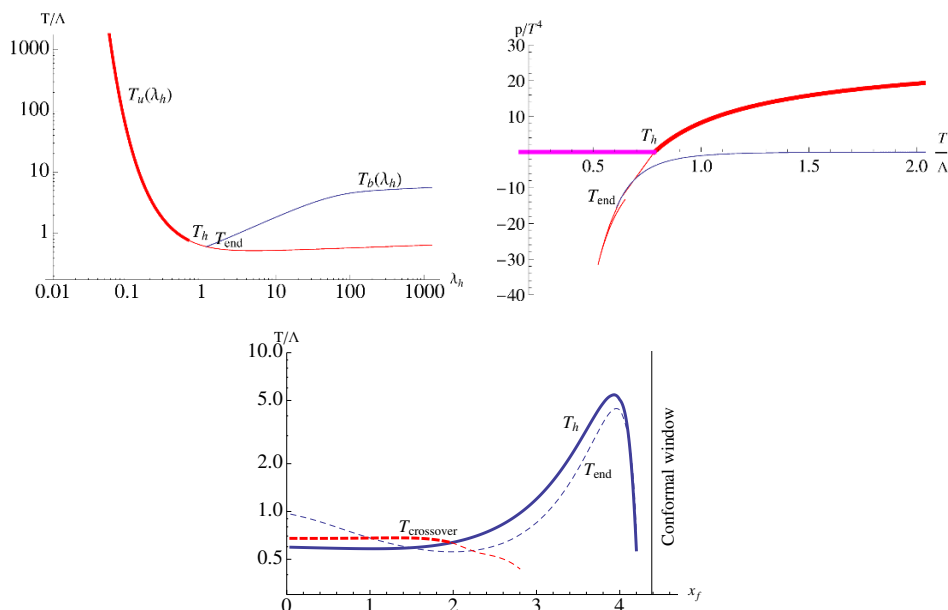

Figure 16. *Left*: the phase diagram for potential II at $W_0 = 0$, $x_c = 4.18$. The dashed box shows the region detailed in the other plot. For discussion, see text. $T_{\text{crossover}}$ continues into the conformal window.

4.3 Class-II$_*$ potentials

In this section, we consider the phase diagram corresponding to the potential II$_*$. Recall that the star subscript refers to the fact that the potential $V(\lambda) = V_g(\lambda) - x_f V_{0f}(\lambda)$ has an extremum only for $x_* < x_f$, while for the cases discussed earlier such extremum exists for all values of x_f; see section 2.2.2 for detailed definitions.

The resulting (x_f, T) -phase diagram is shown in figure 17, the top panel shows how the phase diagram is derived at $x_f = 2.5$. Starting at large T one is in the tachyonless black hole phase (thick red curve). At $T_h \approx 0.8\Lambda$ pressure goes to zero and the ground state is the thermal gas phase with $p = 0$. If one could supercool further one would at T_{end} meet the chirally broken tachyonic black hole phase. It has a higher free energy than the stable broken phase and therefore is unstable.

The main features are that the crossover exists only for small values of x_f, $x_f \lesssim 2$ where it nearly coincides with T_h, and again at larger values $x_f \gtrsim 3.5$, where it is clearly separated from T_h. The second order endpoint T_{end} remains in the unstable phase for $x_f \leq x_c$. Below the conformal window, for values $2 \lesssim x_f \lesssim 4$ both T_h and T_{end} increase. They reach their maximum and finally start to decrease (as predicted by the Miransky scaling) only around $x_f = 4$, very near the boundary of the conformal window. This suggests that the modification of the potential has the tendency to "squeeze" the walking region.

Figure 17. Phase diagram for potential II$_*$ with W_0 SB normalised (bottom). The top panel shows $T = T(\lambda_h)$ and p/T^4 at $x_f = 2.5$. $T_{\text{crossover}}$ reappears at about $x_f = 4$ at a temperature well above the range shown here, and continues into the conformal window.

4.4 Class-I potentials

For class I potentials figure 18 shows phase diagrams for $W_0 = 0, 12/11, 24/11$ and for the SB-normalised case. Recall that for these potentials the tachyon diverges exponentially in the IR. The choices of a and κ are given in eqs. (2.36). We also remind that transitions between stable phases are plotted as thick lines. Transitions plotted as thin lines can be seen only if the system is, e.g., supercooled, so that they are not there in the thermodynamic limit.

One can observe several characteristic features for varying W_0:

- The first observation is the striking structure near $x_f = 0$ which is observed at large W_0, i.e., for $W_0 = 24/11$ or SB normalized. The temperatures T_h and T_{end} drop rapidly with decreasing x_f near $x_f = 0$ and reach zero at a finite value of x_f. Below this critical value, all phases are chirally symmetric.

  This behavior is related to the tachyon mass at the IR fixed point, shown in figure 3. For PotI (the absolute value of) the squared tachyon mass is below the BF bound for low values of x_f. Therefore it is not guaranteed that a solution with zero quark mass and nontrivial tachyon profile exists (at any temperature) in this region. For large W_0 it actually turns out that the solution with $m_q = 0$ and nontrivial tachyon profile does not exist for very low x_f, which explains the absence of chiral symmetry breaking. This implies that this potential is not describing a QCD-like theory. However, the applicability of PotI can be rescued by a simple logarithmic modification of $\kappa(\lambda)$, see section 4.6 and figure 20.

- The symmetric→ symmetric transition T_s becomes a stable transition when $W_0 = 24/11$ or SB normalized. For comparison, for PotII it was always in a metastable phase. This happens mostly in the region of very low x_f where all phases are chirally symmetric so that T_h and T_{end} are absent. For $W_0 = 24/11$ we observe a region with $0.25 \lesssim x_f \lesssim 0.45$ where these transitions are also present. In this case the order of transitions is $T_s > T_{\text{end}} > T_h$, and chiral symmetry is broken in the middle one. For W_0 SB normalized we find instead a region with $0.2 \lesssim x_f \lesssim 0.5$ where only the crossover exists, so that the phase structure is similar to the conformal window.

- At large $x_f \gtrsim 3$, $W_0 = 12/11$, one observes the splitting of the 1st order line T_h into two 1st order lines $T_{12} > T_h$. The order of the transitions is $T_{\text{end}} > T_{12} > T_h$, chiral symmetry is broken at the largest one, T_{end}. The holographic action therefore gives two consecutive 1st order transitions within the chirally-broken phase. It is an open issue what the nature of these transitions is. It is plausible that PotI at large W_0 is not related to QCD-like theories.

- The high temperature crossover exists over a larger and larger range when W_0 increases and ultimately appears at all x_f. This is the same tendency seen also for potentials in the II class.

4.5 Class-I$_*$ potentials

Finally, we present the phase diagram corresponding to the potential I$_*$ in figure 19. The striking difference between the phase diagram of the potential I$_*$ in comparison with potential II$_*$ considered earlier is that for small values of $x_f \lesssim 2$ there are no solutions with broken chiral symmetry, not even at low temperatures; all phase boundaries here are between chirally symmetric phases. There is T_h, but now it describes a chirally symmetric → symmetric transition. To illustrate this we show explicitly $T = T(\lambda_h)$ at $x_f = 1$. It is very structureless, and has no solutions with nonzero tachyon. Thus the (λ_f, T) -diagram is qualitatively similar to the Yang-Mills case [33–35]. Only above $x_f \sim 2$ and below x_c is chiral symmetry broken at low temperatures.

Otherwise the overall features are similar to those in the case of potential II$_*$. For small values of x_f, $x_f \lesssim 2$, the crossover nearly coincides with T_h . The second order endpoint, T_{end}, is in the unstable branch for small values of x_f, but enters into the stable branch at $x \sim 4$. Below the conformal window, for values $2 \lesssim x_f \lesssim 4$ both T_h and T_{end} increase. They start to decrease only at $x_f \sim 4$, very near the boundary of the conformal window.

We have also studied the potentials I$_*$ for the case of fixed W_0 and found qualitatively similar results for the phase structure for $W_0 = 12/11, 24/11$. For $W_0 = 0$ the problematic region without chiral symmetry breaking is absent, and the phase diagram is similar to PotII$_*$. This implies that, like Pot I, this type of potential is probably not applicable for QCD-like theories when W_0 is large.

4.6 PotI with logarithmic correction to $\kappa(\lambda)$

The function $\kappa(\lambda)$ in the action (2.2) represents the effects of going from the string frame (to which the derivation of the DBI action as the $\alpha' \to 0$ limit of open strings leads)
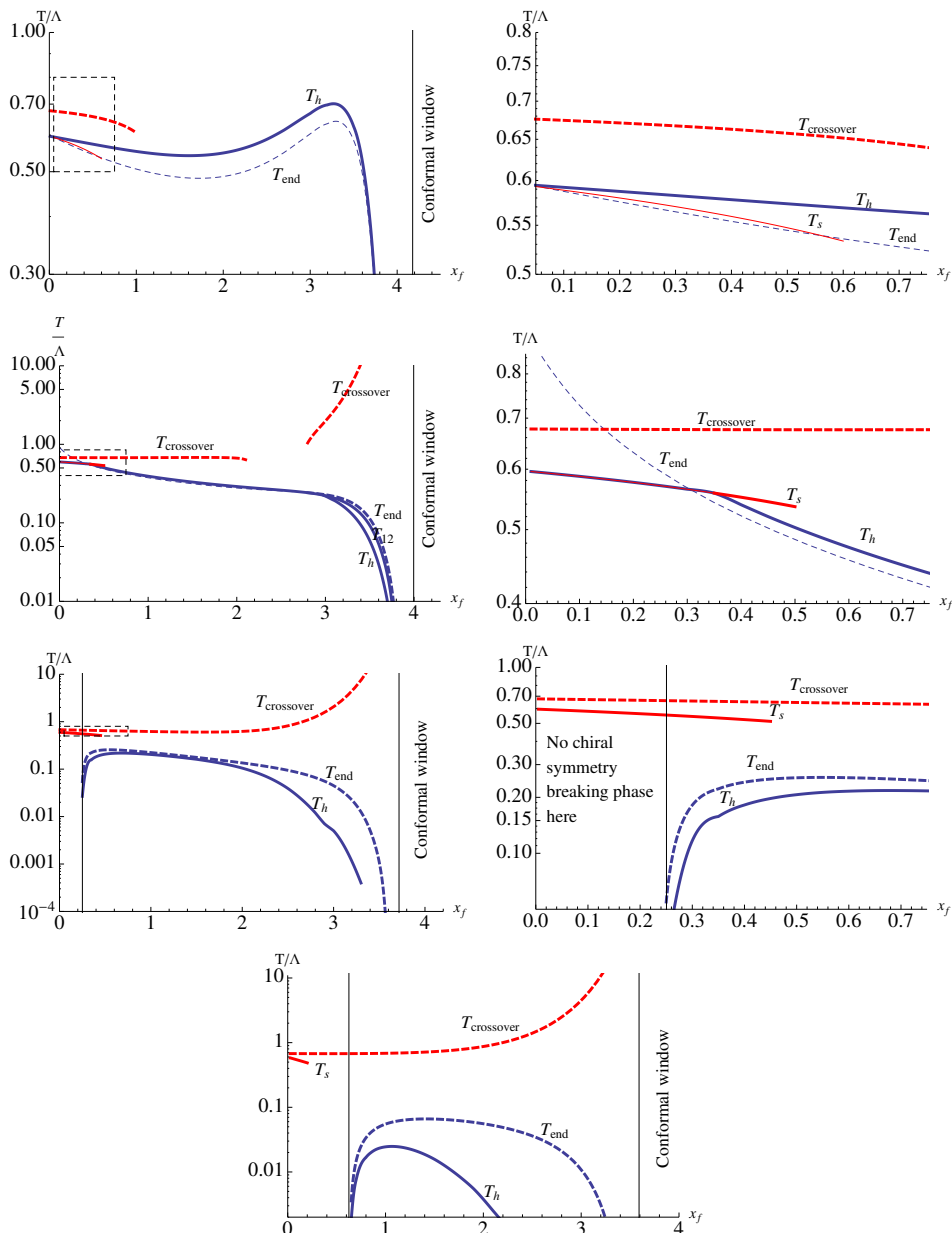
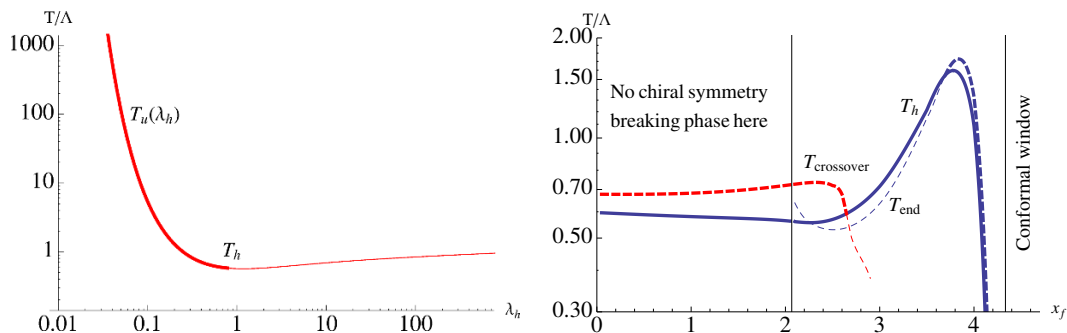**Figure 18**. Phase diagrams for potential I. *Top*: $W_0 = 0$; *Middle ones*: $W_0 = 12/11, 24/11$; *Bottom*: SB normalisation of W_0. A blow-up of the small x_f region is shown at right separately for three top rows. The leftmost vertical line in the bottom three figures denotes the value of x_f below which chiral symmetry breaking solutions do not exist.

and the Einstein frame (where the gravity dual is formulated). Extending the conformal transformation relating these to UV by $\lambda \to 1+\lambda$ one has, in terms of the metric functions,[15]

$$\kappa(\lambda) = \frac{1}{(1+\lambda)^{4/3}} = \frac{b^2}{b_s^2}. \tag{4.1}$$

---

[15]Notice that we introduced additional constants in the formulas (2.36) and (2.38) in order to match with the perturbative anomalous dimensions in QCD.

Figure 19. Phase diagram for potential I_* with SB normalisation of W_0. The left panel shows $T = T(\lambda_h)$ at $x_f = 1$: no tachyonic black hole!

where b and b_s are the metric factors in the Einstein and string frames, respectively.

The potential (2.27) carries the factor $\lambda^{4/3}$, but also the logarithmic factor $(\ln \lambda)^{1/2}$, which plays a quantitatively important role: for $(\ln \lambda)^P$ the excitation spectrum is $m \sim n^P$ [30–32] and one wants the Regge-like spectrum, $P = 1/2$. Also numerically $\ln \lambda$-effects are important, see figure 7. To study these effects in κ we use the parametrisation

$$\kappa(\lambda) = \frac{[1 + \ln(1 + \lambda)]^{\bar{\mu}}}{[1 + \frac{3}{4}(\frac{8}{9} b_0 + 1 + \bar{\mu})\lambda]^{4/3}}. \tag{4.2}$$

There are constraints on this parametrisation from the UV and IR. First, to maintain the proper mass anomalous dimension equation (2.26) at small λ, $\bar{\mu}$ has to appear also in the denominator as shown in (4.2). Secondly, for $\bar{\mu} = 0$ the tachyon grows exponentially in r according to eq. (2.37). The effect of $\bar{\mu}$ on this comes from the change $b^2/\kappa = \sqrt{\ln \lambda}/(\ln \lambda)^{\bar{\mu}} \sim r^{1-2\bar{\mu}}$ (in the IR $r \sim \sqrt{\ln \lambda}$, see (B.4)). This effect propagates through the computation of the r dependence which comes out to be $\tau(r) \sim \exp(C r^{1-2\bar{\mu}})$, indicating that $\bar{\mu} < 1/2$.

The most interesting effect comes from evaluating the tachyon IR mass using (2.42). The result is shown in figure 20, to be compared with figure 3. The difficulty with PotI was that at small x_f the curve in the left panel of figure 3 dropped below the BF bound. The reason for this is easy to see analytically by studying the $\lambda^* \to \infty$ limit of (2.42), which gives $-m_{\rm IR}^2 \ell_{\rm IR}^2 \sim (-\ln x_f)^{-1/2}$ in this case. For small x_f, λ^* approaches infinity and obviously negative values of $\bar{\mu}$ increase the tachyon mass $-m_{\rm IR}^2 \ell_{\rm IR}^2$, so that $-m_{\rm IR}^2 \ell_{\rm IR}^2 \sim (-\ln x_f)^{-\bar{\mu}-1/2}$ For $\bar{\mu} < -1/2$ it even grows without bounds as for PotII in figure 3. This is seen in figure 20.

As a consequence, the phase diagram for PotI with log-modified κ does not suffer from the problems at small x_f described earlier for PotI. The phase diagram computed for $\bar{\mu} = -\frac{1}{2}$ is shown in figure 20 and, in fact, resembles qualitatively those for PotII. This is very gratifying since PotI also leads to a Regge-like particle spectrum [70]. PotI with log-modified $\kappa(\lambda)$ (4.2) thus seems to be the gravity dual leading to the simplest thermodynamics in figure 8 and the expected Regge-like hadron spectrum. It is interesting that also PotII, a dual with spectrum of type $m \sim n$, also leads to the simple thermodynamics in figure 8.
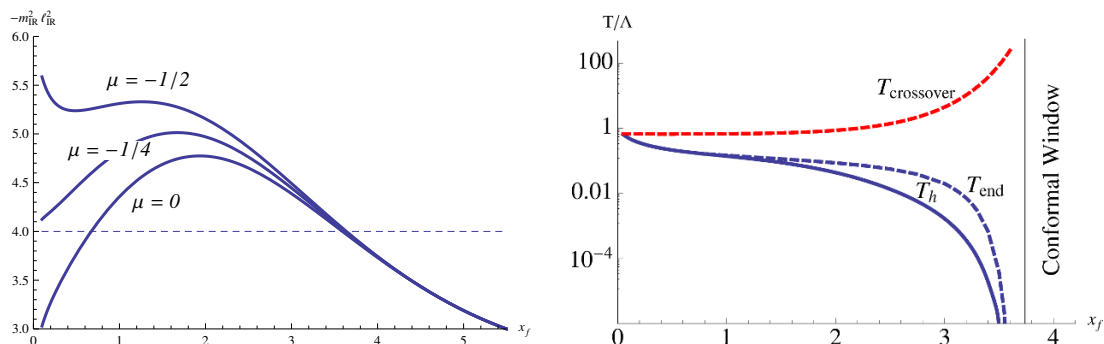
Figure 20. *Left*: the tachyon mass at λ^* for PotI with log-modified $\kappa(\lambda)$, evaluated using eqs. (2.42) and (4.2) for $\bar{\mu} = 0, -\frac{1}{4}, -\frac{1}{2}$. The $\bar{\mu} = 0$ curve is the same as the red dotted curve in left panel of figure 3. *Right*: the phase diagram for PotI with SB-normalised W_0 with $\kappa(\lambda)$ given by (4.2) with $\bar{\mu} = -\frac{1}{2}$. T_{end} intersects T_h at $x_f = x_\chi = 0.72$. $T_{\text{crossover}}$ is the same as in figure 18, bottom.

4.7 The conformal window

A detailed picture of thermodynamics in the conformal window is shown in figure 21. Here p/T^4, i.e. the effective number of degrees of freedom, is plotted for some values of $x_f > x_c$. At large T it is normalised so that it approaches the SB limit (3.38) for any x_f. For T approaching zero, p/T^4 approaches another constant, the value of which decreases when x_f approaches x_c from above. For all x_f, the vacuum phase has zero pressure, and at the limit $T \to 0$ there is a transition from the black hole to the thermal gas phase. When x_f approaches the upper end of the conformal window $11/2$, the behavior of the curves can be worked out analytically in perturbation theory [71] since the coupling then is small.

For the present potential the finite temperature transition between the low and high temperature phases inside the conformal window is a smooth crossover. Figure 21 also plots the interaction measure, the maximum of which defines the critical temperature for this crossover. Note that even if the transition here is smooth crossover, the transition can also be of 1st order in different theories [45]. What determines this behavior is the overall magnitude of the beta function. For illustration, consider the beta function of large N_f QCD, $\beta = -b_0 \lambda^2 - b_1 \lambda^3 + \ldots$. The values of the coefficients behave as $b_0 \sim \mathcal{O}(1) \ll |b_1|$, while the results of [45] suggest $b_0 \sim \mathcal{O}(10) \sim |b_1|$ for 1st order phase transition. For the models we have considered here, we find that the nonperturbative beta function extracted from the gravity solution is small over the entire range $0 \le \lambda \le \lambda_*$ inside the conformal window.

The large temperature values appearing in figure 21 may appear somewhat surprising. However, they have a simple explanation. The region in which p/T^4 is nearly constant and approaching its large T limit is the perturbative region λ small. The conformal window is within $0 < \lambda < \lambda^*(x_c)$ and the upper limit is always small, $\ll 1$, so that the conformal window is perturbative, down to $T = 0$. From figure 2 one sees quantitatively how this holds even somewhat below the conformal window. To 1-loop $\log T = \exp(1/(b_0\lambda))$ and clearly for $b_0 \to 0$ this grows fast. Somewhat more quantitatively, the beginning of the large T region can be estimated by computing the value of T for which the 2-loop correction
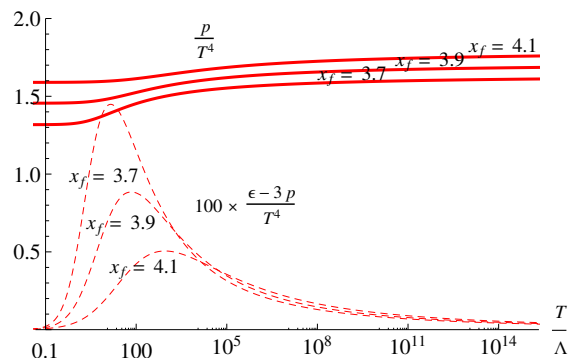
Figure 21. Thermodynamics for some values of x_f within the conformal window, computed for PotI. Note that in the conformal window always $\tau = 0$ and the functions $a(\lambda)$, $\kappa(\lambda)$ do not affect the result.
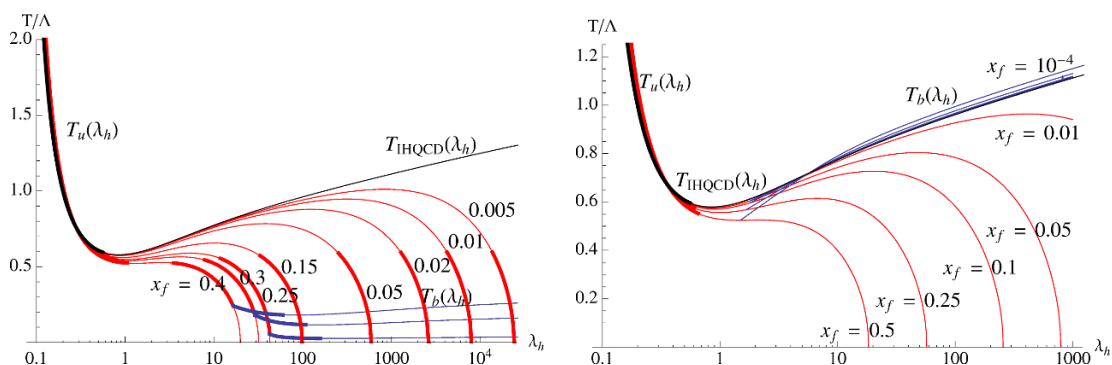
Figure 22. $T(\lambda_h)$ for various small values of x_f and for potential I, $W_0 = 24/11$ (*Left*) or for potential II, $W_0 = 12/11$ (*Right*). The black curve is the IHQCD limit. The chirally unbroken $T_u(\lambda_h) \equiv T(\lambda_h, \tau = 0)$ branch asymptotes to the IHQCD curve as $x_f \to 0$, for both potentials. The chirally broken $T_b(\lambda_h) \equiv T(\lambda_h, \tau_h(\lambda_h, m_q = 0))$ branches behave very differently for PotI and PotII. For PotI T_b is absent at such low x_f and all phases are chirally symmetric (see also figure 18). For PotII the curves T_b follow very closely T_s and, correspondingly, $T_h \approx T_s$ (see figure 15).

term in the perturbative expansion of $1/\lambda(\mu)$ equals the 1-loop term. One finds that the 2-loop correction is smaller than the 1-loop term if $T > (2 \log T)^{|b_1|/b_0^2}$, $|b_1|/b_0^2 = 3|13x_f - 34|/(2(11 - 2x_f)^2)$. This is always true for $T > 1 = \Lambda$ if $x_f < 3.6$. However, for $x_f > 3.6$ this gives a lower limit of T which grows extremely fast when x_f grows within the conformal window. $T_{\text{crossover}}$ is somewhat below the solution of this equation. Numerical values are in qualitative agreement with figure 21.

4.8 The limits $x_f \to 0$ and $x_f \to x_c$

The V-QCD models at $x_f = 0$ are equivalent to an IHQCD model with potential V_g. One thus expects that the hadronisation transition T_h will approach the 1st order deconfining transition of SU(N_c) YM theory[16] when $x_f \to 0$. However, for PotI and large W_0 this

---

[16]Note that strictly speaking the limit of YM theory demands $N_f = 0$ and falls outside the Veneziano limit $N_f \to \infty$ of QCD. This may explain the nontrivial structures observed at $x_f \to 0$.

cannot be the case, since the hadronisation transition does not exist for very low x_f, as we pointed out above. Indeed we see from the phase diagrams of figure 18, that the symmetric transition T_s, which only exists for $x_f \lesssim 0.4$, is the precursor of the YM transition in this case.

Let us then discuss in detail what happens in the $x_f \to 0$ limit in the two cases and at finite temperature. Since thermodynamics is determined by the set of $T(\lambda_h)$ curves in figure 7, one should study how this configuration behaves when $x_f \to 0$. The $T(\lambda_h, \tau = 0)$ curve (shown in red in figure 7) exists only for $\lambda < \lambda^*$ and, according to the definition (2.40) $\lambda^* \to \infty$ when $x_f \to 0$. In more detail, the limit is given by

$$\lambda_*^{2/3} = \frac{8}{W_0 + \frac{20568}{4619}} \frac{1}{x_f} \sqrt{\ln \lambda_*}, \quad V(\lambda_*) = \frac{18476}{729} \lambda_*^{4/3} \sqrt{\ln \lambda_*}. \tag{4.3}$$

where the equation on the left determines λ_* while the equality on the right expresses $V(\lambda_*)$ as a function of λ_*. Eq. (4.3) is valid both for potentials I and II. The red curves of figure 7, therefore, stretch to the right when $x_f \to 0$. Quantitatively what happens is shown in figure 22 and one sees that they approach the $T(\lambda_h)$ curve of IHQCD when $x_f \to 0$. This is as expected since only V_g remains in the limit. It is thus obvious that T_s approaches the transition temperature of IHQCD as $x_f \to 0$ (but it may be a transition between two metastable phases rather than a physical transition).

To find the relative behavior of T_s and T_h one needs the asymptotic properties of the curves $T_b(\lambda_h) \equiv T(\lambda_h, \tau_h(\lambda_h, m_q = 0))$ (shown in blue in figure 7) which only exist for $\lambda > \lambda_{\text{end}}$. Here PotI and PotII behave in considerably different ways, as is already seen from figures 15 and 18.

The crucial difference between PotI (at large W_0) and PotII comes from the fact that for PotI the value of λ_{end} (the endpoint of the blue $T_b(\lambda_h)$ curves in figure 22) grows rapidly when x_f decreases, while for PotII λ_{end} remains almost constant. Since always $T_u(\lambda_{\text{end}}) = T_b(\lambda_{\text{end}})$ and $T_u(\lambda_h)$ decreases rapidly at large λ_h, also the temperature T_{end} becomes small at small x_f for PotI. This drives the whole curve $T_b(\lambda_h)$ towards zero and since T_h is determined by integration along $T_b(\lambda_h)$ also $T_h \to 0$. Finally λ_{end} ceases to exist when x_f goes below a critical value ~ 0.25, the temperatures T_{end} and T_h reach zero, and the low temperature chiral symmetry breaking phase disappears.

For PotII $T_b(\lambda_h)$ follows very closely T_{IHQCD} above it (figure 22) and it is thus natural that $T_h \gtrsim T_s$ and that they approach the same limit. T_s is actually metastable (figure 15).

One can also illustrate the connection of the behavior of λ_{end} to the BF bound of the tachyon (figure 3) by analyzing the linearized tachyon equation motion as discussed in appendix D.

In the limit of $x_f \to x_c$ one expects that all dimensionful quantities sensitive to the IR vanish as specified by Miransky scaling (1.8). All our numerical results are compatible with this, but conclusive numerical verification would require extensive further work. Analytic arguments supporting the scaling, similar to those presented in section 10 of [26], can also be constructed in the finite temperature case. We shall here, however, only briefly comment on the scaling as well as the overall behavior of the solutions as $x_f \to x_c$ from below.
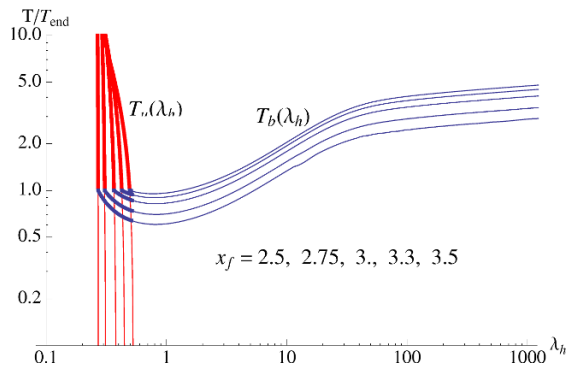
Figure 23. The temperatures $T_u(\lambda_h)$, $T_b(\lambda_h)$ of the two black hole branches, unbroken and broken, scaled to the temperature $T_{\rm end}$ for PotII, W_0 SB normalized. The values of x_f from top to bottom are 2.5, 2.75, 3, 3.3, and 3.5. Compare to figures 9 and 13.

We start with the case of zero temperature which is simpler. For $x_f < x_c$ the dominant background is the one with nontrivial tachyon, and chiral symmetry is broken. As $x_f \to x_c$ the solution comes closer and closer to the fixed point, and the near conformal region grows. As it turns out, the pieces for $\lambda > \lambda_*$ and $\lambda < \lambda_*$ approach separately fixed solutions in this limit, which do not talk to each other.[17] Thus any observable which can be expressed only in terms of either the UV or the IR solution approaches a fixed value in the $x_f \to x_c$ limit. The ratio of the characteristic scales of the two pieces diverge as specified by the Miransky scaling factor of eq. (1.8).

It is hard to find simple examples of such observables at zero temperature, but as it turns out, at finite temperature there are plenty. However, the analysis of the limit is more involved, since we have the additional parameter λ_h we can be either in the UV ($< \lambda_*$) or in the IR ($> \lambda_*$) regions. The curve which determines the main features of the thermodynamics is $T_b(\lambda_h)$, which lies mostly in the IR region. Its endpoint $\lambda_{\rm end}$ is however smaller than λ_*. When $\lambda_h > \lambda_*$ we expect that the background solution breaks into two parts similarly as for $T = 0$ in the limit $x_f \to x_c$, and the temperature is determined solely by the IR piece.[18] In the limit $x_f \to x_c$ we find[19] that $\lambda_{\rm end} \to \lambda_*$ from below. Therefore the whole $T_b(\lambda_h)$ curve is in the IR region in the strict $x_f \to x_c$ limit, and it is plausible that it takes a fixed shape.

This behavior is supported by the numerical study of figure 23, where we plot the temperatures of the two black hole branches as functions of λ_h for PotII with W_0 SB

---

[17]More precisely, keeping fixed the scale $\Lambda_{\rm IR}$ defined by the IR expansions, the background approaches pointwise a "IR" limiting solution which flows from the good IR singularity to the fixed point at $\lambda = \lambda_*$. This solution which approaches λ_* from the "wrong" side is possible due to the presence of the tachyon. Keeping the UV scale $\Lambda_{\rm UV}$ fixed instead, the "UV" limiting solution is the one that flows from the IR fixed point at $\lambda = \lambda_*$ to the standard UV fixed point at $\lambda = 0$ with zero tachyon.

[18]There is a subtlety here as comparing temperatures at different λ_h requires fixing the units of energy, which we do by calculating $\Lambda_{\rm UV}$. However for $\lambda_h > \lambda_*$ the UV part of the solution, and hence practically the units of energy, become independent of λ_h in the limit $x_f \to x_c$. Thus we could equally well define the units in terms of the behavior of the IR piece of the solution near $\lambda = \lambda_*$.

[19]This is observed numerically, and can be understood by studying the violation of the BF bound in the spirit of appendix D.
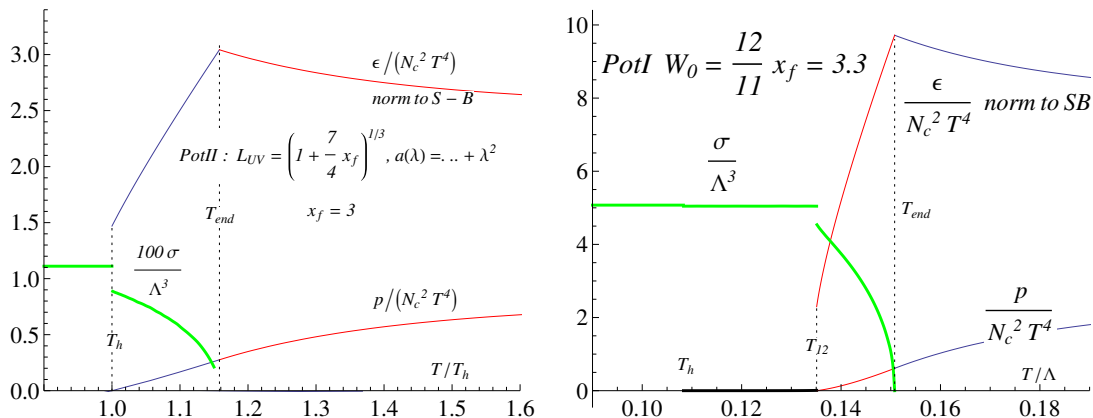
Figure 24. Examples of equation of state with $\bar{q}q$ condensate. *Left*: type II SB-normalised potentials at $x_f = 3$ (compare figures 9 and 13). Note the scaling of σ by a factor 100. *Right*: type I potentials with $W_0 = 12/11$ and $x_f = 3.3$ (compare figure 18, middle panel).

normalized. The x_f-dependence of the curve $T_b(\lambda_h)$ is, up to the overall normalization, so small for $\lambda_h \gg \lambda_*$ that it cannot be resolved from the plot even at relatively low $x_f \lesssim 3$. The main effect with increasing x_f is that the $T_b(\lambda_h)$ curve is visible down to lower and lower λ_h as λ_* decreases slowly, while the shape of the curve remains fixed. The curve $T_u(\lambda_h)$ approaches a vertical line when scaled to T_{end}, reflecting the fact that $\lambda_{\mathrm{end}} \to \lambda_*$.

The values of all the critical temperatures (except $T_{\mathrm{crossover}}$), as well as all thermodynamics up to the transitions, are determined by $T_b(\lambda_h)$ as $x_f \to x_c$. Therefore, we expect that the thermodynamics "freezes" in this limit, in the sense that all ratios of the critical temperatures approach fixed values. Moreover, the parts of the thermodynamical functions which are determined by the IR solutions, are expected to have well defined limits. While we have not proven these statements, they are strongly supported by the numerical study of figure 23. Notice however, that our data only extends up to $x_f = 3.5$ which is still well below the critical value $x_c \simeq 3.70$. Therefore we cannot exclude the possibility that something drastic happens for x_f even closer to x_c.

5 The chiral condensate

In principle, it should be straightforward to extract the chiral condensate $\propto \sigma$ from the tachyon solution in the UV

$$\tau(r) \sim \sigma r^3 (-\ln(\Lambda r))^{3/(2b_0)}, \quad r \to 0, \tag{5.1}$$

as the quark mass is set to zero. However, in this model the task is actually very demanding due to the logarithmic corrections (i.e., the running of the condensate) and the fact that the numerical solutions have a tiny residual quark mass due to limited numerical precision. These issues and their resolution are discussed in appendix E.

Examples of the correlation of σ with that of the free energy are shown figure 24. One expects that σ jumps in a 1st order transition. The first case is thermodynamics for SB-normalised type II potentials at $x_f = 3$, also studied in figures 9 and 13. Cooling from large
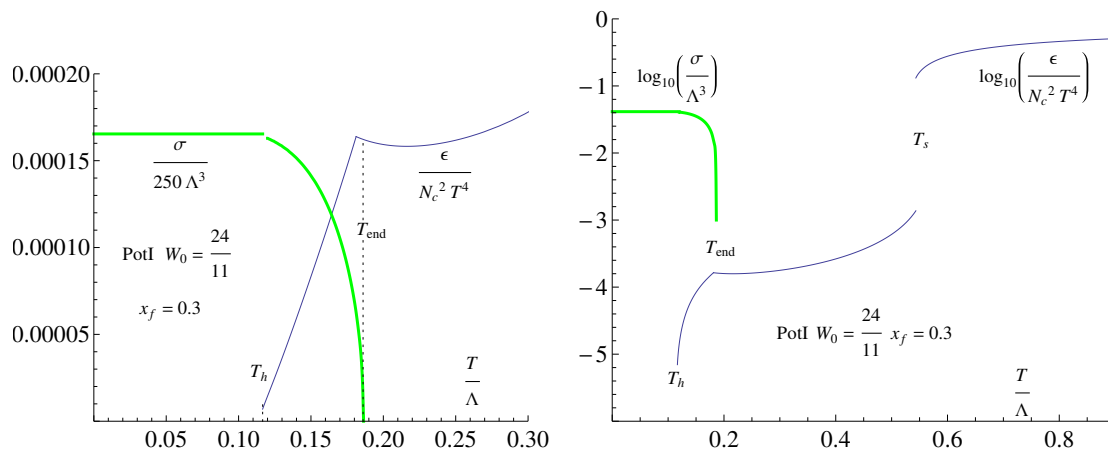
Figure 25. The condensate for the Pot I, $W_0 = \frac{24}{11}$ phase diagram in the right hand column of figure 18 at $x_f = 0.3$ in linear (*Left*) and log (*Right*) scale. Note the scaling of σ by a factor $1/250$ in the left panel. The right panel shows all the three transitions in figure 18.

T chiral symmetry first breaks at the 2nd order transition $T_{\rm end}$ and the condensate starts from zero and increases with further cooling. At T_h the system experiences a 1st order transition and σ jumps the amount shown in the figure. Below that σ remains constant in the present models, which does not describe the thermodynamics of the low T phase. In that the degrees of freedom are N_f^2 massless Goldstone bosons.

A second example is thermodynamics with condensate of Type I potentials with $W_0 = 12/11$ and $x_f = 3.3$. This case is special in that in it the 1st order line T_h splits in two 1st order transitions at T_h, T_{12} if $x_f \gtrsim 2.8$, as shown explicitly in figure 18, middle panel. Again the highest temperature transition is a 2nd order one at $T_{\rm end}$, at which the condensate starts to grow when the system is cooled. The condensate grows up to the value $\sigma = 4.537\Lambda^3$. Then there is a 1st order transition at T_{12} with a jump in σ and latent heat:

$$\frac{\Delta\sigma}{\Lambda^3} = 0.508, \quad \frac{\Delta\epsilon}{T_{12}^4} = 2.29 \tag{5.2}$$

and finally a very weak transition at T_h with the value

$$\frac{\Delta\epsilon}{T_h^4} = 1.03 \cdot 10^{-7}. \tag{5.3}$$

It is clear that the value of σ also jumps at the latter transition, but the size of the jump is so small that we could not extract it reliably from the numerics.

As a third example, consider the case Pot I, $W_0 = \frac{24}{11}$ at $x_f = 0.3$, which is very special in that T_h is very small and it is T_s which dominates, as is seen in the right hand column of figure 18. The magnitudes vary so much that all the transitions can be presented only on log scale, see figure 25.

At the 2nd order transitions the condensate goes to zero continuously as the temperature approaches $T_{\rm end}$ from below. The curves in figures 24 and 25 seem to be compatible with the standard expectation $\sigma \sim \sqrt{T_{\rm end} - T}$. We study this more precisely in figure 26
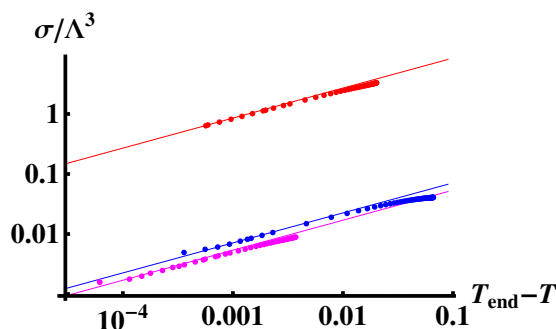
Figure 26. The condensate as a function of $T_{\rm end} - T$ in log-log scale. The dots are our data, extracted from the background solutions, and the lines are fits having the form $\sigma = C\sqrt{T_{\rm end} - T}$. The choices of potentials are, from top to bottom: PotI with $x_f = 3.5$ and $W_0 = 12/11$ (red); PotI with $x_f = 0.3$ and $W_0 = 24/11$ (blue); and PotII with $x_f = 3$ and SB normalized W_0 (magenta).

where we plot our data for the condensate for T close to $T_{\rm end}$ in the log-log scale for various choices of the potentials. The data are compared to the lines $\sigma = C\sqrt{T_{\rm end} - T}$, with the coefficients C chosen such that the lines overlap with the tails of the data at small $T_{\rm end} - T$. It is convincing that $1/2$ is indeed the correct exponent.

6 Nonzero quark mass and thermodynamics

We have so far mainly discussed the case of vanishing quark mass, for which chiral symmetry may hold. Effects of nonzero quark mass have been mentioned in subsection 3.3.2 and described in figures 6 and 7. They follow from the fact that tachyonfree black hole solutions do not exist, as a reflection of the disappearance of chiral symmetry. However, numerically the tachyonic small-m_q solutions are very close to the zero mass tachyonfree solutions in the UV at small λ, as is seen by comparing left and right panels of figure 7. Thus chiral symmetry is always broken even in the high-T phase, but quantitative effects are small at large T.

The effects of small nonzero m_q are shown quantitatively in figure 27 and can be summarised as follows:

- The main effect follows from the fact that for nonzero m_q even the high T phase is chirally broken. The curve marked $m_q = 0$ is the same $T_h(x_f)$ as that in figure 13. For this case the phase at $T > T_h$ is chirally symmetric and chiral symmetry is broken when T decreases below T_h. For nonzero m_q also the phase at $T > T_h$ is chirally broken and the effective order parameter of the transition is the jump in entropy or energy density. There is also a jump in the condensate, but the condensate is nonzero also for $T > T_h(x_f)$.

- For x_f clearly below x_c the effects of small m_q on the phase diagram are small. Particularly interesting is the pattern of approach towards $m_q = 0$. The smaller m_q, the higher is the value of x_f where the curves start deviating significantly.
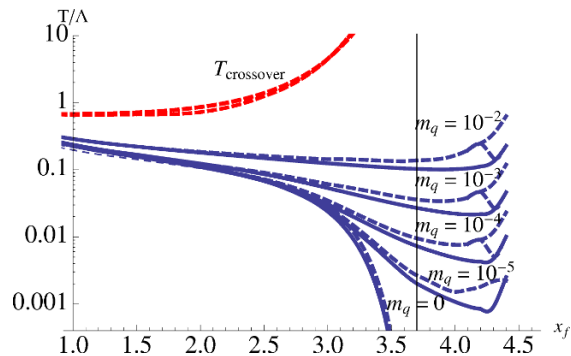
Figure 27. The behavior of $T_h(x_f)$ (in units of $1/\mathcal{L}_{\mathrm{UV}}$, over the x_f range in the figure this unit changes by about 30%) for $m_q = 0$ and for small values of m_q. For $m_q = 0$ the dashed line shows the true 2nd order chiral symmetry breaking transition. For nonzero m_q the line shows the position of one maximum of the interaction measure, a second one gives the usual $T_{\mathrm{crossover}}$ (which is almost independent of m_q).

- The 2nd order transition at T_{end} becomes a continuous one. This is obvious from figure 7, there is no discontinuity near T_{end}. However, a remnant of the genuine transition is a maximum of interaction measure, also plotted in figure 27.

- At large x_f the conformal window and Miransky scaling disappear. For $m_q = 0$ the transition temperature T_h vanishes when $x_c - x_f \to 0$ as dictated by Miransky scaling. The smallest nonzero mass destroys this effect and T_h curves upwards towards larger values.

- The effect of nonzero mass could also be seen by plotting the beta function for values of x_f within the conformal window. For $m_q = 0$ only the tachyonless solutions matter and they extend only up to λ^* in figure 7. The beta function $\beta(\lambda)$ only exists for $\lambda < \lambda^*$ and $\beta(\lambda^*) = 0$ at the IR fixed point λ^*. For $m_q > 0$ the beta function comes close to λ^* but continues past it to larger values of λ.

7 Outlook

In this paper, we have used bottom-up holography to study the thermodynamics of models that are in the universality class of QCD with massless quarks in the Veneziano limit, (large N_c and N_f but fixed $x_f = N_f/N_c$).

The temperature dependence of the pressure $p(T)$ and the condensate $\sigma(T) = \langle\bar{q}q\rangle(T)$ was computed at various x_f up to the loss of asymptotic freedom at $x_f = 11/2$ with a conformal window appearing at $x_c < x_f < 11/2$, $x_c \approx 4$. The singularities of these quantities define the phase diagram of the system.

One expects that the system has two phases, a low temperature phase with broken chiral symmetry and a chirally symmetric high T phase. The simplest alternative is that these are separated by a 1st order transition at some $T = T(x_f)$, see figure 8. In holography, the high T phase is a metric with a black hole and a new feature appears: this phase

can be either chirally symmetric (no tachyon) or chirally broken (nonzero tachyon). The same doubling applies to the low T thermal gas phase. The phase structure can be correspondingly more complicated. For given gluonic and fermionic potentials of the V-QCD action the thermodynamics is fixed and calculable.

A typical prediction of the model is that there indeed is a 1st order line for x_f from 0 up to some value $\leq x_c$. In holography this is a transition at some $T = T_h(x_f)$ between a non-tachyonic black hole metric and a thermal gas metric with a tachyon. In field theory language one would say that at this temperature there is deconfinement and chiral symmetry breaking with coinciding deconfinement and chiral temperatures, $T_d = T_\chi$. However, a new interesting feature is that at larger x_f this 1st order line can split in two: first at higher T chiral symmetry is broken in a 2nd order transition, then at a lower T there is a 1st order deconfinement transition (see, e.g., figure 13), $T_\chi > T_d$.

A particular feature of the phase diagram is that with x_f approaching x_c all transition temperatures, as all mass scales, decrease as specified by Miransky scaling. Associated with this approach is quasiconformality and walking. At very large T there is always a weak coupling region into which one enters at $T_{\text{crossover}}$. This increases when x_f grows, behaves regularly at x_c and continues further into the conformal window increasing faster and faster (see again figure 13).

Detailed predictions of the model depend on the gluonic and fermionic scalar potentials. There are several physical constraints in deriving them, but they are not uniquely determined. One crucial constraint is missing: in contrast to the application of this model to hot SU(N_c) theory [33–35], there is no 4d lattice data in the large N_c, N_f limit. Thus one is genuinely making predictions and we find that also phase diagrams deviating rather drastically from the above baseline prediction follow from holography. Particularly striking examples are shown in figure 18. In these, the chirally symmetric phase can extend all the way down to zero temperature.

Although we do not expect this to happen in QCD, it may happen in other large N-theories. The last diagram of figure 18 has a structure that is very reminiscent of the phase diagram of high-T$_c$ cuprates, although here we are at zero charge density. In particular the intermediate dome-like structure with chiral symmetry breaking corresponds to the superconducting dome [78] in the cuprate diagram.

One may also note that the models predict a very rich structure of metastable states.

There are many directions in which the model could be further sharpened and developed:

- All the computations are numerically very demanding and much further work would be useful. This holds, in particular, for the approach to the conformal window, $x_f \to x_c$, and for computations of the condensate.

- Effects of non-zero quark mass on the thermodynamics should be studied beyond the discussion in section 6.

- The extension to x_{f1} flavors of mass m_1, etc., is possible but requires a non-abelian version of the Sen action. This is in principle possible to deal with, although we have much less information from string theory on the details of such an action.

- It would be very interesting to accumulate lattice Monte Carlo data in the Veneziano limit. For pure SU(N_c) theory already $N_c = 3$ is very close to $N_c = \infty$ [73, 79]. One might thus see that, e.g., $N_f = 4, 8, 12$ at $N_c = 3$ would already give useful information.

- A chemical potential for baryons should be included. This necessitates the inclusion of a bulk U(1) baryon vector field A_μ. It would be particularly interesting to know the fate of the $T_\chi > T_d$ phase at large x_f and μ.

Acknowledgments

A   UV expansions

The expansions near the standard UV boundary can be computed in a straightforward manner. Let us fix the location of the boundary at $r = 0$. The blackening factor f is very close to unity in the UV,

$$f(r) = 1 + \mathcal{O}(r^4) \ . \tag{A.1}$$

Therefore the leading finite temperature and zero temperature expansions of the various fields coincide. Moreover, as the tachyon vanishes at least linearly in r for $r \to 0$, it can be set to zero when solving for the leading behavior of the coupling λ and the warp factor A. Hence the expansions take the form familiar from earlier works [30–35]. We reproduce here the leading expansions of λ and A as well as the expansions of the non-normalizable and normalizable tachyon expansions both in terms of r and A.

A.1   Fields λ and A

Setting the tachyon to zero, the equations of motion for λ and A involve the effective potential

$$V_{\text{eff}}(\lambda) = V_g(\lambda) - x_f V_f(\lambda, 0) = \frac{12}{\mathcal{L}_{\text{UV}}^2} \left[1 + V_1 \lambda + V_2 \lambda^2 + \cdots \right] \ . \tag{A.2}$$

Then the (leading) UV expansions of A and λ can be found by substituting suitable Ansätze in the equations of motion. The result reads

$$A(r) = -\ln\frac{r}{\mathcal{L}_{\mathrm{UV}}} + \frac{4}{9\ln(r\Lambda)} \tag{A.3}$$

$$+ \frac{\frac{1}{162}\left[95 - \frac{64V_2}{V_1^2}\right] + \frac{1}{81}\ln\left[-\ln(r\Lambda)\right]\left[-23 + \frac{64V_2}{V_1^2}\right]}{\ln(r\Lambda)^2} + \mathcal{O}\left(\frac{1}{\ln(r\Lambda)^3}\right)$$

$$V_1\lambda(r) = -\frac{8}{9\ln(r\Lambda)} + \frac{\ln\left[-\ln(r\Lambda)\right]\left[\frac{46}{81} - \frac{128V_2}{81V_1^2}\right]}{\ln(r\Lambda)^2} + \mathcal{O}\left(\frac{1}{\ln(r\Lambda)^3}\right) . \tag{A.4}$$

Two combinations of the series coefficients of the effective potential appear here. As the potential is matched with perturbative QCD, they become

$$V_1 = \frac{8}{9}b_0 = \frac{88 - 16x_f}{27} \tag{A.5}$$

$$\frac{V_2}{V_1^2} = \frac{23}{64} + \frac{9b_1}{16b_0^2} = \frac{1}{64}\left(23 + \frac{54(34 - 13x_f)}{(11 - 2x_f)^2}\right) \tag{A.6}$$

where b_i are the coefficients of the perturbative QCD beta function. Notice that these coefficients are indeed the same for all potentials used in our study and in particular independent of the choice of W_0.

Let us also present the expansions in terms of A, as we use it as a coordinate in all numerical calculations. The result after the conversion reads

$$\ln r(A) = -A + \ln(\mathcal{L}_{\mathrm{UV}}) - \frac{4}{9A} \tag{A.7}$$

$$- \frac{72\ln(\mathcal{L}_{\mathrm{UV}}\Lambda) - 95 + \frac{64V_2}{V_1^2} + \left(46 - \frac{128V_2}{V_1^2}\right)\ln A}{162A^2} + \mathcal{O}\left(A^{-3}\right)$$

$$V_1\lambda(A) = \frac{8}{9A} + \frac{\left(46 - \frac{128V_2}{V_1^2}\right)\ln A + 72\ln(\mathcal{L}_{\mathrm{UV}}\Lambda)}{81A^2} + \mathcal{O}\left(A^{-3}\right) . \tag{A.8}$$

A.2 The tachyon

As the tachyon is decoupled near the UV boundary, its UV behavior can be studied by inserting the expansions calculated above for λ and A into the tachyon EoM. We also develop the potentials as series in the UV:

$$V_{\mathrm{eff}}(\lambda) = V_g(\lambda) - x_f V_f(\lambda, 0) = \frac{12}{\mathcal{L}_{\mathrm{UV}}^2}\left[1 + V_1\lambda + V_2\lambda^2 + \cdots\right] \tag{A.9}$$

$$xV_f(\lambda) = W_0 + W_1\lambda + W_2\lambda^2 + \cdots$$

$$\frac{\kappa(\lambda)}{a(\lambda)} = \frac{2\mathcal{L}_{\mathrm{UV}}^2}{3}\left[1 + \kappa_1\lambda + \kappa_2\lambda^2 + \cdots\right] . \tag{A.10}$$

Here the leading coefficient of κ/a was already fixed in order to have the correct UV mass of the tachyon [37]. It is enough to study the linear terms in the tachyon EoM, which

become

$$\tau''(r) + \left[-3 + \mathcal{O}\left(\frac{1}{\ln(r\Lambda)^2} \right) \right] \frac{\tau'(r)}{r} \tag{A.11}$$
$$+ \left[3 + \frac{8(\kappa_1 + V_1)}{3V_1 \ln(r\Lambda)} + \mathcal{O}\left(\frac{1}{\ln(r\Lambda)^2} \right) \right] \frac{\tau(r)}{r^2} = 0 \, .$$

The general solution for $r \to 0$ reads

$$\frac{1}{\mathcal{L}_{\mathrm{UV}}} \tau(r) = m_q r (-\ln(r\Lambda))^{\frac{4}{3} + \frac{4\kappa_1}{3V_1}} \left[1 + \mathcal{O}\left(\frac{1}{\ln(r\Lambda)} \right) \right] \tag{A.12}$$
$$+ \sigma r^3 (-\ln(r\Lambda))^{-\frac{4}{3} - \frac{4\kappa_1}{3V_1}} \left[1 + \mathcal{O}\left(\frac{1}{\ln(r\Lambda)} \right) \right] \, .$$

Here matching with the perturbative anomalous dimension of the quark mass in QCD gives

$$\frac{4}{3} + \frac{4\kappa_1}{3V_1} = -\frac{\gamma_0}{b_0} = -\frac{9}{22 - 4x_f} \tag{A.13}$$

where γ_0 is the leading coefficient of the anomalous dimension of the quark mass in QCD.

The result can be again written in terms of A, and it becomes

$$\tau(A) = m_q \, \mathcal{L}_{\mathrm{UV}}^2 \, e^{-A} \, (\ln(A))^{-\frac{\gamma_0}{b_0}} \left[1 + \mathcal{O}\left(A^{-1} \right) \right] \tag{A.14}$$
$$+ \sigma \, \mathcal{L}_{\mathrm{UV}}^4 \, e^{-3A} \, (\ln(A))^{\frac{\gamma_0}{b_0}} \left[1 + \mathcal{O}\left(A^{-1} \right) \right] \, .$$

A.3 Finite temperature

The basic relations

$$f(r) = 1 - \frac{\int_0^r dr/b^3(r)}{\int_0^{r_h} dr/b^3(r)}, \quad \frac{1}{4\pi T} = b_h^3 \int_0^{r_h} \frac{dr}{b^3(r)}, \tag{A.15}$$

can be evaluated in the UV by inserting from (A.3)

$$b = e^A = \frac{\mathcal{L}_{\mathrm{UV}}}{r} \left[1 + \frac{4}{9\ln(\Lambda r)} + \frac{4}{9\ln^2(\Lambda r)} \left(\frac{b_1}{b_0^2} \ln(-\ln(\Lambda r)) + \frac{11}{9} - \frac{b_1}{2b_0^2} \right) \right]. \tag{A.16}$$

Terms of the order of $\ln^2(\ln)/\ln^3$ are neglected; for these, see [80]. One finds [20]

$$\int_0^r \frac{dr}{b^3(r)} = \frac{r^4}{4\mathcal{L}_{\mathrm{UV}}^3} \left[1 - \frac{4}{3\ln(\Lambda r)} - \frac{4}{3\ln^2(\Lambda r)} \left(\frac{b_1}{b_0^2} \ln(-\ln(\Lambda r)) + \frac{7}{12} - \frac{b_1}{2b_0^2} \right) \right], \tag{A.17}$$
$$T = \frac{1}{\pi r_h} \left(1 + \frac{1}{3\ln^2(\Lambda r_h)} \right). \tag{A.18}$$

For the quantity b_h/T needed for the latent heat one has

$$\frac{b_h}{T} = \pi \mathcal{L}_{\mathrm{UV}} \left[1 + \frac{4}{9\ln(\Lambda r_h)} + \frac{4}{9\ln^2(\Lambda r_h)} \left(\frac{b_1}{b_0^2} \ln(-\ln(\Lambda r_h)) + \frac{17}{36} - \frac{b_1}{2b_0^2} \right) \right]. \tag{A.19}$$

---

[20]Ref. [30–32], second paper, equation (D.3), has a different constant in the expansion of T. We have checked the 1/3 here also numerically.

B IR expansions

B.1 Zero temperature

Here we first discuss the expansions near the "good" IR singularity at zero temperature. It is the particular solution which can be lifted to finite temperature. In the IR, the tachyon potential in the DBI action is expected to be exponentially suppressed. Therefore the tachyon is again decoupled, and the IR behavior of λ and A can be solved separately from that of the tachyon. Moreover, the IR expansions of λ and A are exactly the same as in IHQCD. We will anyhow repeat the discussion for the particular asymptotics of V_g that matches well with the IR properties of QCD [30–32], which covers all potentials in this article.

B.1.1 A and λ

Let us assume that the potential V_g has the asymptotic behavior

$$V_g(\lambda) = v_0 \lambda^{4/3} \sqrt{\ln \lambda} \left[1 + \frac{v_1}{\ln \lambda} + \frac{v_2}{\ln^2 \lambda} + \cdots \right] . \tag{B.1}$$

Then the asymptotic solution reads

$$A = -\frac{r^2}{R^2} + \frac{1}{2} \ln \frac{r}{R} - \ln R - \frac{1}{2} \ln v_0 + \frac{5}{4} \ln 2 + \frac{3}{4} \ln 3 + \frac{23}{24} + \frac{4v_1}{3}$$
$$+ \frac{R^2 \left(-173 + 512 v_1^2 + 1024 v_2 \right)}{3456 r^2} + \mathcal{O}\left(r^{-4} \right) \tag{B.2}$$

$$= -\frac{r^2}{R^2} + \frac{1}{4} \ln \frac{3r^2}{2R^2} + A_0 + \frac{23}{24} + \frac{4v_1}{3}$$
$$+ \frac{R^2 \left(-173 + 512 v_1^2 + 1024 v_2 \right)}{3456 r^2} + \mathcal{O}\left(r^{-4} \right) \tag{B.3}$$

$$\ln \lambda = \frac{3}{2} \frac{r^2}{R^2} - \frac{23}{16} - 2v_1 - \frac{R^2 \left(151 + 512 v_1^2 + 1024 v_2 \right)}{2304 r^2} + \mathcal{O}\left(r^{-4} \right) \tag{B.4}$$

where

$$e^{A_0} = \frac{\sqrt{24}}{R \sqrt{v_0}}. \tag{B.5}$$

The IR scale $R = 1/\Lambda_{\rm IR}$ is an integration constant here.[21] Recall that r does not appear explicitly in the equations of motion, and therefore there is also an integration constant related to r: we have the freedom of shifting any solution by $r \to r + \delta r$. The solution having the simple r-dependence of eqs. (B.2) and (B.3) corresponds to a special choice of δr. It will have its UV boundary at an arbitrary value of r (rather than at $r = 0$). If δr is fixed instead by requiring the UV boundary to lie at $r = 0$, a corresponding shift must be added to the asymptotic formulas. For our choice of V_g,

$$v_0 = \frac{92 \left(b_0^{\rm YM} \right)^2 - 144 b_1^{\rm YM}}{27 \mathcal{L}_0^2} = \frac{18476}{243} \tag{B.6}$$

$$v_1 = \frac{1}{2} ; \qquad v_2 = -\frac{1}{8} \tag{B.7}$$

if we set $\mathcal{L}_0 = 1$.

---

[21]It is not independent of the scale $\Lambda = \Lambda_{\rm UV}$ of the UV expansions, i.e., the complete solution from UV to the IR will have fixed $\Lambda_{\rm UV}/\Lambda_{\rm IR}$.

Using A as the coordinate, the result reads

$$\frac{r^2}{R^2} = -A + \frac{1}{4}\ln\left(-\frac{3}{2}A\right) + A_0 + \frac{23}{24} + \frac{4v_1}{3}$$
$$-\frac{655 + 1152v_1 + 512v_1^2 + 1024v_2}{3456A} - \frac{\ln(-\frac{3}{2}A) + 4A_0}{16A} + \mathcal{O}\left(A^{-2}\right) \qquad (B.8)$$

$$\ln\lambda = -\frac{3}{2}A + \frac{3}{8}\ln\left(-\frac{3}{2}A\right) + \frac{3}{2}A_0 - \frac{7 + 16v_1 + 3\ln(-\frac{3}{2}A) + 12A_0}{32A} + \mathcal{O}\left(A^{-2}\right) \quad (B.9)$$

Various other combinations may be useful. In thermodynamics one needs $b = e^A$ in terms of λ; from (B.9) one can invert:

$$b = \left(\frac{3}{2}\right)^{3/4}\frac{4}{R\sqrt{v_0}}\frac{1}{\lambda^{2/3}}\left(\frac{2}{3}\ln\lambda\right)^{1/4}\left[1 + \mathcal{O}\left(\frac{1}{\ln\lambda}\right)\right] \qquad (B.10)$$

For the pair of functions $q(A) = e^A r'(A)$, $\lambda(A)$ used in numerics one can derive, for $A \to -\infty$,

$$q(A) = -\frac{R}{2}e^A(-A)^{-1/2}\left[1 + \frac{1}{8A}\left(\ln\left(-\frac{3}{2}A\right) + 4A_0 + \frac{9}{2}\right) + \mathcal{O}\left(A^{-2}\right)\right] \qquad (B.11)$$

$$\lambda(A) = e^{-\frac{3}{2}(A-A_0)}\left(-\frac{3}{2}A\right)^{3/8}\left[1 - \frac{3}{32A}\left(\ln\left(-\frac{3}{2}A\right) + 4A_0 + 5\right) + \mathcal{O}\left(A^{-2}\right)\right]. \quad (B.12)$$

B.1.2 The tachyon

The IR expansion of the tachyon depends on the large-λ asymptotics of the potentials V_f, a, and κ. Recall that the tachyon potential $V_f(\lambda, \tau)$ needs to vanish in the IR [37] in order to have correct kind of flavor anomalies. All power-law asymptotics for the potentials were analyzed in [26], and two different acceptable cases were chosen as examples. They are:

I Asymptotics with

$$a(\lambda) \sim \lambda^0 ; \qquad \kappa(\lambda) \sim \lambda^{4/3} ; \qquad V_{f0}(\lambda) \sim \lambda^{\hat{\tau}} \qquad (B.13)$$

where $\hat{\tau} < 10/3$. This case includes the potentials I and I_* of this article (for which $\hat{\tau} = 2$). The tachyon diverges exponentially for $r \to \infty$ ($A \to -\infty$),

$$\tau \sim e^{C_I \frac{r}{R}} \sim e^{C_I \sqrt{-A}} \qquad (B.14)$$

where the coefficient reads for potentials I

$$C_I = \frac{81 \; 3^{5/6}(115 - 16x_f)^{4/3}(11 - x_f)}{812944 \; 2^{1/6}} \; . \qquad (B.15)$$

II Asymptotics with

$$a(\lambda) \sim \lambda^{\hat{\sigma}} ; \qquad \kappa(\lambda) \sim \lambda^{4/3} ; \qquad V_{f0}(\lambda) \sim \lambda^{\hat{\tau}} \qquad (B.16)$$

where $\hat{\sigma} > 0$ and $\hat{\tau}$ can take any value. This case includes the potentials II and II$_*$ of this article (for which $\hat{\sigma} = 2/3$ and $\hat{\tau} = 2$). The tachyon diverges for $r \to \infty$ ($A \to -\infty$) as

$$\tau \sim C_{II}\sqrt{\frac{r}{R}} \sim C_{II}(-A)^{1/4} \tag{B.17}$$

where the coefficient reads for potentials II

$$C_{II} = \frac{27\ 2^{3/4}3^{1/4}}{\sqrt{4619}}\ . \tag{B.18}$$

B.2 Finite temperature

We will work out the finite temperature IR expansions in A-coordinates. Instead of writing down the explicit expansions as above, it is more convenient to state the relations between the coefficients of the series expansions. We start by defining the series

$$f = \epsilon f'_h + \mathcal{O}(\epsilon^2)\ , \quad f'(0) = f'_h + \epsilon f''_h + \mathcal{O}(\epsilon^2), \tag{B.19}$$

$$q = q_h + \epsilon q'_h + \mathcal{O}(\epsilon^2), \tag{B.20}$$

$$\lambda = \lambda_h + \epsilon \lambda'_h + \mathcal{O}(\epsilon^2), \tag{B.21}$$

$$\tau = \tau_h + \epsilon \tau'_h + \frac{1}{2}\epsilon^2 \tau''_h + \mathcal{O}(\epsilon^3), \tag{B.22}$$

where $\epsilon = A - A_h$ is the distance from the horizon, which lies at $A = A_h$, and all coefficients are to be evaluated at the horizon. The key input here is $f(A_h) = 0$. Inserting to the equations of motion one can solve for six of the nine coefficients listed above:

$$q_h = -\frac{\sqrt{3f'_h}}{\sqrt{V_g - V_f}}, \tag{B.23}$$

$$f''_h = -4f'_h + \frac{q_h^4}{f'_h}\left[\frac{1}{16}\lambda_h^2(\partial_\lambda V_g - \partial_\lambda V_f)^2 + \frac{(\partial_\tau V_f)^2}{6V_f\kappa_h}\right], \tag{B.24}$$

$$q'_h = \frac{q_h^5}{(f'_h)^2}\left[\frac{1}{16}\lambda_h^2(\partial_\lambda V_g - \partial_\lambda V_f)^2 + \frac{(\partial_\tau V_f)^2}{6V_f\kappa_h}\right] = q_h\left(4 + \frac{f''_h}{f'_h}\right), \tag{B.25}$$

$$\lambda'_h = -\frac{3\lambda_h^2 q_h^2}{8f'_h}(\partial_\lambda V_g - \partial_\lambda V_f), \tag{B.26}$$

$$\tau'_h = \frac{q_h^2 \partial_\tau \ln V_f}{f'_h \kappa_h}, \tag{B.27}$$

$$\tau''_h = \frac{9\partial_\tau V_f(A + B + C) + D}{12\kappa_h^2 V_f^3(V_f - V_g)^3}, \tag{B.28}$$

with the abbreviations

$$\begin{aligned}
A &= 6\lambda_h^2 \kappa'_h V_f^3(\partial_\lambda V_g - \partial_\lambda V_f), \\
B &= V_f^2[8\partial_\tau^2 V_f - 3\lambda_h^2(\partial_\lambda V_g - \partial_\lambda V_f)(\kappa_h(\partial_\lambda V_g - 3\partial_\lambda V_f) + 2\kappa'_h V_g)], \\
C &= -2V_f\left[6\partial_\tau V_f + V_g(4\partial_\tau^2 V_f + 3\lambda_h^2 \kappa_h \partial_\lambda V_f(\partial_\lambda V_g - \partial_\lambda V_f))\right], \\
D &= 27\lambda_h^2 \kappa_h \partial_\tau \partial_\lambda V_f V_f^2(V_g - V_f)(\partial_\lambda V_g - \partial_\lambda V_f).
\end{aligned} \tag{B.29}$$

Here $V_g \equiv V_g(\lambda_h)$, $V_f \equiv V_f(\lambda_h, \tau_h)$, $\kappa'_h = d\kappa(\lambda_h)/d\lambda$, $\kappa_h = \kappa(\lambda_h)$. The so far unspecified three coefficients λ_h, τ_h, and f'_h remain as free parameters. However f'_h will be fixed by requiring the standard normalization of the blackening factor $f \to 1$ in the UV. Therefore the physically relevant parameters are λ_h and τ_h, which can be mapped to the temperature and the quark mass after the full solution has been found.

C The quark mass and the Efimov solutions

As detailed in [26], the existence of the Efimov vacua is tightly linked to the tachyon mass at the IR fixed point, plotted in figure 3. In particular, the existence of the full Efimov tower of vacua with arbitrary number of tachyon nodes is guaranteed if the tachyon mass violates the BF bound. The same holds at finite temperature: one can always tune λ_h and τ_h such that the solution comes arbitrarily close to the fixed point. When the BF bound is violated, the tachyon solution is oscillatory in the vicinity of the fixed point. Thus, when approaching the fixed point the tachyon will achieve arbitrary many nodes, which signals the presence of the full Efimov tower. In this case the dependence of the quark mass on λ_h and τ_h is the "standard" one, i.e., qualitatively as in figure 5.

There are, however, some cases where either the fixed point is absent, which is the case for potentials I$_*$ and II$_*$ at low x_f, or the BF bound is not violated, which is the case, interestingly, for potentials I at very low x_f (as well as in the conformal window for all potentials). In such cases the picture can be different from figure 5. We shall not give a detailed description of all possible cases here, but rather discuss some of the main features and give examples.

The curve τ_{hc} (which actually starts at λ_*) exists if and only if there is a fixed point. If there is no fixed point, the solutions are expected to reach the standard UV boundary for all values of λ_h and τ_h. For the curves τ_{h0}, τ_{h1}, ... the situation is more complicated. At least few of these curves may still exist even if there is no fixed point or if the BF bound is satisfied at the fixed point. Their existence at asymptotically large λ_h is linked to the existence of Efimov solutions at zero temperature: taking $\lambda_h \to \infty$ with τ_h fixed along the curves, the finite temperature Efimov configurations converge towards their zero temperature counterparts. In particular, we expect that the chiral symmetry is broken at zero temperature if and only if τ_{h0} exists at asymptotically large λ_h. We have found numerically that the curves are always absent in the conformal window, $x_f \geq x_c$, so that chiral symmetry is intact. This turns out to be the case also for potentials I at large W_0 and low x_f, but only in a part of the region where BF bound is satisfied at the fixed point. See also the phase diagrams in figure 18 of section 4 which show that chiral symmetry is intact at low x_f. For potentials I$_*$ and at low x_f, where no fixed point exists, the curves are also absent, and chiral symmetry is unbroken. In this case the $m_q = 0$ thermodynamics is determined by the $\tau = 0$ solution and is qualitatively similar to the Yang-Mills one (see also figure 19). For potentials II$_*$ however, at least the leading solution τ_{h0} can always be found and chiral symmetry is thus broken at low temperatures (see figure 17).

D Computation of λ_{end}

One can also illustrate the connection of the behavior of λ_{end} to the BF bound of the tachyon (figure 3), assuming that we have chosen a set of potentials and value of x_f such that the IR fixed point exists. First we recall that λ_{end} can be defined as the endpoint of the $\tau_{h0}(\lambda_h)$ curve which gives the (non-node) solution with nontrivial tachyon and zero quark mass (figure 5). In particular, as λ_h approaches λ_{end} from above, τ_h tends to zero, and we expect that the whole tachyon solution from the boundary to the horizon becomes small, and the tachyon decouples from the other fields. Therefore, in order to define λ_{end} it is enough to study the behavior of the tachyon based on the linearized tachyon EoM, evaluated on a fixed background, obtained by setting the tachyon to zero.

The linearized tachyon equation has the form

$$\tau''(r) + F_1 \tau'(r) + F_2 \tau(r) = 0 \tag{D.1}$$

where

$$F_1 = 3A'(r) + \frac{f'(r)}{f(r)} + \lambda'(r)\frac{\partial \ln \kappa(\lambda)}{\partial \lambda} + \lambda'(r)\frac{\partial \ln V_{f0}(\lambda)}{\partial \lambda}, \tag{D.2}$$

$$F_2 = \frac{2e^{2A}a(\lambda)}{f(r)\kappa(\lambda)} .$$

Here $A(r)$, $\lambda(r)$, and $f(r)$ are the solutions of the EoMs for $\tau \equiv 0$, which are the same for potentials I and II. The drastic difference between the potentials, as suggested by figure 3, thus arises only through the appearances of a and κ in the coefficients (D.2). The regular tachyon solution, which is finite in the IR, obeys

$$\frac{\tau'(r_h)}{\tau(r_h)} = -\lim_{r \to r_h} \frac{F_2}{F_1} \tag{D.3}$$

since the double-derivative term in (D.1) is negligible near the horizon.

Nodes of the regular solution to the linear tachyon equation can then be used to determine λ_{end}. For small λ_h perturbative analysis applies and it is not difficult to see that the solution is monotonic, without nodes. When λ_h increases the equation becomes nontrivial and has to be studied numerically. Usually we observe, that beyond a critical value of λ_h a tachyon node appears in the UV. The leading tachyon behavior in the UV is controlled by the quark mass, which has to vanish at the critical value. We thus identify the critical value as λ_{end}, which was defined as the endpoint of the curve where $m_q = 0$. Thus the regular solution to the linearized EoM has no nodes for $\lambda_h < \lambda_{\text{end}}$ and one or more nodes for $\lambda_h > \lambda_{\text{end}}$. It can also happen that λ_{end} does not exist, and the tachyon nodes are absent for all λ_h.

Since λ_h can take values from zero to λ_*, we can construct backgrounds which get arbitrarily close to the IR fixed point at $\lambda = \lambda_*$. If the BF bound for the tachyon is violated at the fixed point, the tachyon must have nodes as $\lambda_h \to \lambda_*$. We can conclude that λ_{end}, and thus also the curve τ_{h0}, exist in this case. This makes sense, since when the BF bound is violated, chiral symmetry breaking takes place also at zero temperature, which means the the curve τ_{h0} exist also at asymptotically large λ_h as discussed in appendix C.

We can also say something about $\lambda_{\rm end}$ in the probe limit $x_f \to 0$. For PotII it seems that it approaches a fixed value as seen from figure 22 (right). This value can be found by solving the linearized tachyon EoM with a background evaluated at $x_f = 0$ (i.e., the IHQCD solution), and by checking if a special value of λ_h (identified as $\lambda_{\rm end}$) can be found where nodes emerge in the tachyon solution. Notice that λ_* goes to ∞ in the probe limit so that λ_h can take any value. Existence of the limiting value of $\lambda_{\rm end}$ as $x_f \to 0$ thus requires that the tachyon has nodes in the limit $\lambda_h \to \infty$ after first taking the probe limit. Since zero temperature solutions are obtained for $\lambda_h \to \infty$, it is plausible that the behavior of figure 22 (right) is seen if and only if the probe limit system admits tachyon solutions with nodes (in other words, chiral symmetry breaking) at zero temperature. Recall that for PotI, for which the different behavior of figure 22 (left) is found, chiral symmetry is unbroken at low x_f.

E Computation of the condensate

In principle, the condensate for an $m_q = 0$ system could be computed from the UV expansion

$$\tau(r)/\mathcal{L}_{\rm UV} = \sigma r^3 (-\ln(\Lambda r))^{3/(2b_0)}, \quad r \to 0, \tag{E.1}$$

with

$$A - \ln(\Lambda \mathcal{L}_{\rm UV}) = \frac{1}{b_0 \lambda(A)} + \frac{b_1}{b_0^2} \ln(b_0 \lambda(A)) = -\ln(\Lambda r), \quad A \to \infty, \tag{E.2}$$

where we dropped corrections of $\mathcal{O}(A^{-1})$. Using this one can define

$$\ln \tilde{\sigma}(A) = \ln \tau(A) - \ln \mathcal{L}_{\rm UV} + \frac{3}{b_0 \lambda(A)} + \frac{3b_1}{b_0^2} \ln(b_0 \lambda(A)) + \frac{3}{2b_0} \ln(b_0 \lambda(A)), \tag{E.3}$$

which approaches $\ln \sigma$ for $A \to \infty$.

However, our solution for the tachyon, which is obtained numerically by shooting from the IR, will have a linear term $\tau \sim m_q r$ with a tiny quark mass (typically $m_q \sim 10^{-7}$), because the IR boundary conditions cannot be fine tuned beyond the numerical accuracy of the code. The linear term will dominate over the cubic one of eq. (E.2) in the deep UV. In order to calculate the condensate, we need to separate the linear and cubic terms from the numerically computed $\tau(A)$, and use the cubic solution in eq. (E.3). For $\tilde{\sigma}(A)$ to be a good approximation to the condensate σ, we need to have $A \sim$ hundreds. Direct separation of the linear m_q term in this region requires numerical accuracy on the level of $e^{-\rm hundreds}$, which is practically impossible to achieve.

To illustrate the difficulty and its resolution, consider a concrete case. Let us take Potential II, SB normalised, $\mathcal{L}_{\rm UV} = (1 + \frac{7}{4} x_f)^{1/3}$, $x_f = 3$. This system, when cooled, has a 2nd order transition at $T_{\rm end} = 1.158 T_h$, above a 1st order transition at T_h. This is concretely seen in figure 9. Since chiral symmetry is broken at $T_{\rm end}$ we expect that $\sigma(T)$ starts growing from zero at $T_{\rm end}$ and grows when the system is cooled towards T_h. As an example, we evaluate the condensate when T has been cooled to $T = 0.95 T_{\rm end} = 1.1 T_h$.

Numerical solution of Einstein's equations required knowing the values of λ_h, τ_h leading to a certain T with $m_q = 0$. For this potential and T they were $\lambda_h = 0.4017564, \tau_h = $

$\tau_{h0}(\lambda_h, m_q = 0) = 0.217984$. The computed $\tau(A)$ is shown in figure 28. For A up to about 10 one discerns the required $r^3 \sim e^{-3A}$ behavior, but beyond that $r \sim e^{-A}$ sets in and extends up to the end point of the computation at $A = 400$. It is impossible to shoot from the horizon and get $m_q = 0$ more accurately; note that the tachyon has already decreased to 10^{-14} from 0.22 at the horizon.

To impose $\tau(r) \sim r^3$ one must shoot from the boundary, $r = 0$, $A = \infty$. In this limit the evolution of τ decouples from the other bulk fields, of which only $\lambda(A)$ is relevant since $f \approx 1$. We can thus integrate the tachyon equation from some large $A(= 400)$ using the $\lambda(A)$ from Einstein's equations and imposing as the initial condition $\tau(A) = e^{-3A}$, $\tau'(A) = -3e^{-3A}$ with small enough normalisation.[22] The result is plotted as the curve $\tau_{\text{UV}}(A)$ in figure 28. One observes that in the range $A = 2 \ldots 10$ the curve behaves accurately as a constant$\times \tau_{\text{IR}}(A)$ and the normalisation can thus be determined. In this way the true $\tau(A; m_q = 0)$ plotted in figure 28 is obtained.

Now that the accurate $\tau(A)$ is known, $\ln \tilde{\sigma}(A)$ can be plotted using eq. (E.3), see figure 28. For the extrapolation it is even more convenient to plot as a function of $\lambda(A)$, see also figure 28. One obtains a nice linear behavior with the asymptotic value $\ln \sigma = -5.1558$, $\sigma(T = 0.95T_{\text{end}}) = 0.005766$.

If one used the original $\tau(A, m_q = 0)$ at the largest value of A, $A = 10$, where the r^3 behavior was obtained, one would have $\tilde{\sigma} = 0.0106$. This is too large by a factor 1.82, not very far off, but actually slightly larger than the expected 10% error from neglecting the $\mathcal{O}(A^{-1})$ corrections in eqs. (E.2) and (E.3) at this value of A. If we tried using the $\tau(A, m_q = 0)$ solution directly, reliable extraction of σ would thus require much higher numerical precision, as already mentioned above.

After applying the procedure discussed above, the dominant error in the value of σ arises actually from the matching of the two tachyon solutions that were obtained by shooting from the UV and from the IR. The solutions are not exactly proportional for $0 \lesssim A \lesssim 10$ due to nonlinearities in the tachyon EoM and coupling to other fields. The error can be reduced by introducing a further subtraction trick that effectively reduces the value of m_q of the solution that was obtained by shooting form the IR, so that the matching can be done for slightly higher values of A where the coupling effects are considerably reduced.

We follow [26] and construct two solutions $\tau_{1,2}$ with small but different values $m_{q1,q2}$. Optimal choice is to take $|m_q|$ as small as possible and choose one solution with a positive value and another with a negative one. Then we construct

$$\tau_{\text{IR}}(A) = \frac{1}{1 - \frac{m_{q1}}{m_{q2}}} \left(\tau_1(A) - \frac{m_{q1}}{m_{q2}} \tau_2(A) \right) \tag{E.4}$$

where the ratio m_{q1}/m_{q2} can be accurately determined as the ratio of the solutions τ_1/τ_2 at

---

[22]It is not important to have precisely correct UV boundary conditions, since corrections to the $\tau \sim r^3$ solution will decay fast as the system is solved toward the IR. One should only make sure that the tachyon is much less than one in the whole region of interest ($A \gtrsim 0$) in order to suppress nonlinear effects, or alternatively use explicitly linearized differential equation for the tachyon.
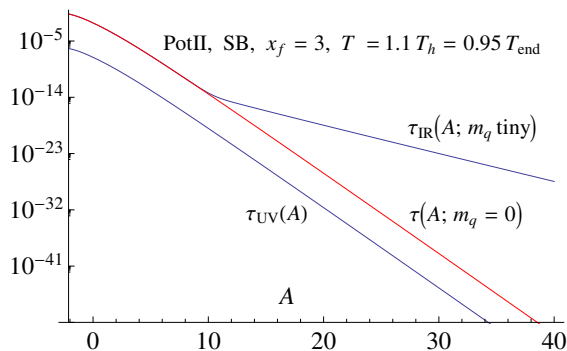
Figure 28. The tachyon computed for $T = 0.95T_{\rm end} = 1.1T_h$. The curve $\tau_{\rm IR}(A, m_q = {\rm tiny})$ is obtained by integrating Einstein's equations from the horizon and tuning $m_q = 0$ as accurately as possible. The curve $\tau_{\rm UV}(A)$ is obtained by integrating the tachyon equation of motion from the UV at $A = 400$ using the bulk field $\lambda(A)$ from Einstein's equation and imposing $\tau \sim r^3$ in the UV. The normalisation can be fixed by matching to $\tau_{\rm IR}$ in the $A = 2 \ldots 10$ range and a reliable $\tau(A, m_q = 0)$ for the true $m_q = 0$ tachyon is obtained.
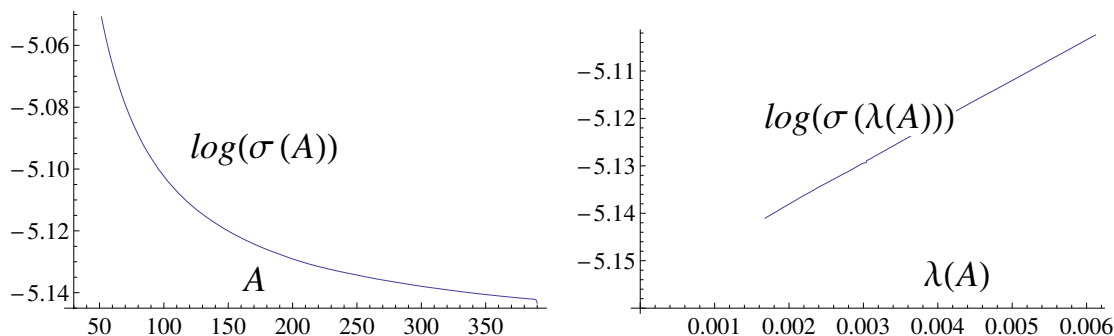
Figure 29. Extrapolation of the value of $\ln \sigma$ to $r = 0$, $A = \infty$, $\lambda = 0$, for the potential and temperature as in figure 28

large A (say $A = 400$).[23] The point is that the constructed $\tau_{\rm IR}$ has its m_q several orders of magnitude closer to zero than either of the solutions $\tau_{1,2}$. Moreover, the residual dependence of σ on m_q is drastically reduced: the linear corrections cancel in (E.4) (see [26]). The improved value of σ can now be found by matching $\tau_{\rm IR}$ with the solution $\tau_{\rm UV}$, which was obtained by shooting from the UV, as discussed above.

Open Access. This article is distributed under the terms of the Creative Commons Attribution License which permits any use, distribution and reproduction in any medium, provided the original author(s) and source are credited.

---

[23]There is a small technicality involved in this procedure as the two solutions will in general have different values of Λ. Changing Λ is equivalent with shifts of A in A-coordinates (see eq. (E.2)), so we can fix the issue by shifting, say, the solution τ_2 by a small ΔA, obtained by requiring that the corresponding solutions $\lambda_{1,2}$ for the coupling match at large A. Notice also that the resulting $\tau_{\rm IR}$ is only useful in the UV region $A \gtrsim 0$.

References

[1] G. Veneziano, U(1) *without instantons*, *Nucl. Phys.* **B 159** (1979) 213 [INSPIRE].

[2] T. Banks and A. Zaks, *On the phase structure of vector-like gauge theories with massless fermions*, *Nucl. Phys.* **B 196** (1982) 189 [INSPIRE].

[3] W.E. Caswell, *Asymptotic behavior of nonabelian gauge theories to two loop order*, *Phys. Rev. Lett.* **33** (1974) 244 [INSPIRE].

[4] D.R.T. Jones, *Two loop diagrams in Yang-Mills theory*, *Nucl. Phys.* **B 75** (1974) 531 [INSPIRE].

[5] V.L. Berezinskii, *Destruction of long-range order in one-dimensional and two-dimensional systems having a continuous symmetry group. I. Classical systems*, *Zh. Eksp. Teor. Fiz.* **59** (1970) 907 [*Sov. Phys. JETP* **32** (1971) 493].

[6] J. Kosterlitz and D. Thouless, *Ordering, metastability and phase transitions in two-dimensional systems*, *J. Phys.* **C 6** (1973) 1181 [INSPIRE].

[7] V.A. Miransky, *Dynamics of spontaneous chiral symmetry breaking and continuum limit in quantum electrodynamics*, *Nuovo Cim.* **A90** (1985) 149.

[8] M.G. Alford, K. Rajagopal and F. Wilczek, *QCD at finite baryon density: nucleon droplets and color superconductivity*, *Phys. Lett.* **B 422** (1998) 247 [hep-ph/9711395] [INSPIRE].

[9] M.G. Alford, K. Rajagopal and F. Wilczek, *Color flavor locking and chiral symmetry breaking in high density QCD*, *Nucl. Phys.* **B 537** (1999) 443 [hep-ph/9804403] [INSPIRE].

[10] J. Giedt, *Lattice gauge theory and physics beyond the standard model*, talk given at the 30th *International Symposium on Lattice Field Theory (Lattice2012)*, June 24–29, Cairns, Australia (2012).

[11] M. Panero, *Recent results in large-N lattice gauge theories*, talk given at the 30th *International Symposium on Lattice Field Theory (Lattice2012)*, June 24–29, Cairns, Australia (2012).

[12] M. Teper, *Large-N and confining flux tubes as strings — A view from the lattice*, *Acta Phys. Polon.* **B 40** (2009) 3249 [arXiv:0912.3339] [INSPIRE].

[13] B. Lucini and M. Panero, SU(N) *gauge theories at large-N*, arXiv:1210.4997 [INSPIRE].

[14] Z. Fodor et al., *Twelve massless flavors and three colors below the conformal window*, *Phys. Lett.* **B 703** (2011) 348 [arXiv:1104.3124] [INSPIRE].

[15] X.-Y. Jin and R.D. Mawhinney, *Evidence for a first order, finite temperature phase transition in 8 flavor QCD*, PoS(LATTICE 2010)055 [arXiv:1011.1511] [INSPIRE].

[16] K. Miura, M.P. Lombardo and E. Pallante, *Chiral phase transition at finite temperature and conformal dynamics in large N_f QCD*, *Phys. Lett.* **B 710** (2012) 676 [arXiv:1110.3152] [INSPIRE].

[17] J. Kogut and D. Sinclair, *Thermodynamics of lattice QCD with 3 flavours of colour-sextet quarks*, *Phys. Rev.* **D 85** (2012) 054505 [arXiv:1111.3353] [INSPIRE].

[18] R.D. Pisarski, *Finite temperature QCD at large-N*, *Phys. Rev.* **D 29** (1984) 1222 [INSPIRE].

[19] A. Dumitru and R.D. Pisarski, *Degrees of freedom and the deconfining phase transition*, *Phys. Lett.* **B 525** (2002) 95 [hep-ph/0106176] [INSPIRE].

[20] T. Appelquist, A. Ratnaweera, J. Terning and L. Wijewardhana, *The phase structure of an* SU(N) *gauge theory with* N_f *flavors*, *Phys. Rev.* **D 58** (1998) 105017 [hep-ph/9806472] [INSPIRE].

[21] F. Sannino and J. Schechter, *Chiral phase transition for* SU(N) *gauge theories via an effective Lagrangian approach*, *Phys. Rev.* **D 60** (1999) 056004 [hep-ph/9903359] [INSPIRE].

[22] J.T. Lenaghan, D.H. Rischke and J. Schaffner-Bielich, *Chiral symmetry restoration at nonzero temperature in the* SU(3)(r) × SU(3)(l) *linear* σ-*model*, *Phys. Rev.* **D 62** (2000) 085008 [nucl-th/0004006] [INSPIRE].

[23] P. Calabrese and P. Parruccini, *Five loop* ϵ-*expansion for* U(n) × U(m) *models: finite temperature phase transition in light QCD*, *JHEP* **05** (2004) 018 [hep-ph/0403140] [INSPIRE].

[24] A. Karch and A. O'Bannon, *Chiral transition of* $N = 4$ *super Yang-Mills with flavor on a 3-sphere*, *Phys. Rev.* **D 74** (2006) 085033 [hep-th/0605120] [INSPIRE].

[25] Y. Kikukawa, M. Kohda and J. Yasuda, *First-order restoration of* SU(NF) × SU(N_f) *chiral symmetry with large-*N_f *and electroweak phase transition*, *Phys. Rev.* **D 77** (2008) 015014 [arXiv:0709.2221] [INSPIRE].

[26] M. Jarvinen and E. Kiritsis, *Holographic models for QCD in the Veneziano limit*, *JHEP* **03** (2012) 002 [arXiv:1112.1261] [INSPIRE].

[27] R. Narayanan and H. Neuberger, *Chiral symmetry restoration at finite temperature in the planar limit*, *Phys. Lett.* **B 638** (2006) 546 [hep-th/0605173] [INSPIRE].

[28] L. McLerran and R.D. Pisarski, *Phases of cold, dense quarks at large-*N_c, *Nucl. Phys.* **A 796** (2007) 83 [arXiv:0706.2191] [INSPIRE].

[29] T. Kahara and K. Tuominen, *Effective models of two-flavor QCD: finite* μ *and* m_q-*dependence*, *Phys. Rev.* **D 82** (2010) 114026 [arXiv:1006.3931] [INSPIRE].

[30] U. Gürsoy and E. Kiritsis, *Exploring improved holographic theories for QCD: part I*, *JHEP* **02** (2008) 032 [arXiv:0707.1324] [INSPIRE].

[31] U. Gürsoy, E. Kiritsis and F. Nitti, *Exploring improved holographic theories for QCD: part II*, *JHEP* **02** (2008) 019 [arXiv:0707.1349] [INSPIRE].

[32] E. Kiritsis, *Dissecting the string theory dual of QCD*, *Fortsch. Phys.* **57** (2009) 396 [arXiv:0901.1772] [INSPIRE].

[33] U. Gürsoy, E. Kiritsis, L. Mazzanti and F. Nitti, *Deconfinement and gluon plasma dynamics in improved holographic QCD*, *Phys. Rev. Lett.* **101** (2008) 181601 [arXiv:0804.0899] [INSPIRE].

[34] U. Gürsoy, E. Kiritsis, L. Mazzanti and F. Nitti, *Holography and thermodynamics of* 5D *dilaton-gravity*, *JHEP* **05** (2009) 033 [arXiv:0812.0792] [INSPIRE].

[35] U. Gürsoy, E. Kiritsis, L. Mazzanti and F. Nitti, *Improved holographic Yang-Mills at finite temperature: comparison with data*, *Nucl. Phys.* **B 820** (2009) 148 [arXiv:0903.2859] [INSPIRE].

[36] U. Gürsoy, E. Kiritsis, L. Mazzanti, G. Michalogiorgakis and F. Nitti, *Improved holographic QCD*, *Lect. Notes Phys.* **828** (2011) 79 [arXiv:1006.5461] [INSPIRE].

[37] R. Casero, E. Kiritsis and A. Paredes, *Chiral symmetry breaking as open string tachyon condensation*, *Nucl. Phys.* **B 787** (2007) 98 [hep-th/0702155] [INSPIRE].

[38] I. Iatrakis, E. Kiritsis and A. Paredes, *An AdS/QCD model from Sen's tachyon action*, *Phys. Rev.* **D 81** (2010) 115004 [arXiv:1003.2377] [INSPIRE].

[39] I. Iatrakis, E. Kiritsis and A. Paredes, *An AdS/QCD model from tachyon condensation: II*, *JHEP* **11** (2010) 123 [arXiv:1010.1364] [INSPIRE].

[40] F. Bigazzi, R. Casero, A. Cotrone, E. Kiritsis and A. Paredes, *Non-critical holography and four-dimensional CFT's with fundamentals*, *JHEP* **10** (2005) 012 [hep-th/0505140] [INSPIRE].

[41] J. Alanen, K. Kajantie and V. Suur-Uski, *Spatial string tension of finite temperature QCD matter in gauge/gravity duality*, *Phys. Rev.* **D 80** (2009) 075017 [arXiv:0905.2032] [INSPIRE].

[42] J. Alanen, K. Kajantie and V. Suur-Uski, *A gauge/gravity duality model for gauge theory thermodynamics*, *Phys. Rev.* **D 80** (2009) 126008 [arXiv:0911.2114] [INSPIRE].

[43] S.S. Gubser and A. Nellore, *Mimicking the QCD equation of state with a dual black hole*, *Phys. Rev.* **D 78** (2008) 086007 [arXiv:0804.0434] [INSPIRE].

[44] O. DeWolfe, S.S. Gubser and C. Rosen, *A holographic critical point*, *Phys. Rev.* **D 83** (2011) 086005 [arXiv:1012.1864] [INSPIRE].

[45] J. Alanen and K. Kajantie, *Thermodynamics of a field theory with infrared fixed point from gauge/gravity duality*, *Phys. Rev.* **D 81** (2010) 046003 [arXiv:0912.4128] [INSPIRE].

[46] J. Alanen, K. Kajantie and K. Tuominen, *Thermodynamics of quasi conformal theories from gauge/gravity duality*, *Phys. Rev.* **D 82** (2010) 055024 [arXiv:1003.5499] [INSPIRE].

[47] J. Alanen, T. Alho, K. Kajantie and K. Tuominen, *Mass spectrum and thermodynamics of quasi-conformal gauge theories from gauge/gravity duality*, *Phys. Rev.* **D 84** (2011) 086007 [arXiv:1107.3362] [INSPIRE].

[48] G. Bertoldi, F. Bigazzi, A. Cotrone and J.D. Edelstein, *Holography and unquenched quark-gluon plasmas*, *Phys. Rev.* **D 76** (2007) 065007 [hep-th/0702225] [INSPIRE].

[49] C. Núñez, I. Papadimitriou and M. Piai, *Walking dynamics from string duals*, *Int. J. Mod. Phys.* **A 25** (2010) 2837 [arXiv:0812.3655] [INSPIRE].

[50] S.P. Kumar, D. Mateos, A. Paredes and M. Piai, *Towards holographic walking from $N = 4$ super Yang-Mills*, *JHEP* **05** (2011) 008 [arXiv:1012.4678] [INSPIRE].

[51] L. Anguelova, *Electroweak symmetry breaking from gauge/gravity duality*, *Nucl. Phys.* **B 843** (2011) 429 [arXiv:1006.3570] [INSPIRE].

[52] L. Anguelova, P. Suranyi and L. Wijewardhana, *Holographic walking technicolor from D-branes*, *Nucl. Phys.* **B 852** (2011) 39 [arXiv:1105.4185] [INSPIRE].

[53] L. Anguelova, P. Suranyi and L.R. Wijewardhana, *Scalar mesons in holographic walking technicolor*, *Nucl. Phys.* **B 862** (2012) 671 [arXiv:1203.1968] [INSPIRE].

[54] D. Kutasov, J. Lin and A. Parnachev, *Conformal phase transitions at weak and strong coupling*, *Nucl. Phys.* **B 858** (2012) 155 [arXiv:1107.2324] [INSPIRE].

[55] D.K. Hong and H.-U. Yee, *Holographic estimate of oblique corrections for technicolor*, *Phys. Rev.* **D 74** (2006) 015011 [hep-ph/0602177] [INSPIRE].

[56] K. Haba, S. Matsuzaki and K. Yamawaki, *S parameter in the holographic walking/conformal technicolor*, *Prog. Theor. Phys.* **120** (2008) 691 [arXiv:0804.3668] [INSPIRE].

[57] D.D. Dietrich and C. Kouvaris, *Constraining vectors and axial-vectors in walking technicolour by a holographic principle*, *Phys. Rev.* **D 78** (2008) 055005 [arXiv:0805.1503] [InSPIRE].

[58] D.D. Dietrich and C. Kouvaris, *Generalised bottom-up holography and walking technicolour*, *Phys. Rev.* **D 79** (2009) 075004 [arXiv:0809.1324] [InSPIRE].

[59] D.D. Dietrich, M. Jarvinen and C. Kouvaris, *Mixing in the axial sector in bottom-up holography for walking technicolour*, *JHEP* **07** (2010) 023 [arXiv:0908.4357] [InSPIRE].

[60] D. Kutasov, J. Lin and A. Parnachev, *Holographic walking from tachyon DBI*, *Nucl. Phys.* **B 863** (2012) 361 [arXiv:1201.4123] [InSPIRE].

[61] C. Núñez, A. Paredes and A.V. Ramallo, *Unquenched flavor in the gauge/gravity correspondence*, *Adv. High Energy Phys.* **2010** (2010) 196714 [arXiv:1002.1088] [InSPIRE].

[62] O. Bergman, S. Seki and J. Sonnenschein, *Quark mass and condensate in HQCD*, *JHEP* **12** (2007) 037 [arXiv:0708.2839] [InSPIRE].

[63] A. Dhar and P. Nag, *Sakai-Sugimoto model, tachyon condensation and chiral symmetry breaking*, *JHEP* **01** (2008) 055 [arXiv:0708.3233] [InSPIRE].

[64] A. Dhar and P. Nag, *Tachyon condensation and quark mass in modified Sakai-Sugimoto model*, *Phys. Rev.* **D 78** (2008) 066021 [arXiv:0804.4807] [InSPIRE].

[65] N. Jokela, M. Järvinen and S. Nowling, *Winding effects on brane/anti-brane pairs*, *JHEP* **07** (2009) 085 [arXiv:0901.0281] [InSPIRE].

[66] D.B. Kaplan, J.-W. Lee, D.T. Son and M.A. Stephanov, *Conformality lost*, *Phys. Rev.* **D 80** (2009) 125005 [arXiv:0905.4752] [InSPIRE].

[67] M. Järvinen and F. Sannino, *Holographic conformal window — A bottom up approach*, *JHEP* **05** (2010) 041 [arXiv:0911.2462] [InSPIRE].

[68] O. Antipin and K. Tuominen, *Constraints on conformal windows from holographic duals*, *Mod. Phys. Lett.* **A 26** (2011) 2227 [arXiv:0912.0674] [InSPIRE].

[69] R. Alvares, N. Evans and K.-Y. Kim, *Holography of the conformal window*, *Phys. Rev.* **D 86** (2012) 026008 [arXiv:1204.2474] [InSPIRE].

[70] D. Arean, I. Iatrakis, M. Järvinen and E. Kiritsis, *V-QCD: spectra, the dilaton and the S-parameter*, arXiv:1211.6125 [InSPIRE].

[71] K. Tuominen, *Finite temperature phase diagrams of gauge theories*, arXiv:1206.5772 [InSPIRE].

[72] J. Noronha, *Polyakov loops in strongly-coupled plasmas with gravity duals*, *J. Phys.* **G 37** (2010) 094018 [arXiv:1001.3155] [InSPIRE].

[73] M. Panero, *Thermodynamics of the QCD plasma and the large-N limit*, *Phys. Rev. Lett.* **103** (2009) 232001 [arXiv:0907.3719] [InSPIRE].

[74] J. Braun and H. Gies, *Chiral phase boundary of QCD at finite temperature*, *JHEP* **06** (2006) 024 [hep-ph/0602226] [InSPIRE].

[75] J. Braun and H. Gies, *Scaling laws near the conformal window of many-flavor QCD*, *JHEP* **05** (2010) 060 [arXiv:0912.4168] [InSPIRE].

[76] M. Järvinen and F. Sannino, *Extreme technicolor and the walking critical temperature*, *JHEP* **02** (2011) 081 [arXiv:1009.5380] [InSPIRE].

[77] J. Braun, C.S. Fischer and H. Gies, *Beyond Miransky scaling*, *Phys. Rev.* **D 84** (2011) 034045 [arXiv:1012.4279] [INSPIRE].

[78] D.M. Broun, *What lies beneath the dome?*, *Nature Phys.* **4** (2008) 170.

[79] M. Teper, *Large-N*, PoS(LATTICE 2008)022 [arXiv:0812.0085] [INSPIRE].

[80] K. Kajantie, M. Krssak, M. Vepsäläinen and A. Vuorinen, *Frequency and wave number dependence of the shear correlator in strongly coupled hot Yang-Mills theory*, *Phys. Rev.* **D 84** (2011) 086004 [arXiv:1104.5352] [INSPIRE].